Anisotropic Acquisition and Analysis for Diffusion Tensor Magnetic Resonance Imaging

by

Jee Eun Lee

A dissertation submitted in partial fulfillment of

the requirements for the degree of

Doctor of Philosophy

(Medical Physics)

at the

UNIVERSITY OF WISCONSIN-MADISON

2006

ABSTRACT

Diffusion tensor magnetic resonance imaging (DT-MRI) is a non-invasive imaging method for assessing the characteristics and organization of tissue microstructure. The diffusion tensor provides information about the magnitude, anisotropy, and orientation of water diffusion in biological tissues. In brain white matter, the direction of greatest diffusivity is typically assumed to be parallel to the white matter tracts. The number of DT-MRI applications is rapidly expanding; however, diffusion tensor measurements are also highly sensitive to noise in the raw diffusion weighted (DW) images. Furthermore, the relatively poor spatial resolution of most DT-MRI studies cause partial volume averaging between different tissue regions, which can lead to errors in the estimated DT-MRI measures. Finally, the variance of DT-MRI measures may impair the ability to detect and characterize subtle differences either between regions or subjects. In this thesis, new acquisition and analysis methods for reducing measurement noise effects are investigated.

For the case where the diffusion tensor orientation and shape may be estimated a priori, changing the diffusion-weighting with encoding direction may improve the overall accuracy of the diffusion tensor measurements. The variance of DT-MRI measurements is expressed as a function of directional diffusitivities and diffusion weightings. Minimizing the variance using quadratic optimization algorithms leads to an obtainment of anisotropic diffusion weightings. In this study anisotropic diffusion weighting reduced the variance of FA and MD measurements by roughly 50 % in the corpus callosum.

Anisotropic Gaussian kernel smoothing was used to reduce the errors and noise for

the entire regions of DT-MRI data. The anisotropic Gaussian kernels for convolution smoothing are equivalent to the water diffusion distributions described by the diffusion tensor. Further the direction of greatest diffusitivity is often assumed to be parallel to the direction of the local white matter tracts, thus the measured diffusion tensor is a good candidate for anisotropic kernel smoothing. This reduces the partial averaging effects with high levels of smoothing.

In voxel based analyses of DT-MRI data, isotropic Gaussian kernel smoothing is often used to blur the individually distinct anatomic features. Anisotropic Gaussian kernel smoothing may reduce the partial volume averaging which will improve anatomic specificity. In this study, anisotropic Gaussian smoothing was applied to DT-MR data from a group of autism subjects to investigate the differences of DT-MRI measurements between the autism and control groups. Anisotropic Gaussian kernel smoothing provides more consistent results for the group differences as compared with manual ROI analysis Finally, anisotropic Gaussian kernel smoothing may be useful for estimating anatomic connectivity as the diffusion will be greatest along the white matter pathways. In this study iterative convolution with anisotropic Gaussian kernels was used to estimate connectivity patterns in DT-MRI fields. Preliminary results in both phantoms and human brain were promising. Future developments will constrain the diffusion propagation to white matter to eliminate erroneous pathways.

Acknowledgments

First and foremost, I would like to thank my supervisor Andy Alexander for his warm and insightful guidance. His continuing devotion and innovative ideas in his studies have been truly inspiring to me.

I am thankful for Moo Chung for his exquisite knowledge and useful advice in Statistics. Without his abundant ideas and guidance, my thesis would not be carried on in a right direction. I'd also like to thank all my other committee members; Beth Meyerand, Wally Block, and Aaron Field, who generously advised me to carry out this dissertation.

I would not be able to accomplish what I wanted without Terry Oakes and Mariana Lazar for all my computer programming troubles. I'd like to send my great appreciation to Mariana and Terry for their valuable help.

I am sincerely grateful to Prof. Hyun Myung Jang, who always believes in me and guides me. I'd like to thank all my friends to cheer me up whenever I got desperate, especially Hyejeen Lee and Jeihoon Baek to have helped me grow as a person.

Last but not least, I thank my parents and my sisters who love and support me in every way.

Contents

List of Figures

List of Tables

List of Symbols

ADC	Apparent diffusion coefficient
AG	Anisotropic Gaussian
IG	Isotropic Gaussian
PM	Perona Malik algorithm
B	Magnetic field
b	diffusion weighting
CC	Corpus Callosum
CNS	Central nervous system
CSF	Cerebral spinal fluid
DNR	Diffusion to noise ratio
DW	Diffusion weighted
DWI	Diffusion weighted images
DT-MRI	Diffusion tensor magnetic resonance imaging
DTI	Diffusion tensor imaging
EPI	Echo Planar Imaging
FA	Fractional anisotropy
g	Diffusion weighting gradient
GM	Grey matter
MD	Mean Diffusitivity
NEX	Number of excitations
NMR	Nuclear magnetic resonance

RMSE	Root mean squared error
ROI	Region of Interest
SNR	Signal to noise ratio
TE	Echo time
TR	Repetition time
VBM	Voxel-based morphometry
WM	White matter
WMT	White matter tractography

CHAPTER 1

OUTLOOK

The Diffusion tensor (DT) is a model-based approach of describing the molecular diffusion displacement in a three-dimensional biological medium. Diffusion tensor MRI (DT-MRI) is a non-invasive method for mapping the diffusion properties in vivo. DT-MRI provides information about the magnitude and anisotropy of water diffusion in biological tissues. The simplicity of the DT model is extremely promising for a broad range of clinical and research applications; however, one caution should be used as DT-MRI is exceptionally sensitive to the noise in the acquired diffusion weighted (DW) images. This dissertation introduces and describes novel methods for reducing the effects of image of noise in DT-MRI and potential applications of anisotropic Gaussian filter construction. Anisotropic methods for the acquisition and analysis of DT-MRI are discussed. These approaches are promising for reducing the effects of noise in the computed DT-MRI maps. Further, potential applications of anisotropic image analysis are discussed. An outline summary of this thesis is described here.

Chapter 2 reviews fundamental MRI physics and introduces DT-MRI. Formulations of detecting MR signal based on the Block equation and imaging principles are summarized in brief. The phenomenon of water diffusion in biological tissues is

discussed and the methodology of DT-MRI is described.

Chapter 3 introduces a method to minimize the errors in DT-MRI measures by modifying the diffusion weighting as a function of diffusion encoding direction; thus the diffusion-weighting is anisotropic. The basic mathematical formulation is based on a model of noise propagation. The multivariate variables for this optimization problem are the directional diffusitivities from a set of user-defined diffusion sensitizing gradients. The propagated error in the variance of diffusion tensor measurements can be minimized if these directional diffusitivities are known a priori since the variance of diffusion tensor measurements (fractional anisotropy or mean diffusitivity) is a function of directional diffusitivities. In fact, the expression of co-variance of FA in terms of directional diffusitivity measurements is the core of this chapter.

Chapter 4 compares several spatial filtering methods for DT-MRI data. The problem of spatial filtering in a tensor field image has not been widely explored to date in the DT-MRI literatures. In this study, isotropic Gaussian smoothing is compared with two anisotropic smoothing methods including a new approach which uses a blurring kernel based upon the local diffusion tensor. The performance of these filters for reducing errors (noise and bias) in DT-MRI maps is compared in both measured in vivo human brain data and synthetic DT-MRI data.

Chapter 5 introduces an application of anisotropic Gaussian smoothing for voxel-based methods for DT-MRI group analysis. The method was applied to DT-MRI data from a group of autism spectrum subjects compared with normal control subjects. In typical voxel-based analysis, isotropic Gaussian blurring is applied to improve spatial co-alignment between images and application of random field theory. In this study,

anisotropic Gaussian blurring was used to minimize the mixing of signals between anatomical structures. The results from anisotropic smoothing show more consistency with the results with ROI analysis in the corpus callosum.

Chapter 6 discusses another application of the anisotropic Gaussian kernel smoothing for mapping anatomic brain connectivity. In this approach Gaussian convolution is assumed to be a local approximation of the solution to the diffusion equation (also called the heat equation), a method for diffusion propagation that is estimated from the DT-MRI data. A simulation of physical diffusion phenomenon based upon the measured diffusion tensor gives a connection probability to every voxel in the three-dimensional data. A transitional probability value at each voxel may be considered as a likelihood of reaching each voxel from a starting point of the propagation.

Chapter 7 summarizes the key observations from all chapters and discusses potential future directions.

CHAPTER 2

DIFFUSION TENSOR MAGNETIC RESONANCE IMAGING

2.1 Introduction

This chapter reviews the fundamentals of magnetic resonance imaging (MRI) and introduces the theory and methods for diffusion tensor magnetic resonance imaging (DT-MRI).

Nuclear magnetic resonance (NMR) was first illustrated by F. Block and E. M. Purcell in 1946. NMR is achieved by exciting nuclei in an externally applied magnetic field. The detectable MR (*N* is usually dropped from *N*MR since many people are alarmed by the word "nuclear") signal is not created by a single nucleus but by an enormous number of nuclei- an ensemble. This ensemble driven phenomenon allows us to demonstrate and to study the MR phenomenon via classical vector models without having to resort to partial-differential wave equations in modern quantum mechanics.

MR has been utilized in many fields of science. One of the most successful applications of MR is magnetic resonance imaging (MRI)- sometimes called the most innovative medical diagnosis tools.

In the following sections, MR signal detection, image reconstruction, and diffusion are reviewed.

2.2 Magnetic resonance signal in Block equation

The spin angular momentum of a nucleus with a spin number ½ (see the Table 2-1) has two energy states (+1/2, and -1/2). Each nuclei magnetic moment $\vec{m}$ in the presence of an applied magnetic filed is governed by the relationship of (2-1)

$$\vec{t} = \vec{m} \times \vec{B} \tag{2-1}$$

where $\vec{B}$ represents the magnetic field strength, and $\vec{t}$ is the torque experienced by the magnetic moment $\vec{m}$. Thermo-mechanics can help us to detect that a portion of the net $\sum \vec{m}$ is in the direction of the applied field $\vec{B}$, and the resultant magnetic moment per unit volume can be symbolized as magnetization $\vec{M}$. The time dependent behavior of $\vec{M}$ in the presence of an applied magnetic filed can be derived as in (2-2) using $\vec{t} = \frac{d\vec{J}}{dt}$ and

$$\vec{m} = g\vec{J}$$

$$\frac{d\vec{M}}{dt} = g \ \vec{M} \times \vec{B} \tag{2-2}$$

The Bloch equation (2-2) describes that the vector $\frac{d\vec{M}}{dt}$ is always oriented perpendicular to the plane of $\vec{B}$ and $\vec{M}$, which leads to the precession movement of $\vec{M}$ with the precession rate being dependent on the strength of the magnetic field $\vec{B}$. This unique angular frequency of nuclear precession is called Larmor frequency w_0

$$w_0 = g \ B_0 \tag{2-3}$$

Table 2-1. Properties of some NMR-Active Nuclei [Liang and Lauterbur, 1999]

Nucleus	Spin	Relative Sensitivity	Gyromagnetic Ratio (MHz/T)
^{1}H	1/2	1.000	42.58
^{13}C	1/2	0.016	10.71
^{19}F	1/2	0.870	40.05
^{31}P	1/2	0.093	11.26

Usually the total magnetic field is composed of three components [Nishimura, 1996]

$$\left(\frac{d\vec{M}}{dt}\right)_{B_0} + \left(\frac{d\vec{M}}{dt}\right)_{dB,G,B_1} = g\ \left(\vec{M} \times \left(B_0 + dB + \vec{k}(\vec{G}\cdot\vec{r}) + \vec{B}_1\right)\right) \qquad (2\text{-}4)$$

The gradient field $\vec{G}$ is essential to creating 2D or 3D images and always in the z direction, parallel to the $\vec{B}_0$. The gradient field is discussed in the next section. $\vec{B}_1$ is a shot-time varying magnetic field that is perpendicular to the $\vec{B}_0$

Relaxation is an important descriptive parameter for the time evolution of magnetization in the two directions. When a $\vec{B}_1$ field at the Larmor frequency is applied to the system, the magnetization is perturbed and flipped in the classical vector models. The perturbed magnetization shortly recovers the equilibrium. The recovery time frame is unique for the object of nuclei ensemble, and can be characterized with two parameters. The first parameter, T_1, describes the spin-lattice relaxation, or longitudinal relaxation. It

is mathematically described by:

$$\frac{d\vec{M}_z(t)}{dt} = -\frac{M_z(t) - M_0}{T_1} \qquad (2\text{-}5)$$

where $Mz(t)$ is the longitudinal magnetization at time t and M_0 is the initial longitudinal magnetization.

The second parameter, T_2, describes the spin-spin relaxation or the transverse relaxation. The characteristic decay time T_2 causes the transverse magnetization M_T that is perpendicular to the main magnetic field to relax back to zero by dephasing the individual spins :

$$\frac{d\vec{M}_T(t)}{dt} = -\frac{M_T(t)}{T_2} \qquad (2\text{-}6)$$

Table 2.2 Typical brain tissue parameters measured at 1.5 T [Vlaardingerborek and Boer]

Tissue	T1(ms)	T2(ms)	relative r
White matter	510	67	0.61
Gray matter	760	77	0.69
Cerebrospinal fluid	2650	280	1.00

: r is the proton density

These two relaxation phenomena are the main source for the detectable MR signal, and are derived by Eqn (2-5) and (2-6) in the assumption of a homogeneous external magnetic field. The field inhomogeneiy which is often problematic for brain imaging causes additional signal attenuation. This is parameterized by the relaxation time $T2^*$. $T2^*$ is proportional to T2 and is also dependent on the field inhomogeneity. By combining (2-5) and (2-6) the Block equation becomes:

$$\frac{d\vec{M}}{dt} = g\ \vec{M} \times B - \frac{M_x \vec{i} + M_y \vec{j}}{T_2} - \frac{(M_z - M_z^{\,0})\vec{k}}{T_1} \qquad (2\text{-}7)$$

2.3 Signal detection and MRI reconstruction

MR signal detection is based on Faraday's law of electromagnetic induction and the principle of reciprocity. The time varying magnetic flux through a conduction loop, i.e. a receiver coil will induce an electromagnetic field in the coil.

The magnetic flux through the coil by $\vec{M}(\vec{r},t)$ is given by

$$\Phi(t) = \int_{object} \vec{B}_r(\vec{r}) \cdot \vec{M}(\vec{r},t)\ d\vec{r} \qquad (2\text{-}8)$$

According to Faraday's law of induction, the voltage $V(t)$ induced in the coil is

$$V(t) = -\frac{\P\Phi(t)}{\P t} = -\frac{\P}{\P t} \int_{object} \vec{B}_r(\vec{r}) \cdot \vec{M}(\vec{r},t)\ d\vec{r} \qquad (2\text{-}9)$$

If the receiver coil has a homogeneous reception field over the region of interest, as is often assumed, the signal expression can be further simplified

$$S(t) = \int_{object} \vec{M}_{xy}(\vec{r},0)\ e^{-i\Delta w(\vec{r})t} d\vec{r} \tag{2-10}$$

where $\Delta w(t) \cdot t$ is the phase accumulation due to the frequency shift from w_0.

The gradient field $\vec{G}$ relates specifically to the spin frequency at an object location, namely, $\vec{r}$:

$$\vec{w} = w_0 + g\vec{G} \cdot \vec{r} \tag{2-11}$$

Measured with respect to the echo time TE, t'=t-TE

$$\int_0^t w(x,y,t)dt = gG_{yn}T_y y + gG_x t\, x = k_y y + k_x x, \tag{2-12}$$

$$k_y = g\ G_{yn}T_y = g \int_0^{t'} G_{yn}(t)dt \tag{2-13}$$

$$k_x = g\ G_x\ t' = g \int_0^{t'} G_x(t)dt \tag{2-14}$$

These k_x ,and k_y define k-space. Expanding (2-10) with (2-11) through (2-14), the signal can be expressed as a function of k_x ,and k_y (2-15)

$$S(t) \propto \int_{object} r(x,y)\ e^{-i2p(k_x x + k_y y)} dxdy \tag{2-15}$$

2.4 Diffusion

Diffusion refers to a macroscopic manifestation of Brownian motion, which was first studied by Robert Brown in the early 19th century. The Brownian motion refers to the random movement of particles in a medium, and the trajectories of the motion are continuous. If the motion is described in a discrete fashion, it may be called as random walk process.

One way of mathematically relating Brownian motion to the diffusion equation is summarized in the Appendix A. A derivation of the diffusion equation from a random walk is discussed in the Appendix B. Those two approaches (Appendix A and B) constitute the background theory for the Chapter 6: probabilistic connectivity via diffusion process.

The diffusion equation can also be obtained using Fick's law that relates the bulk diffusion flux $\vec{J}$ to the concentration gradient ∇C through an apparent bulk diffusion coefficient D.

$$\vec{J} = -D\nabla C, \qquad C: \text{the concentration gradient} \tag{2-16}$$

Combining the Fick's law (2-16) with the equation of conservation of mass Eqn. (2-17),

$$\nabla \cdot \vec{J} = -\frac{\partial C}{\partial t} \tag{2-17}$$

The diffusion equation is obtained as

$$\frac{\partial C}{\partial t} = \nabla \cdot (D \nabla C) \tag{2-18}$$

One solution to the diffusion equation is given by the Gaussian function

$$C(\vec{r}, t) = \left(\frac{1}{\sqrt{4pDt}} \right)^3 \exp\left(\frac{-(\vec{r} - r_0) \cdot (\vec{r} - r_0)}{4Dt} \right) \tag{2-19}$$

in which, the diffusion coefficient D may be theoretically derived. This was done by Albert Einstein using kinetic theory. D may be experimentally measured in several ways. The next section discusses measuring D using MR experiments.

2.5 Modified Block equation with diffusion and DT-MRI

Diffusion tensor magnetic resonance imaging (DT-MRI) is built on the assumption that three-dimensional diffusion phenomenon of water molecular ensembles can be assessed and described with diffusion tensor on a voxel basis. The diffusion tensor has been proved to be a particularly successful and useful model in brain imaging for describing the microstructure of the biological tissues using MR imaging.

As already mentioned in the previous section, the NMR phenomenon is created by an ensemble of nuclei. Thermal physics tells us that the particles are always thermally agitated and the associated kinetic energy is proportional to the environmental temperature. Therefore, if the temperature is not at absolute zero, the system is not static.

Since anything we can measure in reality exists at some temperature above zero the Block equation should involve the diffusion considerations.

A non-invasive method for measuring diffusion in biological system has been done by modeling the Block equations with diffusion motion. In a bipolar pulsed-gradient experiment [Fig 2-2], which was developed based upon a spin echo EPI pulse sequence [Fig 2-1], the interval of two diffusion sensitizing gradients (Δ) leads to the added dissipation of transverse phase by individual spin's random displacements and the resultant signal attenuation can be derived as follows [Stejskal and Tanner, 1965]

$$\frac{d\vec{M}}{dt} = g\ \ \vec{M} \times B - \frac{M_x \vec{i} + M_y \vec{j}}{T_2} - \frac{(M_z - M_z{}^0)\vec{k}}{T_1} + \nabla \cdot (D \nabla \vec{M}) \qquad (2\text{-}20)$$

where D is the diffusion coefficient.

The solution of this equation is given by:

$$M(\vec{r}, t) = M(t = 0) \cdot \exp(-\frac{1}{T_2}) \cdot \exp(-i\vec{r} \cdot \vec{k}(t)) \exp(-\int_0^t \vec{k}(t')' D \vec{k}(t') dt') \qquad (2\text{-}21)$$

where $\vec{k}(t) = g \int_0^t G(t') dt'$,

Ignoring T2 attenuation, the total magnetization ratio at time TE may be expressed in Eqn (2-21) as

$$\frac{M(TE)}{M_0} = \exp(-bD), \qquad (2\text{-}22)$$

where $b = \int_0^{TE} \vec{k}(t') \cdot \vec{k}(t') dt'$,

If anisotropic Gaussian diffusion in 3D space is considered, a tensor model may be employed, and the equation (2-22) above becomes

$$\frac{M(TE)}{M_0} = \exp(-b\vec{g}'\overline{D}\vec{g}), \qquad (2\text{-}23)$$

where $\overline{D}$ is a 3x3 tensor and $\vec{g}$ is a unit vector that represents the direction of the diffusion encoding gradient. More information on diffusion tensor formalism and its invariant measures can be found in the Appendix C. Assuming that water molecules are electromagnetically neutral, which leads to $\overline{D}$ being a symmetric tensor, solving the six unknown tensor elements requires at least six different $\vec{g}$ orientations; If more than six encoding directions are used, Eqn (2-23) becomes an over-determined equation. That can be solved by multivariate linear regression or non-linear regression. In this dissertation, all DT-MRI studies are based on twelve diffusion sensitizing encoding directions [Hasan et al 2001a] and Eqn (2-23) was solved using the singular value decomposition with linear regression.

In the Stejskal-Tanner scheme (Fig 2-2), commonly employed for DT-MRI experiments, the b value (or b factor, diffusion weighting) is summarized as follows [Mattiello et al., 1997]

$$b = g^2 G^2 d^2 (\Delta - d/3), \qquad (2\text{-}24)$$

where g is the gyromagnetic ratio, d is the duration of the diffusion sensitizing gradient and Δ is the separation time of the two diffusion sensitizing gradient G.

Conventional DT-MRI uses the same b value (2-25) for each encoding direction. Utilizing different b values per encoding direction is the subject of Chapter 3 and the solution of the diffusion equation- the Gaussian function (2-20), is exercised in the rest of the chapters.

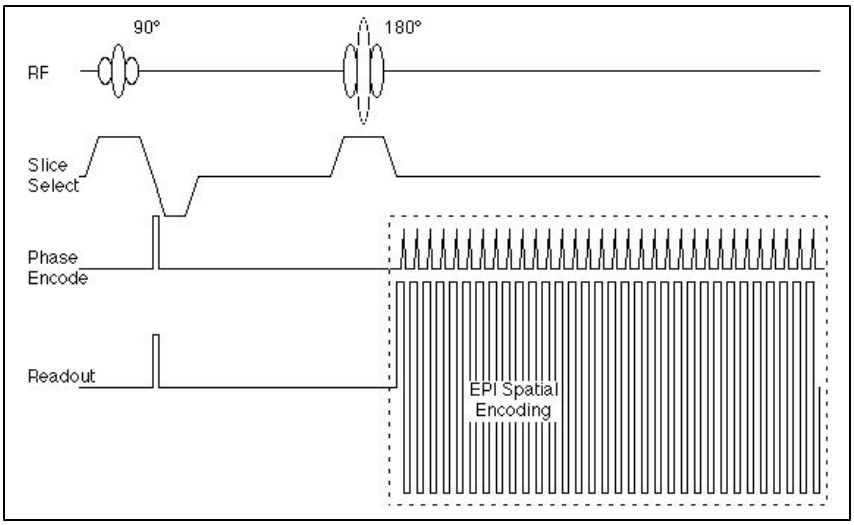

Fig 2-1 Spin echo EPI pulse schematics. EPI was developed by P. Mansfield [Mansfield, 1977]. EPI is a fast MRI technique to acquire an image in only a single or very few excitations.

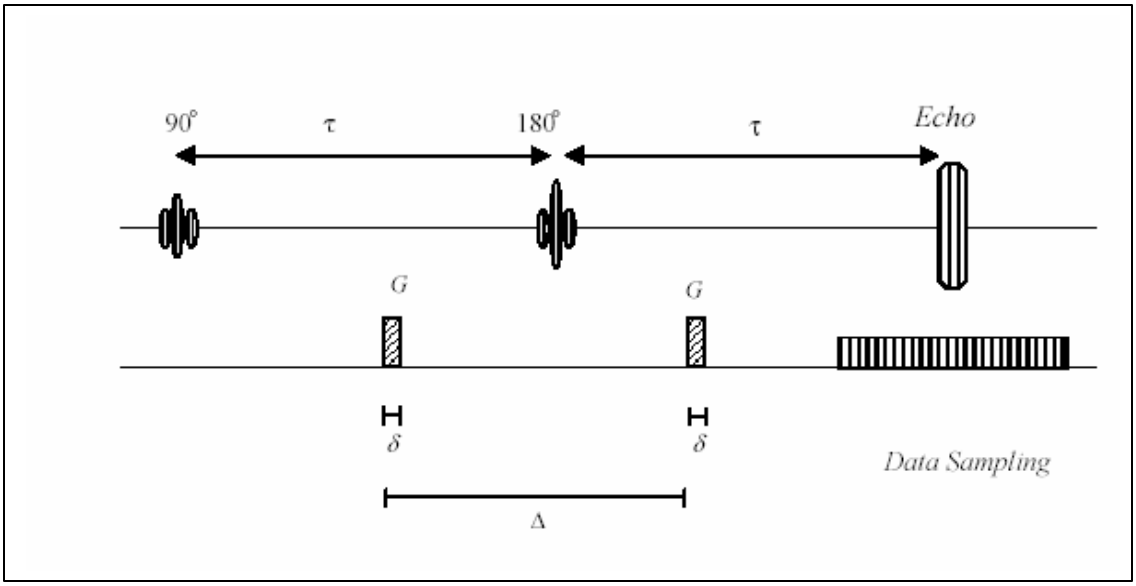

Fig 2-2. Stejskal-Tanner sequence. After a 90° RF pulse, the left side diffusion gradient G is on over a short period d and another RF pulse 180° is applied to precede the right side diffusion gradient G. Two diffusion sensitizing gradients G are separated by the time interval Δ. G, d and Δ affect the total amount of diffusion related signal attenuation on the sampled data at the echo time.

CHAPTER 3

OPTIMIZATION OF DIFFUSION TENSOR ENCODING WITH ANISOTROPIC DIFFUSION WEIGHTING

3.1 Introduction

Diffusion tensor MRI and the associated measures, such as fractional anisotropy (FA), mean diffusitivity (MD), and eigenvector directions, are highly sensitive to image measurement noise. The main strategy to decrease noise sensitivity is to employ uniformly distributed diffusion encoding directions with a diffusion-weighting value that is nearly optimum for the mean diffusivity. [Papadakis N.G et al., 1999; Jones DK et al, 1999; Armitage et al., 2001; Hasan K.M. et al., 2001] These approaches make sense for the case where the diffusion tensor distributions and directions are arbitrary or unknown. However, in the case where the diffusion tensor shape and orientation in a specific region may be estimated a priori, such as in the corpus callosum, the corticospinal tract, or the spinal cord, it may be possible to make more precise measurements in that region by using an anisotropic diffusion-weighting scheme. In this study, the diffusion weighting was optimized for each encoding direction to minimize the error in FA measurements of the corpus callosum.

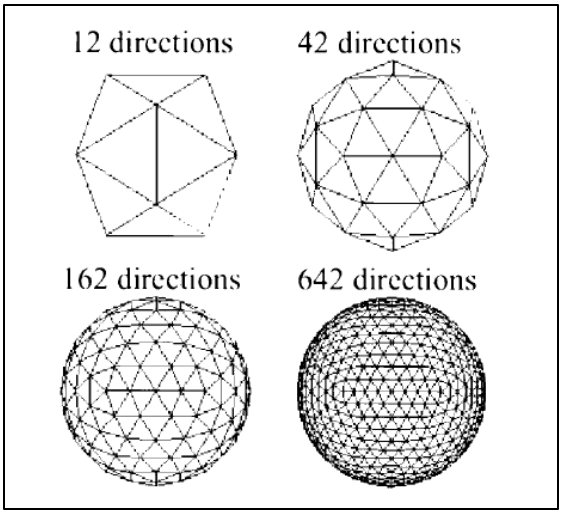

Fig 3-1 Examples of directional sampling schemes. [Le Bihan et al., 2001]. Conventionally diffusion sensitizing encoding directions are set to be uniformly distributed and a single diffusion weighting factor is used for all directions.

3.2 Theory

The diffusion to noise ratio (DNR) introduced by Xing et al [Xing et al., 1997] is defined as:

$$DNR = \frac{D}{s_D} = SNRk_D \text{ , where } k_D = \frac{bD}{\sqrt{1+\exp(2bD)}} \tag{3-1}$$

where D represents the diffusitivity, b the diffusion weighting, and s_D the standard deviation of diffusitivity.

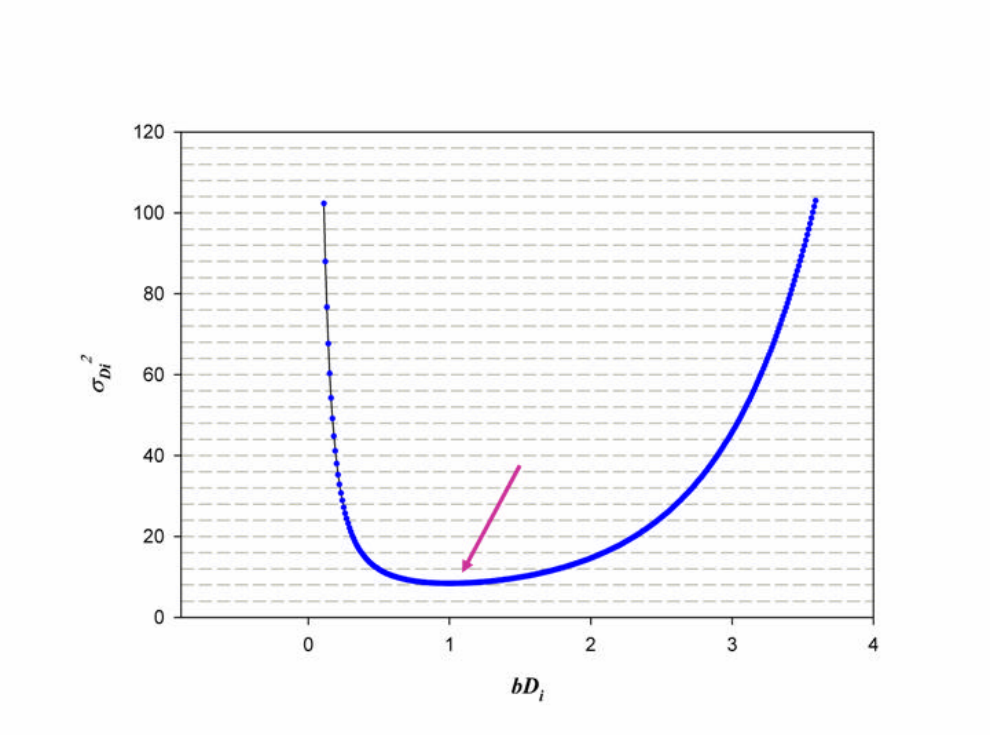

Fig 3-2. Plot of s_{D}^{2} as a function of bD_i. s_{D}^{2} is minimized at $bD_i \sim 1.1$

The measured diffusitivity variance (Fig 3.2) can be plotted as a function of bD_i, and the function has a global minimum at $bD_i \sim 1.1$.

Since the diffusion-weighted image in each direction is considered to be independent in the diffusion tensor-encoding scheme, the DNR in each direction i can be denoted as D_i / s_{D_i}. Consequently, an invariant function, i.e., a function of eigenvalues can be expressed as a function of the measurement of D_i. MD and FA variance optimizations are constructed as follows.

MD optimization in the anisotropic scheme

The variance of MD may be expressed as:

$$s^{2}_{MD} = \sum_{i}^{n}\left(\frac{\partial MD}{\partial D_i}\right)^2 s^{2}_{D_i} + 2\sum_{j\neq i}^{n}\sum_{i}^{n}\left(\frac{\partial^2 MD}{\partial D_j \partial D_i}\right) s^{2}_{D_i D_j} \qquad (3\text{-}2)$$

MD is a linear summation of D_i which makes the second term in (3-2) to vanish. This means, each D_i optimization, i.e. minimization of $s^{2}_{D_i}$, will lead to MD optimization.

Since MD is the first order of diffusitivity variables D_i the variance is easily derived. It turns out to be the same as DNR calculated above since the $G^{-1}{}_{1,2,3,j}$ in Eqn (3-3) is a scalar factor.

$$MD = \frac{D_{xx} + D_{yy} + D_{zz}}{3} = \frac{\sum_{j=1}^{N} G^{-1}{}_{1,j} D_j + \sum_{j=1}^{N} G^{-1}{}_{2,j} D_j + \sum_{j=1}^{N} G^{-1}{}_{3,j} D_j}{3} \qquad (3\text{-}3)$$

FA optimization

Unlike the MD variance described above, the FA variance has a non-zero second term in (3-2) due to the fact that FA is the second order function of D_i. Detailed derivation is described in the Appendix C.

If FA is expressed as a function of D_i, the variance FA has the following form.

$$s^{2}_{FA} = \sum_{i}^{n}\left(\frac{\partial FA}{\partial D_i}\right)^{2} s^{2}_{D_i} + 2\sum_{j\neq i}^{n}\sum_{i}^{n}\left(\frac{\partial^{2} FA}{\partial D_j \partial D_i}\right) s^{2}_{D_i D_j} \qquad \text{(3-4 a)}$$

$$\text{where} \quad s^{2}_{D_i D_j} = \frac{s^{2}_{S_0}}{S_0^{2}} \frac{1}{b_i b_j} \quad \text{(Appendix C)} \qquad \text{(3-4 b)}$$

The s^{2}_{FA} is a function of diffusitivities D_i and b factors b_i. The highlight of this chapter is in fact derivation of (3-4b) which shows that the covariance from two independent directional diffusitivities is related to the diffusion weighting factors. Obviously if the two diffusion weighting factors are large, the covariance of the directional diffusitivity becomes negligible.

Once the ROI is chosen, its representative D_i is inserted into (3-4) then s^{2}_{FA} is expressed as a multivariate quadratic function (3-5)

$s^{2}_{FA} = f(b_i), i = 1 \cdots N$, N = number of encoding directions. (3-5)

Any multivariate minimization algorithm, such as the direction set method, which doesn't require derivatives, may be implemented to find the minimum s^{2}_{FA} [Lee and Alexander, 2004].

3.3 Methods

The method that was used in this study involves error/noise propagation through Taylor expansions to calculate the error (variance) function, *f=f(diffusitivities, b factors)*, and a multivariate optimization algorithm to find the minimum of the error function.

A single-shot spin echo EPI sequence with diffusion-tensor encoding (12 directions (optimized using minimum energy criterion [Hasan et al 2001a]), & b = 1000s/mm^2) was used to estimate the diffusion tensor of the corpus callosum. A region of interest (ROI) in the corpus callosum, which is the largest white matter pathway consisting mostly of contralateral axon projections that are made up of about 200-250 million nerve fibers, was selected manually. Only voxels with FA > 0.6 and the x component of the major eigenvector> 0.9 retained. The measured diffusitivities of these voxels were averaged for each encoding direction to estimate a representative set of directional diffusitivities in the corpus callosum [Table 3-1]. Powell's optimization method was used to estimate the twelve directionally optimum b factors by minimizing the variance of FA. The optimum diffusion weighting for each direction is listed in Table 1-1. Note that the optimum directional diffusion weightings ranged between 595 and 2014 s/mm^2. In order to achieve the necessary diffusion weighting for the anisotropically optimized encoding set, the times Δ (interval between the two diffusion gradient pulses), and δ (the diffusion gradient pulse duration) were increased from 21 ms to 26.2 ms and from 27.4 ms to 32.2 ms, respectively. A subsequent diffusion tensor scan was performed on the same subject using both with the isotropic diffusion-weighting (b = 1000 s/mm^2) and the optimized anisotropic diffusion-weighting scheme listed in Table 3-1. The scan was repeated nine times for each set of encoding weightings to estimate the variance in FA for the region that was selected (FA>0.6, ex >0.9) in the corpus callosum.

3.4 Results

Simulation

The error propagation in simulation predicted that the variance in FA should decrease by 56% using the anisotropic diffusion-weighting (shown in red plot, Fig 3-3). A set of FA optimized b factors was inserted to the Eqn. (3-2) to see the impact on MD variance. The reduction rate of the MD variance was close to the FA variance reduction (shown in blue plot, Fig 3-3) indicating that using the FA optimizing b factors may be also beneficial to optimizing MD measurements.

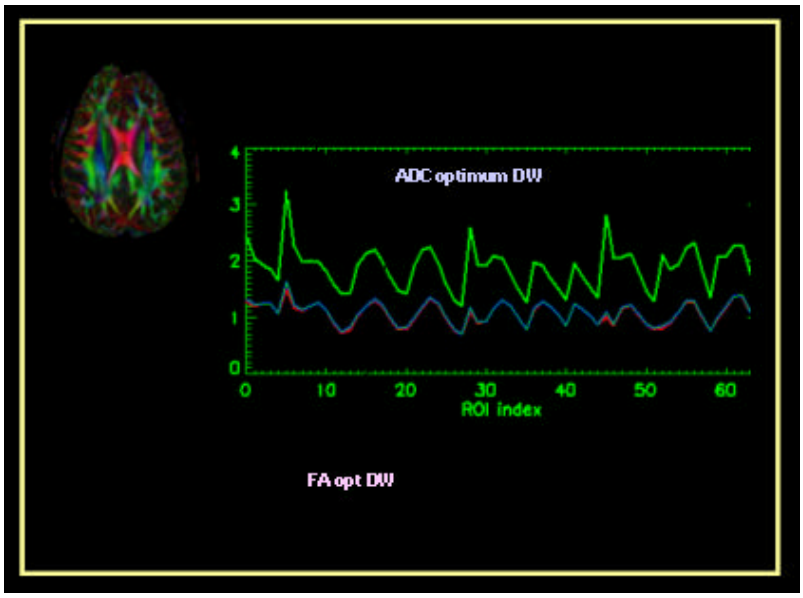

Fig 3-3 simulation results using the optimum diffusion weighting that are listed in the Table 3-1.The line in green is the variance by using b=1000 s/mm^2 isotropically, and the red line indicates the variance of FA by using anisotropic b factors listed in the table 3-1. The blue line is the consequent MD variance by using the same b factors that were optimized for FA.

Table 3-1. Encoding directions, average diffusitivities from ROI, their standard deviation, and optimum diffusion weightings

Gx	Gy	Gz	Mean ($x10^{-3}$)	Std dev ($x10^{-3}$)	FA optimized b factors
0.418	0.824	0.383	0.568	0.0921	1759
0.502	0.568	0.652	1.11	0.187	1033
0.144	-0.429	-0.891	0.562	0.0458	1968
0.698	0.048	-0.714	0.988	0.220	825
-0.090	-0.829	0.552	0.649	0.0645	2014
-0.224	-0.964	-0.142	0.738	0.0751	1954
0.953	0.194	0.234	1.91	0.208	510
0.617	-0.166	0.769	1.08	0.200	872
-0.918	0.354	0.180	1.36	0.185	595
-0.577	0.740	-0.344	0.741	0.0860	1104
0.048	0.276	-0.960	0.525	0.0737	1971
-0.735	-0.617	0.282	1.38	0.156	623

ROI based analysis

Fig 3-4 shows an example of how voxel based analysis was done. In most cases, the FA variance was noticeably larger when using the isotropic diffusion weighting factor of 1000 s/mm^2 than when using the optimum diffusion weighting factors in the corpus callosum area. The variance of the collection of voxels was estimated in the ROI shown in the Fig 3-5. The ROI was manually drawn in the corpus callosum region with the same threshold when the optimum diffusion weighting factor scheme was performed in the method section. The x axis in the plot indicates the ROI (voxel index) and each bar represents the standard deviation over the nine acquisition period. A significant reduction in the variance was observed using the anisotropic diffusion weighting scheme.

In addition to the reduction of the FA variance, new optimum b factors decreased the residual error $\sum_i | D_i (= \frac{\ln S_o - \ln S_i}{b_i}) - g_i{}^T \overline{D} g_i |$ in the corpus callosum region from ~2.5 to ~2.1. This fact ensures a better fitting to the single tensor model with the optimum b

factors.

Visualization of images

The optimum tensor encoding was applied to four other subjects and similar results were obtained. Axial FA maps through the body of the corpus callosum for isotropic diffusion-weighting and the optimized anisotropic diffusion-weighting are shown in Fig 3-6. In general, the corpus callosum appears fuller and less noisy in the FA image obtained with anisotropic diffusion-weighting. The other white matter regions, however, appear blurrier and noisier. The variances of the FA maps across the nine runs are shown in Fig 3-6. The variance in the corpus callosum is lower for anisotropic diffusion-weighting but higher in most other brain regions. The overall reduction of the FA variance in the corpus callosum region using optimum b factors was threefold.

3.5 Conclusions

Optimizing the diffusion-weighting for individual encoding directions was found to reduce the variances of FA measurements in regions where there was an a priori estimate of the apparent water diffusion tensor. However, as expected, in regions where the diffusion tensor was not similar to the optimization case, the accuracy tended to be similar or worse.

The sensitivity of the anisotropic encoding to slight variations in tensor shape and orientation is unknown. In addition to the corpus callosum, this method may be useful for studies of other white matter regions that are relatively homogeneous and the

approximate direction is known before the experiment, such as the spinal cord and the corticospinal tract.

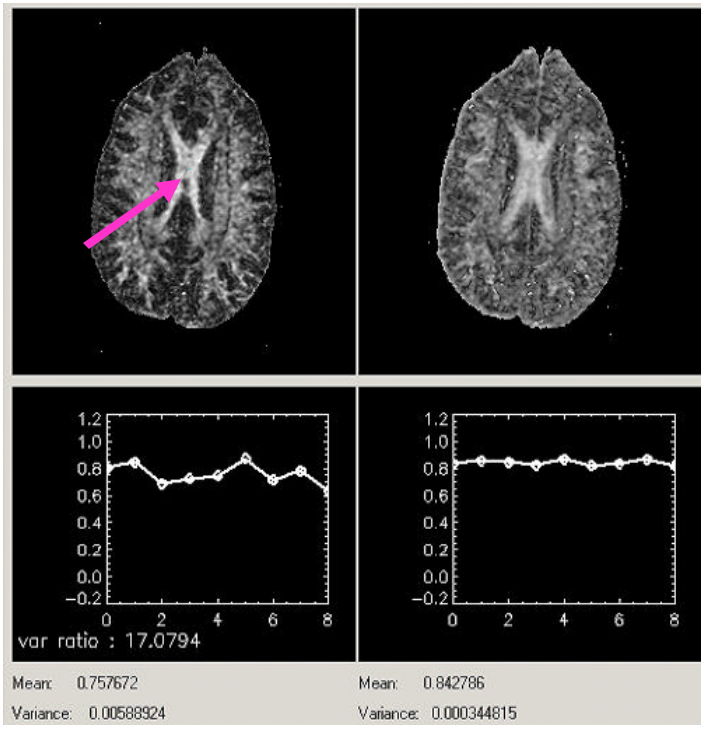

Fig 3-4 An example of voxel based analysis using the optimum diffusion weightings that are listed in the table 3-1. As shown in the bottom left plot of the figure, the FA value at a voxel fluctuates over the time series when using an isotropic diffusion weighting factor 1000 s/mm^2. Using the optimum diffusion weighting factor, FA variance was significantly reduced (bottom, right).

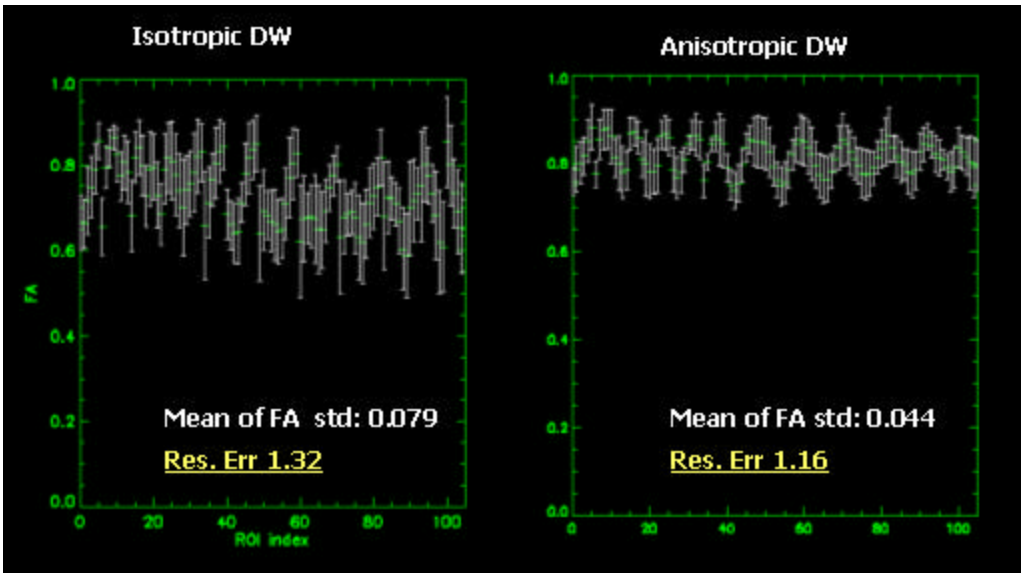

Fig 3-5 ROI analysis using the optimum diffusion weightings that are listed in the table 3-1. Each bar represents the standard deviation over nine time series. The standard deviation was noticeably reduced using anisotropic diffusion weighting schemes.

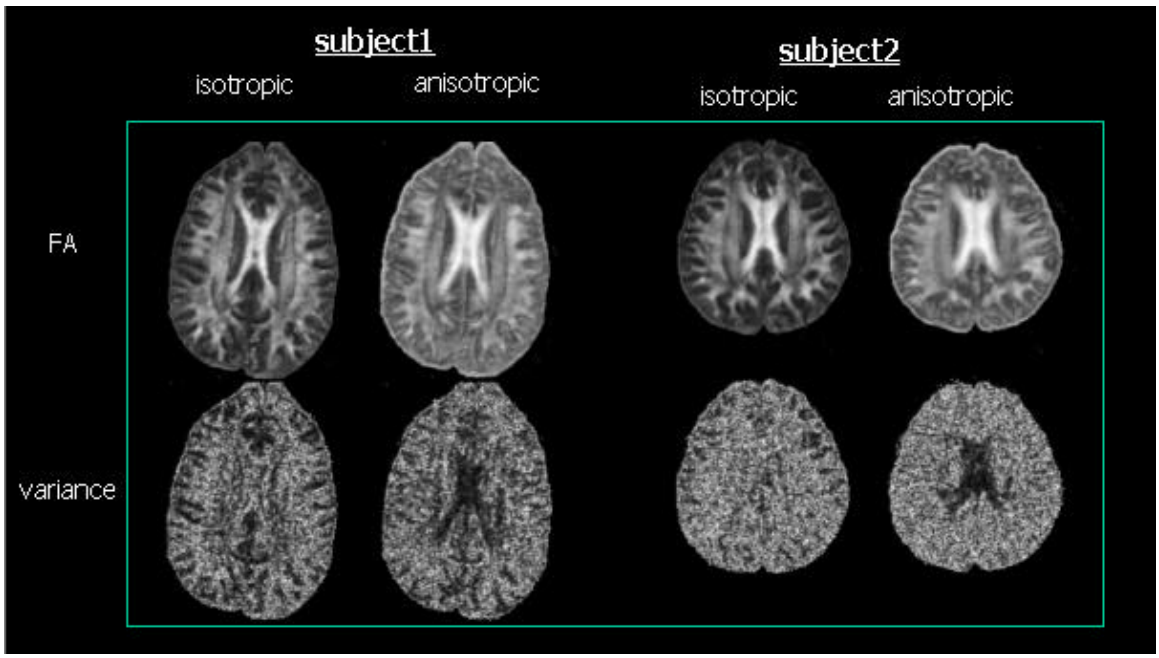

Fig 3-6 The top row: FA maps using b= 1000 s/mm2 vs. FA map using optimum b factors listed in the Table 3-1. The bottom row: the variance map of FA over repeated measurements using conventional b factors vs. the variance map of FA using optimum b factors. Significantly lower variance was observed in the CC using the anisotropic diffusion scheme.

CHAPTER 4

NOISE FIILTERING FOR DT-MRI

4.1 Introduction

The high sensitivity of DT-MRI to noise and error in the DW images may be locally reduced by using the anisotropic diffusion weighting scheme discussed in the previous chapter. However, the local error minimization from Chapter 3 is only optimal for a specific tensor shape and orientation which must be known a priori. Therefore it might not be useful for the whole brain assessment because its directional diffusitivity would be different from region to region. To target the general heterogeneous region, increasing the number of averaging DW data can substantially increase the SNR, yet in certain cases (e.g., young children, anxious or claustrophobic subjects, etc.) it may be desirable to minimize the acquisition time of the DT-MRI protocol. Lowering the spatial resolution might increase the SNR, but obviously, the spatial resolution should be improved to reduce partial volume averaging and to study the anatomy with greater detail [Alexander et al, 2001]. Consequently, either the reduction of scan time (e.g., fewer averages or encoding directions) or the acquisition of images with smaller voxel dimensions will significantly reduce the SNR of DT-MRI measurements, thereby

affecting the accuracy. Reduced SNR will not only increase the variance of the diffusivities, anisotropy, and eigenvector directions, but will also induce biases into the eigenvalues and anisotropy measures [Pierpaoli and Basser, 1996; Basser and Pajevic, 2000]. The sorting bias of eigenvalues in noisy DT-MRI data causes a systematic overestimation of the largest eigenvalues and an underestimation of the smallest eigenvalues [Anderson, 2001].

In this chapter, a more reliable method to decrease the noise in DT-MRI through post processing is discussed and anisotropic Gaussian smoothing using the diffusion tensor at each voxel as the anisotropic diffusion kernel is proposed. The application of the diffusion tensor as a convolution kernel will inherently smooth the data more in the direction of greater diffusivity which is generally parallel to the orientation of white matter tracts in the brain. Conversely, in gray matter areas, which demonstrate more isotropic diffusion, the smoothing will also be more isotropic. The anisotropic kernel smoothing approaches are compared against isotropic Gaussian smoothing and the Perona Malik filtering algorithm. Comparisons of filtering applied directly to the diffusion weighted data and to the estimated diffusion tensor elements are performed. The performance of each spatial filtering method is evaluated as a function of SNR in in-vivo high- resolution human DT-MRI data using the root mean squared error (RMSE) that describes the accuracy and variance of the diffusion tensor measures.

4.2 Theory

Image filtering and smoothing methods may be used to reduce noise in medical images. However, certain types of smoothing may also blur important image features and the edges of structures. Fine image features and edges may be preserved using anisotropic diffusion filtering methods such as Perona-Malik (PM) algorithm [Perona and Malik, 1990]. Note that anisotropic diffusion here refers to the image filter used and not the anisotropy from the diffusion tensor. The PM filter was originally developed for scalar images and methods for smoothing DT-MRI data may require more complex approaches than scalar image smoothing methods, because the diffusion tensor image data is multidimensional and represents spatially coherent directional information by the eigenvectors and eigenvalues. In this section, several smoothing algorithms are discussed: They are the conventional isotropic Gaussian kernel, which is mostly used in the medical image community, an anisotropic diffusion scheme using PDE to compensate for the demerits of Gaussian blurring, and anisotropic Gaussian kernel smoothing that is based on the measured diffusion tensor.

Gaussian kernel smoothing

Gaussian kernel smoothing is typically used in the field of image processing. The Gaussian convolution is a linear operator and the resultant convolved image has less noise due to the local averaging operation. The Gaussian kernel smoothing is essentially a low pass filter in that the abrupt signal intensity change, which often time is due to noise, is decreased thanks to the averaging with the neighborhood intensity values. The n-

dimensional Gaussian distribution is defined as

$$K(\vec{r}) = \frac{\exp(-\vec{r}'\vec{r}/2s^2)}{(2p)^{n/2}s^n}, \qquad \vec{r} = (r_1, r_2, \cdots, r_n)' \tag{4-1}$$

where $\vec{r}$ is the position vector, and s is the standard deviation of the distribution $K(\vec{r})$ in the *n* dimensional case.

This kernel in Eqn. (4-1) is herein called the isotropic Gaussian kernel partially because it has an isotropic shape and also in order to be compared against an anisotropic Gaussian kernel that is introduced later.

The mathematical description of Gaussian convolution is defined over the entire domain, from - 8 to + 8, or the entire grid of points of data. However, integration of the entire region for each data point is computationally overloaded, and in reality, the Gaussian decreases exponentially, a reasonable approximation could be used. For instance, integrating the kernel in the closed cube [-2.58, 2.58] leads to the value, 0.99, which is close to 1. Therefore, a limited window size is used instead of the entire domain and, which leads to the procedure that the kernel should be normalized in order to keep the total probability 1, so that the kernel K is transformed as $\tilde{K} = \frac{K}{\int_{window} K}$.

To increase the kernel size, the iterated convolution is used.

$$K_{\sqrt{n}t} = K_t \otimes K_t \otimes K_t \ldots \otimes K_t \quad \text{(n times)} \tag{4-2}$$

PDE based image smoothing : Perona Malik Algorithm

Partial differential equations (PDEs), specifically the diffusion equation (hereafter, heat equation, not to be confused with the diffusion in diffusion tensor MRI), based technique have been used for imaging processing, and the basic idea is to lessen the "diffusion", i.e., regional intensities mixing effect, where the magnitude of the gradients of the image intensity is large, so that the edges are kept to be sharp and the homogeneous area is to be smoothed relatively generously [Perona and Malik, 1990]. The "diffusion" function in most PDE based image smoothing schemes, is governed by image intensity. Eqn (4-3) is the heat equation that the Perona Malik (PM) algorithm is based on.

$$\frac{\partial I}{\partial t} = div[g(\|\nabla I\|)\nabla I] \tag{4-3}$$

where $\|\nabla I\|$ is the image intensity gradient and there are infinite numbers of degree of freedom for choosing the function g. One common characteristic that the g function must have is an inverse relationship with the image gradient $\|\nabla I\|$. Followings are examples of the function g [Catte et al., 1992]:

$g(\nabla I) = e^{-(\|\nabla I\|/l)^2}$, which tends to be better for high contrast edges over low contrast ones, and

$g(\nabla I) = \frac{1}{1+(\frac{\|\nabla I\|}{l})^N}$, which tends to better for wide regions over smaller ones.

In this study, the PM algorithm for DT-MRI is formulated as (4-4)

$$g(\|\nabla I\|) = \exp[(-\|\nabla I\| / K)^2] \quad (4\text{-}4)$$

Eqn (4-4) is from Parker et al [Parker et al., 2000].

Other Approaches

Besides applying the PM algorithm to the raw, diffusion-weighted scalar images prior to the calculation of the diffusion tensor and associated measures, Pajevic et al used a B-spline interpolation method to regularize the diffusion tensor field. More recently, several investigators have applied constrained variational principles to the full diffusion tensor data with promising results [Pajevic et al., 2002; Coulon et al., 2004; Tschumperle and Deriche 2003; Wang et al., 2003, 2004]. However, these approaches have not been widely used because they are relatively complex and the computational demands can be high. Ding et al. developed the original Weickert's method to provide a more reliable and computationally less demanding smoothing algorithm. [Weickert, 1999; Ding et al., 2005]

Gaussian kernel smoothing (revisited): Anisotropic Gaussian kernel smoothing

The anisotropic Gaussian kernel that is introduced herein is a generalization of the isotropic Gaussian kernel formalism. H is a constant matrix that linearly transforms the isotropic Gaussian function to be an anisotropic shape of Gaussian profile.

$$K_H(\vec{r}) = K(H^{-1}\vec{r})/\det(H) \quad (4\text{-}5)$$

Note that $K_H(\vec{r})$ remains as an isotropic Gaussian kernel if H is an identity matrix.

The anisotropic Gaussian kernel based on the diffusion tensor can be built on the Riemannian metric tensors for the purpose of smoothing more along the larger metric distance, such as the major eigenvalue in the diffusion tensor [Chung et al., 2003; Lee et al., 2006]. The anisotropic Gaussian kernel may be formulated as

$$K_t(\vec{r}) = \frac{\exp(-\vec{r}\overline{D}^{-1}\vec{r} / 4t)}{(4pt)^{n/2}(\det \overline{D})^{1/2}} \tag{4-6}$$

where *t* represents a dummy variable (a diffusion time) that is used to adjust a width of the kernel (4-6) and $\overline{D}$ is a diffusion tensor.

$$\overline{D} = \begin{bmatrix} 5 & 0 & 0 \\ 0 & 2 & 0 \\ 0 & 0 & 1 \end{bmatrix} \qquad \overline{D} = \begin{bmatrix} 15 & 0 & 0 \\ 0 & 6 & 0 \\ 0 & 0 & 3 \end{bmatrix}$$

Fig 4-1.The anisotropic Gaussian kernel that is projected in the x-y plane

Voxel based normalization

The tensor $\overline{D}$ should be normalized in a voxel basis in order to regularize a kernel shape for various ranges of diffusitivities. Our interest is in an anisotropic tensor shape not the magnitude of the tensor. For instance, there can be a case where two different voxels have the same anisotropy index but have different eigenvalues (Fig 4-1), which means that the ratio of eigenvalues of each voxel is constant. If each tensor is not normalized, the resultant anisotropic Gaussian kernel from the tensor that has bigger eigenvalues has a bigger bandwidth with a given t in Eqn. (4-6). Normalization can be done with the trace of the tensor or one of the maximum eigenvalues or minimum eigenvalues. In this chapter, to make a fair comparison with isotropic Gaussian kernel smoothing, the trace is used for the scale factor to regularize each diffusion tensor.

In this study, a 5 x 5 x 5 voxel window size and $t = 0.2$ were chosen for the voxel size 1mm x 1mm x 1mm. If t (or s), is small enough for the FWHM to be within one voxel, then the purpose of Gaussian kernel smoothing, local averaging, is not effectively done. Also, making t relatively big results in only the concentrated value around the peak of the Gaussian profile within the window.

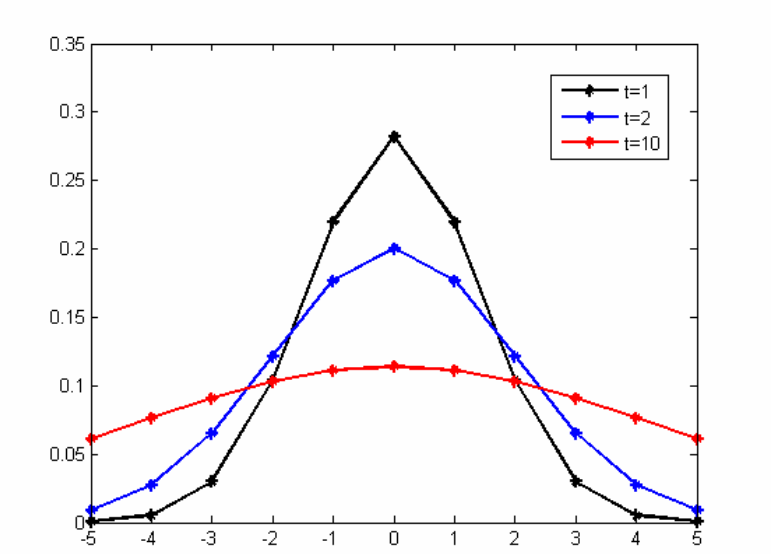

Fig 4-2. One dimensional Gaussian distribution as the diffusion time *t* increases. Each curve is normalized in such that the integral of the underneath area should be one. In a very shot time, the Gaussian profile is narrow (black, t=1) and the longer time passes, the more flattened the profile becomes. Therefore, if *t* (4-3) is too big then the distinction between different shapes of anisotropic Gaussian at each voxel would be not attainable.

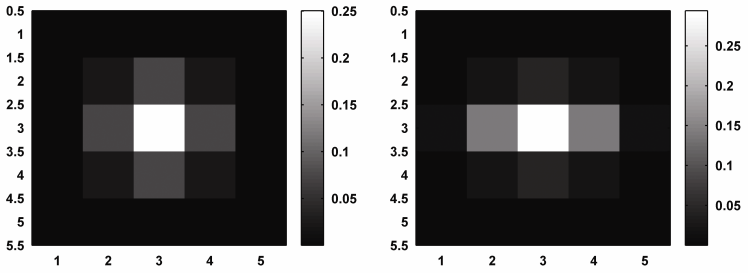

Fig 4-3. Example of smoothing kernels (x-y plane projected) for a voxel in the corpus callosum for (a) isotropic Gaussian kernel and anisotropic Gaussian kernel (b). The anisotropic kernel shows increased preferential smoothing in the x direction, which is parallel to the WM structure of the corpus callosum.

Positive Definite Constraints

A diffusion tensor is supposed to be positive definite and most regularization algorithms for DT-MRI have a constraint to keep the tensor positive definite. However, the Gaussian convolution operation doesn't affect the tensor's positiveness if the data is given as positive definite [Appendix D], so that it doesn't require any constraint. On the other hand, the PM algorithm may not hold the positiveness [Fig 4-4].

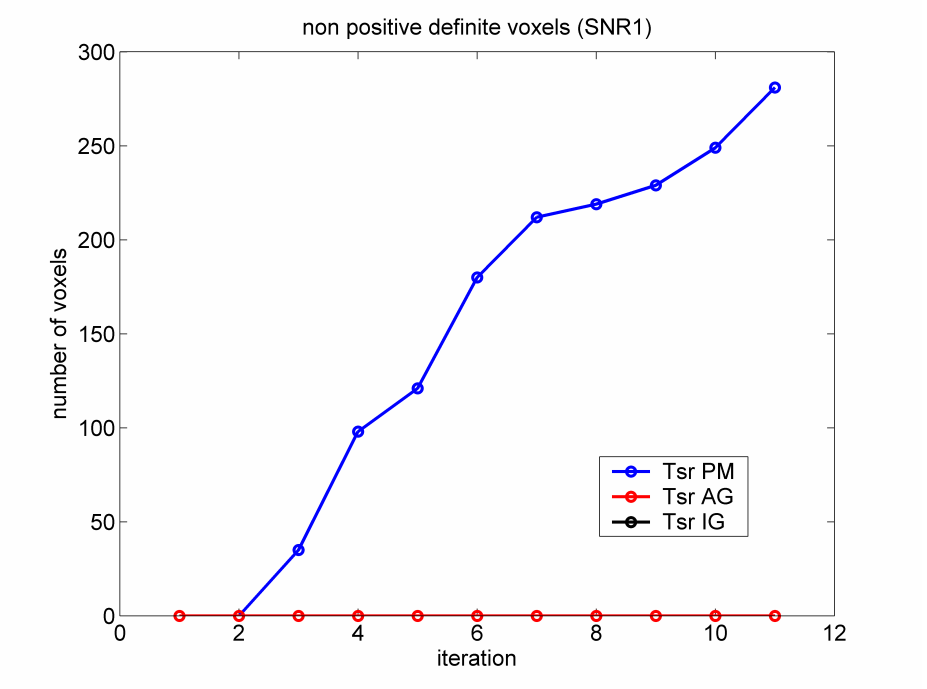

Fig 4-4. A simulation to test the preservation of positive definiteness of the diffusion tensor. Artificial noise was added to a Cholesky-decomposed matrix (L and L') of the tensor (positive definite) so that composed LL' was guaranteed to be positive definite. Gaussian smoothing and PM filtering were applied to the noisy positive definite tensor. Negative voxels were rapidly formed by PM filter (plot in blue) whereas positive definiteness was hold with Gaussian smoothing.

4.3 Methods

DTI Acquisition

DT-MRI data sets that were used for the evaluation of various smoothing algorithms addressed in this paper were obtained from a single healthy subject. The imaging was performed in accordance with the guidelines of the Institutional Review Board at university of Wisconsin. DT-MRI was performed on a 3.0 Tesla GE SIGNA (GE Healthcare; Waukesha, WI) using a diffusion-weighted, single-shot, spin echo, EPI pulse sequence with diffusion-tensor encoding in 12 directions (direction set was optimized using minimum energy criterion – Hasan et al. 2001a). The imaging protocol was: cardiac gated (effective TR = 18 heartbeats ~ 19 s), TE = 73.9 ms, 1 NEX, b = 1000 s/mm^2, slice thickness = 1.8mm (contiguous 0 mm gap), 54 contiguous axial slices, field-of-view = 230 mm, matrix = 128x128, interpolated on the scanner to 0.8984 x 0.8984 voxel dimension. The scan was repeated twelve times. Two data sets that had relatively severe head movement were excluded for the study. Image misregistrations between ten repeated data sets were corrected using the 3D affine image registration program *Flirt* in the FMRIB software library (http://fmrib.ox.ac.uk/fsl/). Ten registered data sets were used to create "gold standard" averaged data and also different levels of SNR data, such as NEX 3, NEX 6 data. The SNR of different NEX data were estimated in the high anisotropy region (FA>0.45), and is listed in Table 1.

Linear regression was used to estimate the diffusion tensor from the raw DW data. The diffusion tensors were diagonalized and maps of the mean diffusitivity (MD) and fractional anisotropy (FA) [Basser and Pierpaoli, 1996] were generated using the

numerical methods that are described in [Hasan et al., 2001b].

Evaluation of Anisotropic Smoothing

Three image filters were evaluated: an isotropic Gaussian kernel, an anisotropic Gaussian kernel based on the diffusion tensor D, and the Perona Malik (PM) algorithm. Filter performance was evaluated for application to both the original diffusion-weighted images, and the diffusion tensor elements.

Various kernel widths were investigated by using the iterative convolution in (4-2) up to ten times. The optimal diffusion time (a temporal step size for each iteration) for the Gaussian kernel and the PM smoothing was investigated with a small set of data prior to applying different types of smoothing algorithms to the entire data sets for evaluation. The optimal diffusion time t was sought in a range of values [0.01, 0.05, 0.1, 0.2…1.0] for the step size that led to the minimum RMSE of FA and each diffusion time that was used was 0.2 (s; seconds) for the lowest SNR data, and 0.1 (s) for the rest of data.

The effects of the filters on two widely used DTI measures – the fractional anisotropy (FA) and the mean diffusivity (MD = trace(D)/3) - were evaluated by estimating the root mean squared error (RMSE) at each voxel for each iteration, i, which was quantified as the root mean square error between the gold standard maps, $\tilde{x}$ and the smoothed data, $\hat{x}_i$,

$$\mathrm{RMSE}_i = \sqrt{< \sum (\tilde{x} - \hat{x}_i)^2 >} \qquad (4\text{-}7)$$

The effects of filtering on the major eigenvector orientation (the directional field) by Gaussian kernel convolution were also evaluated for voxels with high anisotropy (FA > 0.45). The average error in the major eigenvector orientation was

$$\text{ang}_i = \cos^{-1}(< \sum_n \hat{e}_1 \cdot \hat{e}_{1,i,n}) \qquad (4\text{-}8)$$

where $\hat{e}_1$ is the gold standard major eigenvector and $\hat{e}_{1,i,n}$ is the eigenvector from the nth filtered data set and *i*th iteration.

The measures were computed for the entire brain volume within the images. Regions of CSF were excluded from the analysis by using a trace threshold (trace > 0.003 mm^2/s). All specific regions of interest including global white matter and grey matter ROIs were extracted using the software *SPAMALIZE* *http://brainimaging.waisman.wisc.edu/~oakes/spam/spam_frames.htm* by T. Oakes.

Simulated Data Analysis

The gold standard used in the real image data is non-ideal in that it still has some degree of noise and error. In order to evaluate the filter performance relative to a true gold standard, we developed a realistic synthetic data set by taking a high quality DTI data set (SNR ~ 60) of a different subject with slightly different imaging parameters (3T; a quadrature birdcage headcoil; twelve diffusion-weighted encoding directions at b = 1000 s/mm^2 plus a non-diffusion weighted reference image (b = 0); peripheral pulse gating (TR was 13 heartbeats ~ 15s); eight repeated scans with magnitude averaging; 39 contiguous 3 mm thick slices; voxel dimensions = 0.9375 x 0.9375 x 3.0 mm). To make

the noise ‘texture’ of the gold standard data smoother, a small degree of smoothing was performed using a single iteration of the isotropic Gaussian filter. Noisy data sets at different levels were synthesized by adding zero-mean normal random noise with a range of standard deviations. The SNRs of the image sets were estimated in regions of high anisotropy (FA>0.45), and were between 15 and 77. The filter performance with the same methodology described in the previous section was applied.

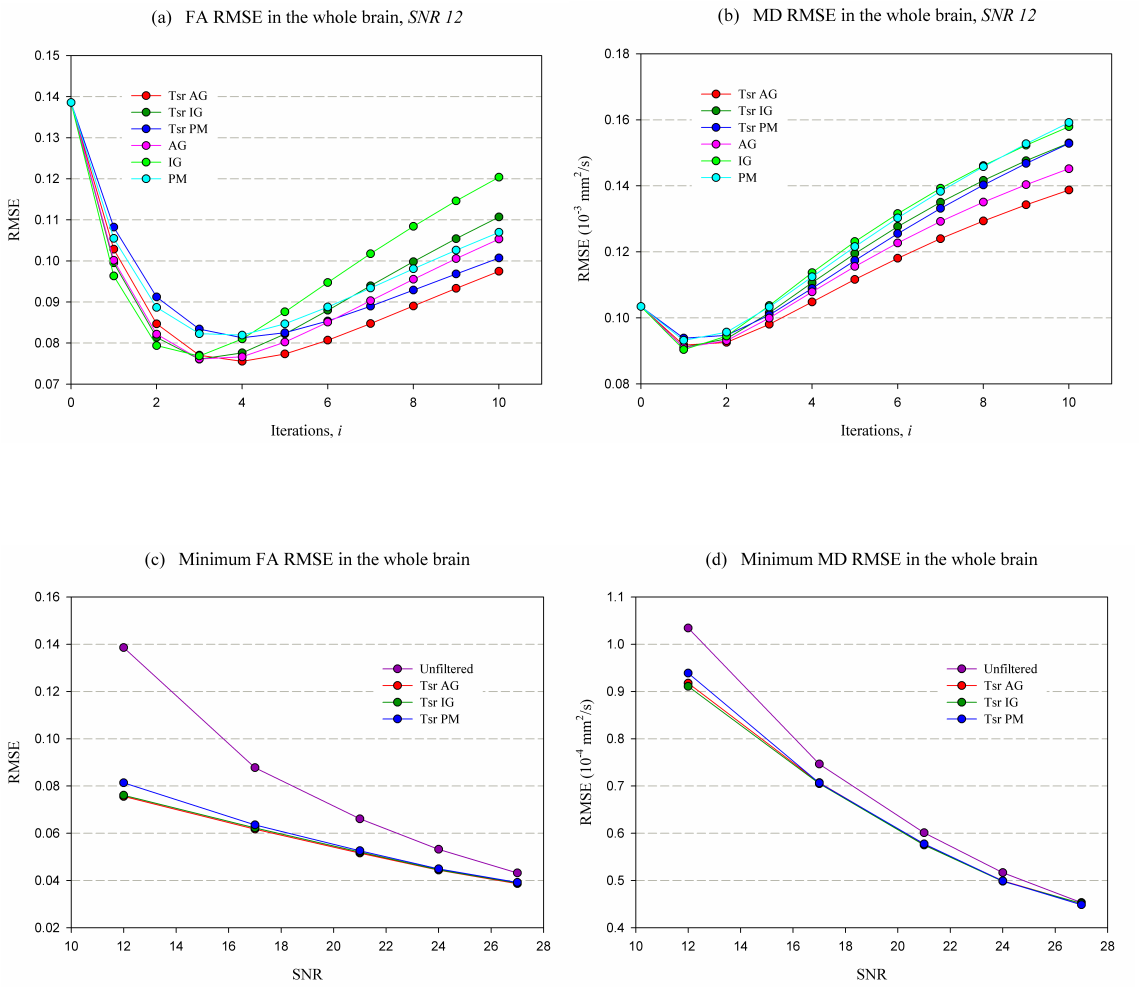

Fig 4-5.The effects of filtering on FA (a), (c) and MD (b), (d) in the whole brain, CSF are excluded in the evaluation. SNR ~12 was shown in these plots. Tsr AG represents the case of filtering of tensor elements with an anisotropic Gaussian filter. Tsr IG represents the case of filtering of tensor elements with an isotropic Gaussian filter. Tsr PM represents the case of filtering of tensor elements with a PM algorithm. AG, IG and PM represent the case of filtering DW data.

(a) FA RMSE in WM , *SNR 12*

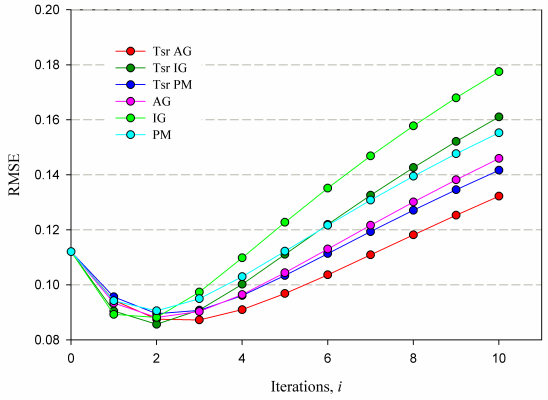

(b) MD RMSE in WM , *SNR 12*

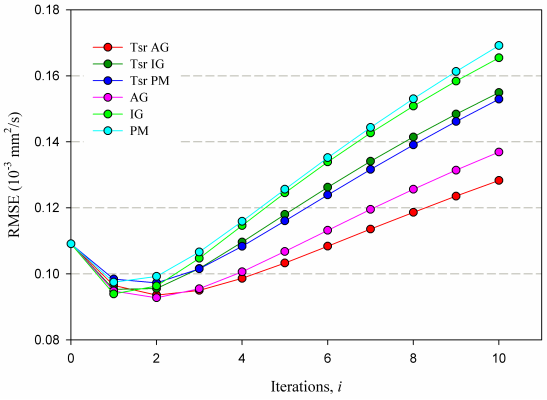

(c) Minimum FA RMSE in WM

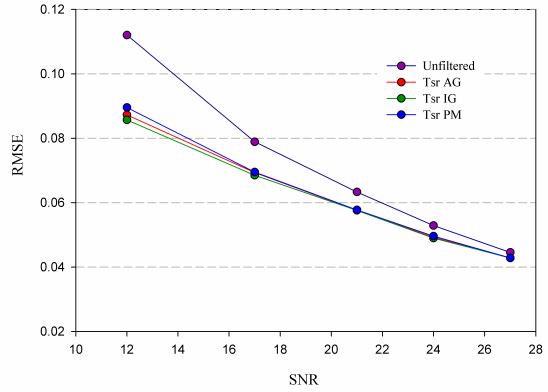

(d) Minimum MD RMSE in WM

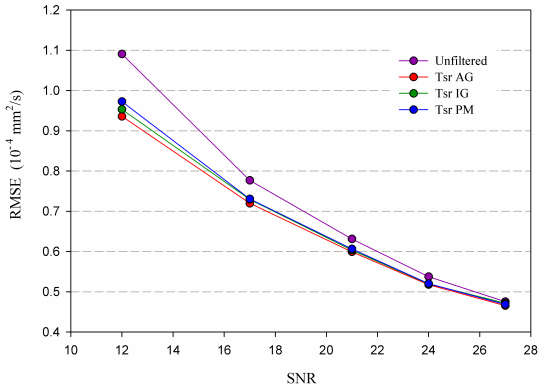

(e) Minimum FA RMSE in CC

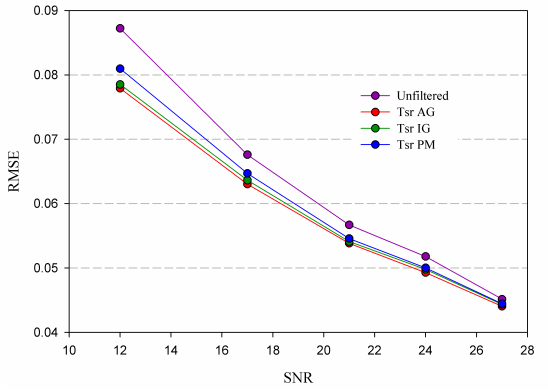

(f) Minimum Princ. Evc Dispersion in WM

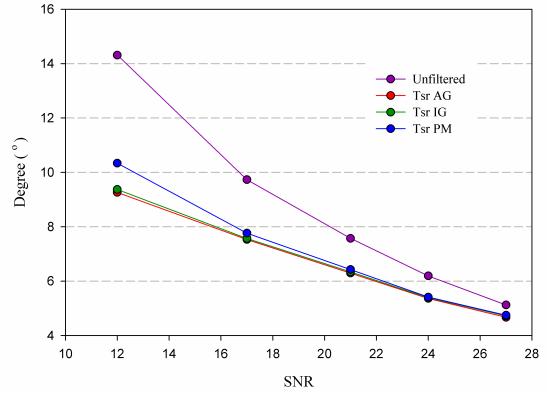

Fig 4-6.The effects of filtering on FA (a), (c) and MD (b) (d) in the total white matter (thresholded FA >0.45). The effects of filtering on FA in the corpus callosum (FA is greater than 0.6) is shown in (e) and (f) demonstrates the angular dispersion of the principal eigenvectors due to the filtering.

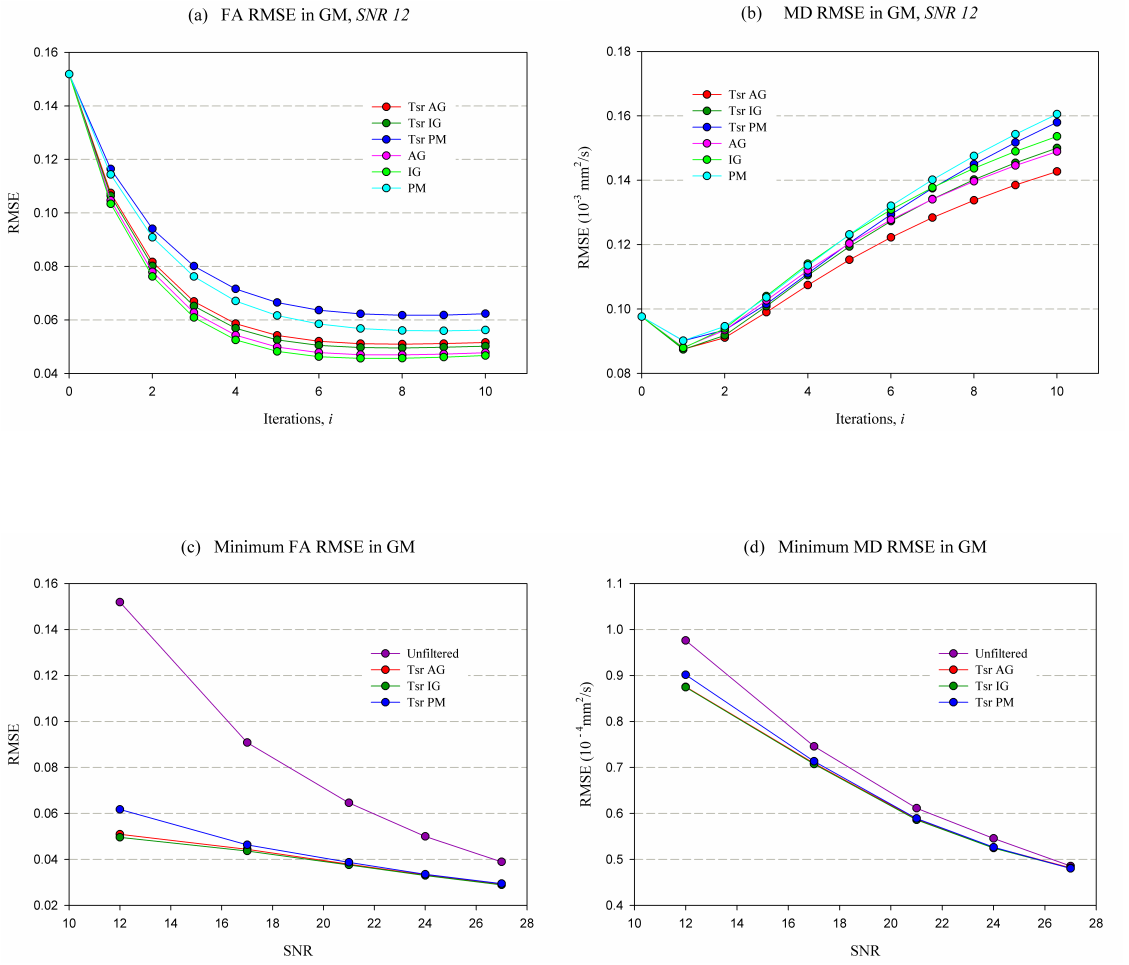

Fig 4-7.The effects of filtering on FA (a), (b) and MD (c) ,(d) in the total grey matter (thresholded FA <0.15, CSF excluded).

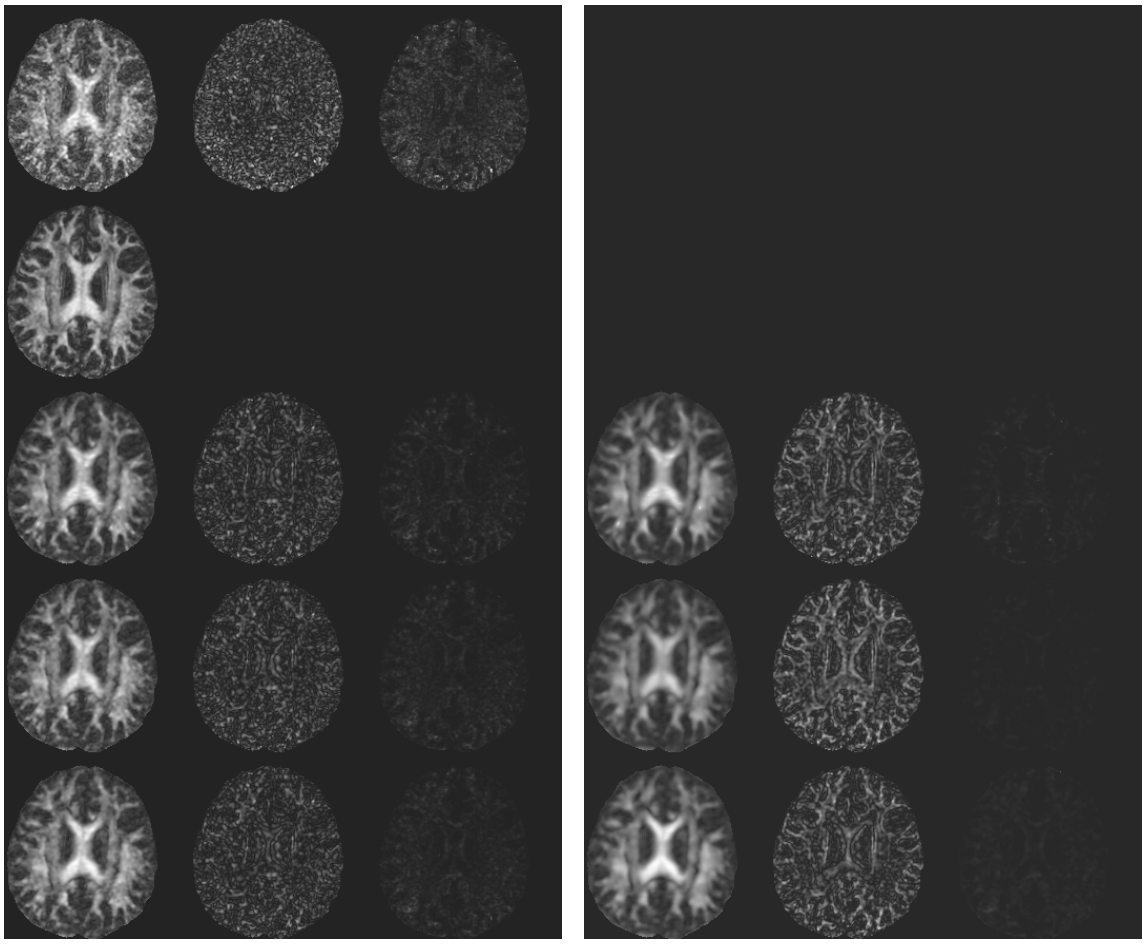

(a) (b)

Fig 4-8-(a). The first row is unfiltered FA, error, and variance map of SNR 12 data. The second row is the gold standard FA. The third row is AG filtered (the 4th iteration), the fourth row is IG filtered (the 3rd iteration), the fifth row is PM filtered (the 4th iteration) FA maps. Each iteration was corresponding to the minimum RMSE in Fig 4-5-(a). Fig 4-8-(b) All filtered images are at the 10th iteration. A significant error lied in the white matter region of IG filtered, (e.g. in the body of corpus callosum) Over-filtering led to almost invisible variance maps are in this figure (Fig 4-8-b 3rd column).

4.4 Results

Real In Vivo DT-MRI Data

Whole Brain. Plots of the estimated RMSE values (4-7) for all filters evaluated for the whole brain (excluding CSF) are shown in Fig 4-5. For all filters, the RMSE initially decreased for both FA and MD (Fig 4-5 a, b, respectively for SNR = 12) and then increased after 3-4 iterations for FA and a single iteration for MD. At the lowest SNR level, the isotropic and anisotropic Gaussian filters were very similar in overall minimum RMSE; however, the error increased much more quickly for the isotropic filter after the minimum RMSE point was passed. The Perona Malik filter did not reduce the RMSE quite as effectively as the Gaussian filters at this level. The minimum RMSE levels for both the original unfiltered data and each of the filters (applied to the tensor data) are plotted as a function of SNR in Fig 4-5-c, and d for FA and MD, respectively. These plots demonstrate that all filters performed comparably, particularly when the SNR was large enough. The relative improvement with filtering was much greater for FA maps than MD. Another interesting observation was that filtering DW data (legends; Ag, IG, PM in Fig 4-5-a, b) was more effective until the RMSE reached each minimum RMSE and after each minimum RMSE point, filtering tensor elements (legends; Tsr Ag, Tsr IG, Tsr PM in Fig 4-5-a, b) increased errors more slowly from over-filtering.

White Matter. Summary plots of RMSE filter performance in regions of generally homogenous white matter (FA > 0.45) are shown in Fig. 4-6. In general, the behavior is similar to that observed over the entire brain. The optimum number of iterations was roughly 2-3 for FA (slightly lower than for the whole brain) and 1-2 for MD. In a region

of corpus callosum [Fig 4-6 e], the optimum number of iterations increased and the anisotropic Gaussian filter performed slightly better. The error in the major eigenvector angle in white matter was greatly decreased with filtering with slightly better performance with the Gaussian filters at the lowest SNR level [Fig 4-6 f].

Grey Matter. Summary plots of RMSE filter performance in regions of moderately isotropic 'grey' matter (FA < 0.15) are shown in Fig. 4-7. In general, the behavior of filtering on the MD maps (Fig. 4-7 b, d – optimum 1 iteration) is similar to that observed over the entire brain. However, the filters took much longer to converge (6-9 iterations) when minimizing the RMSE of FA (Fig 4-7 a). Relatively large decreases in FA error were observed with all filters, particularly with filtering DW data [Fig 4-7c], particularly for lower SNR data, whereas the decreases in MD error where much smaller [Fig 4-7 d].

Brain Images. Filter performance is compared visually in Fig 4-8. The unfiltered FA map appears grainy relative to the gold standard with positive biases in regions of gray matter. In all cases, the total-brain, optimum filtered image data appears much less grainy with reduced biases in grey matter regions. However, the fine white matter detail near the brain periphery is not as sharp as in the gold standard case. The mean error and standard deviation maps demonstrate that these measures as well as the FA RSME in Fig 2 are clearly reduced for all filters. To investigate the effects of over-filtering on the image data, the FA maps are shown after 10 filter iterations. It is clear that the isotropic Gaussian filter causes more blurring than either the anisotropic Gaussian or Perona Malik filters.

Simulated Images. The RMSE performance of the filters on the noisy synthetic data is plotted in Fig. 4-10. Overall, the performances of the filters on images with

synthetic noise are similar to the results observed in real image data (Fig 4-5). The effects of the step size for the Perona Malik filter are shown in Fig 4-10 a. For t = 0.5 or less, the optimum filter performances (minimum RMSE condition) are similar, although smaller step sizes result in less variability with number of iterations, which may be preferable for cases where the optimum number of iterations are not well defined.

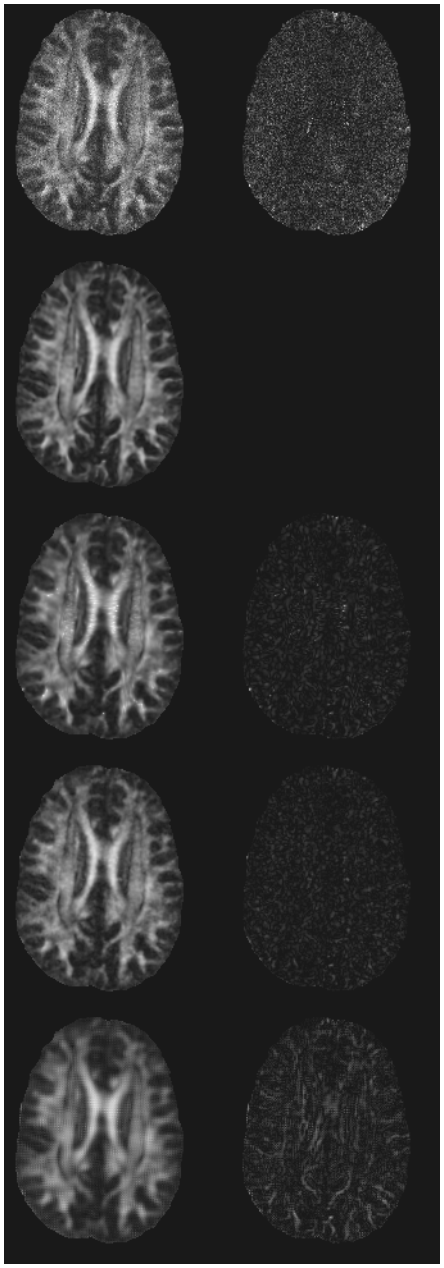

Fig 4-9. *Simulation data* The first row is unfiltered FA, error, and variance map of SNR 15 synthetic data. The second row is the gold standard FA. The third row is AG filtered (the 7^{th} iteration), the fourth row is IG filtered (the 5^{th} iteration), the fifth row is PM filtered (the 8^{th} iteration) FA maps. Each iteration was corresponding to the minimum RMSE in Fig 4-5-(a).

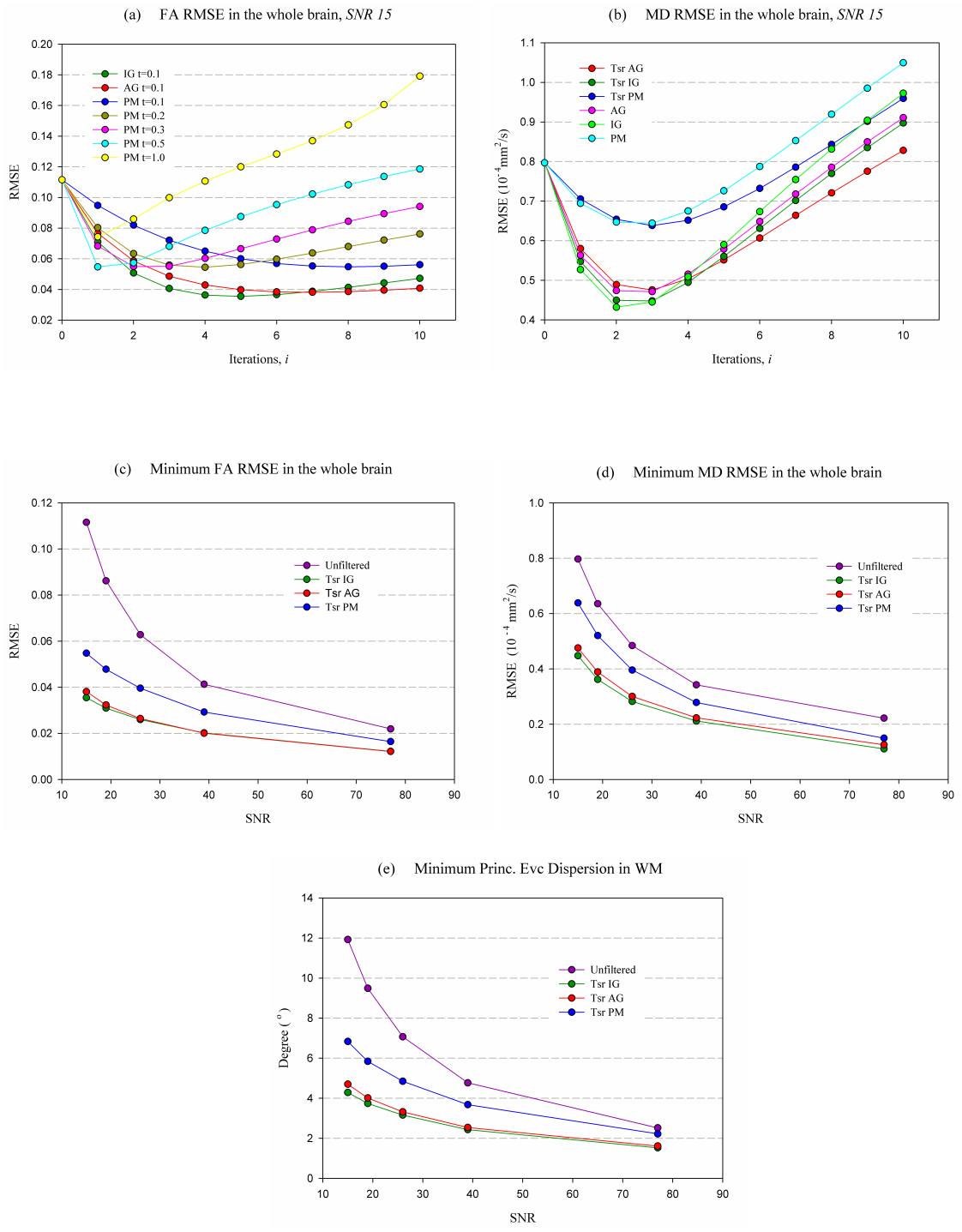

Fig 4-10. The effects of filtering on FA (a), (c) and MD (b), (d) in the whole brain region with synthetic noise added.

4.5 Discussion

In this study, a comparison of different DT-MRI filtering methods was performed. In general all filtering approaches resulted in similar levels of error reduction in real DT-MRI data when applied optimally; however, the Gaussian kernel filters (isotropic and anisotropic) performed better than the Perona Malik filter for the synthetic noise data set. Filtering, when applied optimally, does appear to reduce the root mean squared error (RMSE) of all the investigated measures – FA, MD and the major eigenvector direction. For DT-MRI data with the lowest SNR (~12), filtering reduces the RMSE of the FA by 44%, 24%, and 67% over unfiltered data in whole brain, WM and GM. For MD, the relative reductions in RMSE were much less ~ 11-12% for all tissue regions. The angular error in the major eigenvector was reduced by roughly 33% in WM. For all measures and tissue types, the relative and absolute improvements in RMSE decreased with increasing SNR. Also, the number of iterations required to optimize the RMSE decreased with increasing SNR (data not shown).

Although the optimum performance was similar for all filters in the real data, it was evident that the isotropic Gaussian kernel filter was more sensitive to over-filtering. This is because the anisotropic filters (both anisotropic Gaussian and Perona Malik) performed preferential smoothing parallel to the white matter tracts, which minimizes the partial volume averaging between grey matter and white matter. Since the optimum amount of filtering is generally not known in advance, anisotropic filtering strategies appear to be preferable to avoid excessive blurring.

Another observation is that the optimum number of iterations was dependent upon both the tissue and the specific measure. For example, the optimum number of iterations

for minimizing RMSE of FA was generally lower in WM than in GM. This would imply that the optimum filtering depends upon the specific tissue type and even the region of interest. Consequently, it would be advisable to do less filtering if one is interested in regions of white matter FA; however, if the study focuses on gray matter regions like the basal ganglia, more filtering will help to reduce the amount of error in the measurement. In regions of white matter, the anisotropic Gaussian filters were less prone to errors from over-filtering. Another example is the optimum number of iterations for minimizing the RMSE of MD is much smaller than minimizing the RMSE of FA. This would imply that as long as the analyses of FA and MD were separate, different amounts of filtering may be used to optimize the errors in different maps.

The RMSE measure is a nonspecific indicator of error in that it may reflect either systematic differences (e.g., mean difference) or signal variance (e.g., noise). In general, the signal variance decreases with the higher amounts of filtering. However, the systematic or mean differences often initially decrease a little, and then increase as the image data is blurred, which ultimately drives the RMSE upward. Decreases in the systematic error of FA often decrease much more in regions of grey matter because this measure is biased in regions with isotropic diffusion at low SNR (data not shown – see [Pierpaoli and Basser, 1996]). It should be noted that filtering will not remove all the noise and will introduce blurring, which ultimately reduces the spatial resolution of the image data. Consequently, there is a balance of tradeoffs between the spatial resolution that can be achieved and the biases and noise associated with smaller voxels. Anisotropic filtering appears to improve the noise problems, although it is not clear whether this is preferable over acquiring the images with slightly lower spatial resolution. Future studies

are necessary to evaluate this tradeoff.

4.6 Conclusions

In this study, the performance of three spatial filtering methods for reducing the errors of different DT-MRI measures – FA, MD and major eigenvector orientation was compared. Overall, the study demonstrated that for noisy image data, optimum filtering reduced the errors for all measures. The optimum performances of both the isotropic and anisotropic Gaussian filters were similar, yet the anisotropic filter was much less prone to over-filtering.

CHAPTER 5

APPLICATIONS OF ANISOTROPIC GAUSSIAN SMOOTHING: VOXEL BASED ANALYSIS OF DT-MRI

5.1 Introduction

DT-MRI of the human brain is increasingly being employed to investigate the organization and microstructure of white matter tracts in the brain for a broad range of applications including ischemia, neurodevelopment, aging, Alzheimer's disease and behavioral neurology [Erikkson et al., 2001; Moseley, 2002; Neil et al., 2002; Sotak, 2002; Barnea-Goraly et al., 2003; Burns et al., 2003; Jones et al., 2005; Filley 2005]. In many of these studies, the DT-MRI properties are compared between two groups (i.e., disease versus control). If specific regions of the brain are hypothesized to be different or affected, regional segmentation tools are used to define regions of interest. However, when regions are not well-defined a priori, voxel based analysis methods are often used. In this method, images from multiple subjects are co-registered using linear (i.e., affine) or nonlinear warping transformations. Images are spatially blurred typically with an isotropic Gaussian kernel to compensate for anatomical misregistration, and improve the statistical properties (e.g., Gaussian random fields [Worsley et al., 1992]. Statistical

testing is performed at each voxel location. A significant problem with voxel-based analysis of DT-MRI data is that spatial blurring causes the images to lose their anatomic specificity. For example, standard Gaussian blurring will mix signals from WM, GM, CSF, and other tissues.

In this chapter, the anisotropic Gaussian kernel smoothing that was explored in the previous chapter is applied to the DT-MRI group analysis specifically of the white matter in individuals with autism as compared to controls. Anisotropic blurring is believed to reduce partial volume effects and therefore may be preferable to the conventional isotropic smoothing. In this study anisotropic and isotropic blurring were compared. The results obtained using voxel-based methods in the corpus callosum were compared with those from an ROI analysis from the same data [Alexander et al., in press].

5.2 Methods

DT-MRI data preparation

DT-MRI data from seventy seven subjects were used in this study. Forty three subjects belonged to the autism-spectrum group and thirty four subjects matched for age, handedness, IQ, and head size of the autism data sets. More details about subject and related assessment may be found in the paper [Alexander et al., in press].

Eddy currents and field inhomogeneiy related distortions of each data set were corrected using a 2D affine automatic image registration program (AIR) and in-house software for a field map correction method that is described in the paper [Jezzard et al, 1995]. Distortion corrected DW images were interpolated into 2 x 2 x 2 mm^3 voxels and six tensor elements were calculated using a multivariate log- linear regression method

[Basser et al, 1994]. Then the tensor was diagonalized to estimate three eigenvectors and eigenvalues. Maps of DT-MRI measures, FA and MD were calculated for individual subjects [Basser and Pierpaoli, 1996].

White matter segmentation

General white matter was extracted using FAST [Zhang et al., 2001] in the FMRIB software library (http://www.fmrib.ox.ac.uk/fsl/). FAST was developed using a model of hidden Markov random fields, and expectation-maximization theory. More details on this program can be found in the paper [Zhang et al., 2001]. Two channels (the major and minor eigenvalues of the diffusion tensor) were used as inputs to generate three classes of tissues: grey matter, white matter, and CSF.

In addition to white matter segmentation using FAST, voxels in the white matter segmented regions with relatively high MD values were removed (Fig 5-2) by thresholding the MD maps to remove voxels that were greater than four standard deviations above the mean.

Defining ROI on CC

ROI analysis was done on the corpus callosum prior to performing the voxel-based analysis. First, the corpus callosum was contoured on a map of x component of major eigenvector multiplied by FA. This map ($\vec{e}_{1,X} * FA$) has better contrast on the voxels that have higher FA and larger eigenvector components of right to left major eigenvector directions. The extraction of the corpus callosum on the maps of ($\vec{e}_{1,X} * FA$) was done for all seventy-seven subjects by hand.

More specific regions on the corpus callosum were obtained [Fig 5-4]. Each sub region was composed of a cubical 9 x 9 x 9 voxels, and also thresholded for ($\vec{e}_{1,X} * FA$ to be greater than 0.4.

Statistical analysis

A one-way analysis of variance (ANOVA) is a way to test the equality of three or more means at one time by using variances. Using ANOVA, group differences on the DT-MRI measurements, specifically, FA, MD, and eigenvalues, in three separate sub regions (genu, splenium, and body) and global corpus callosum were tested.

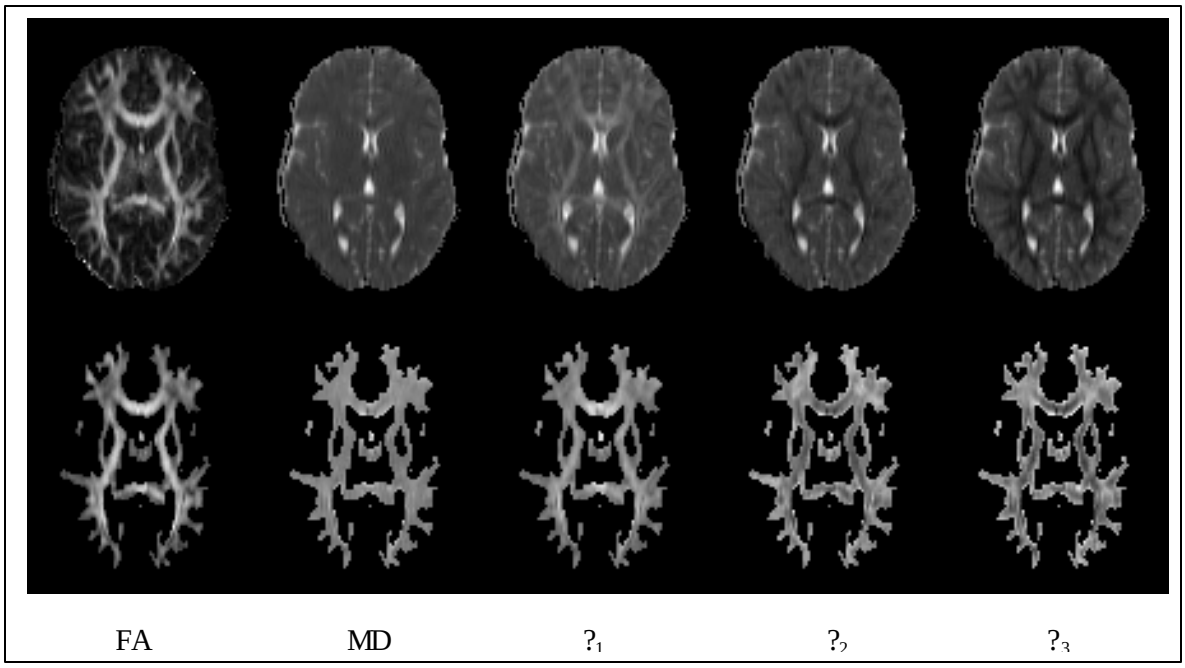

Fig 5-1 Examples of the white matter segmentation. The top row images are the original FA, MD, $?_1$, $?_2$, and $?_3$ maps of one of the subjects, and the bottom row images are white matter segmented FA, MD, $?_1$, $?_2$, and $?_3$ maps using FAST.

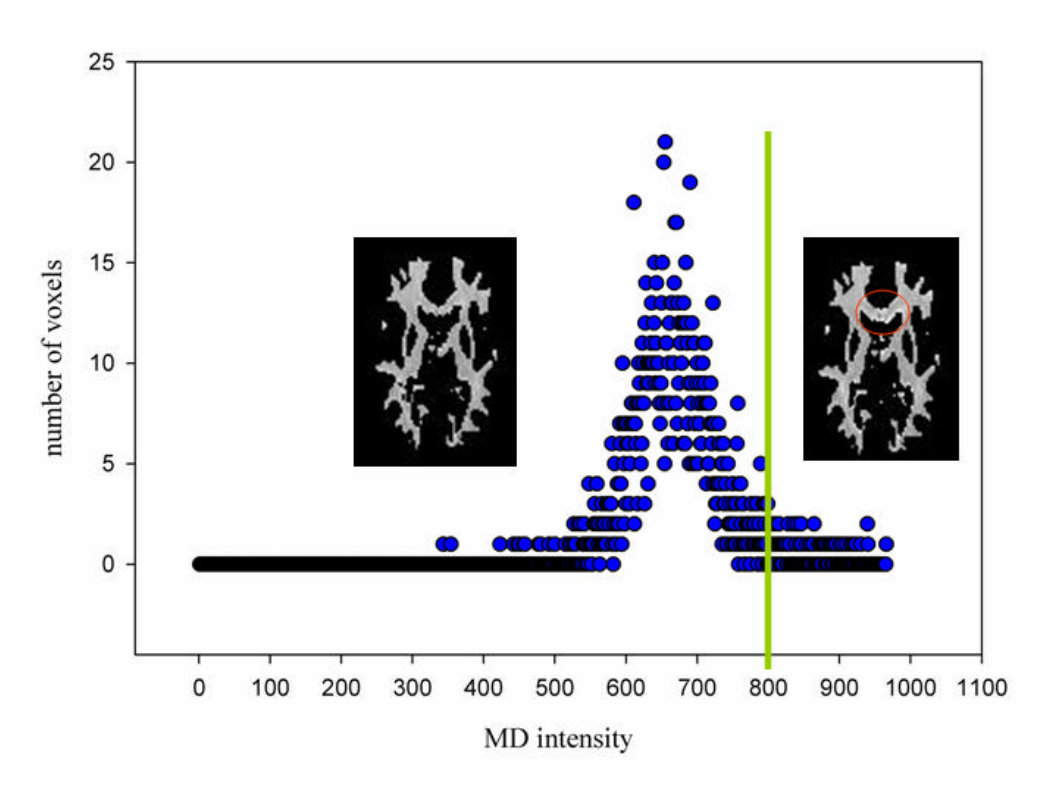

Fig 5-2 white matter segmentation – additional removal of voxels using MD histogram. Relatively high MD values are highly likely due to the partial volume effects affected by surrounded CSF. These voxels (the right image in the plot box, shaded in hyper intensity, see the borderlines that are within the red circle) were successfully removed using a threshold set by using a histogram of MD. The right tail that was thresholded at the four times of standard deviation of MD. The image on the left side of the green bar that indicates the four times of standard deviation was produced after masking out the voxels with hyper intensities.

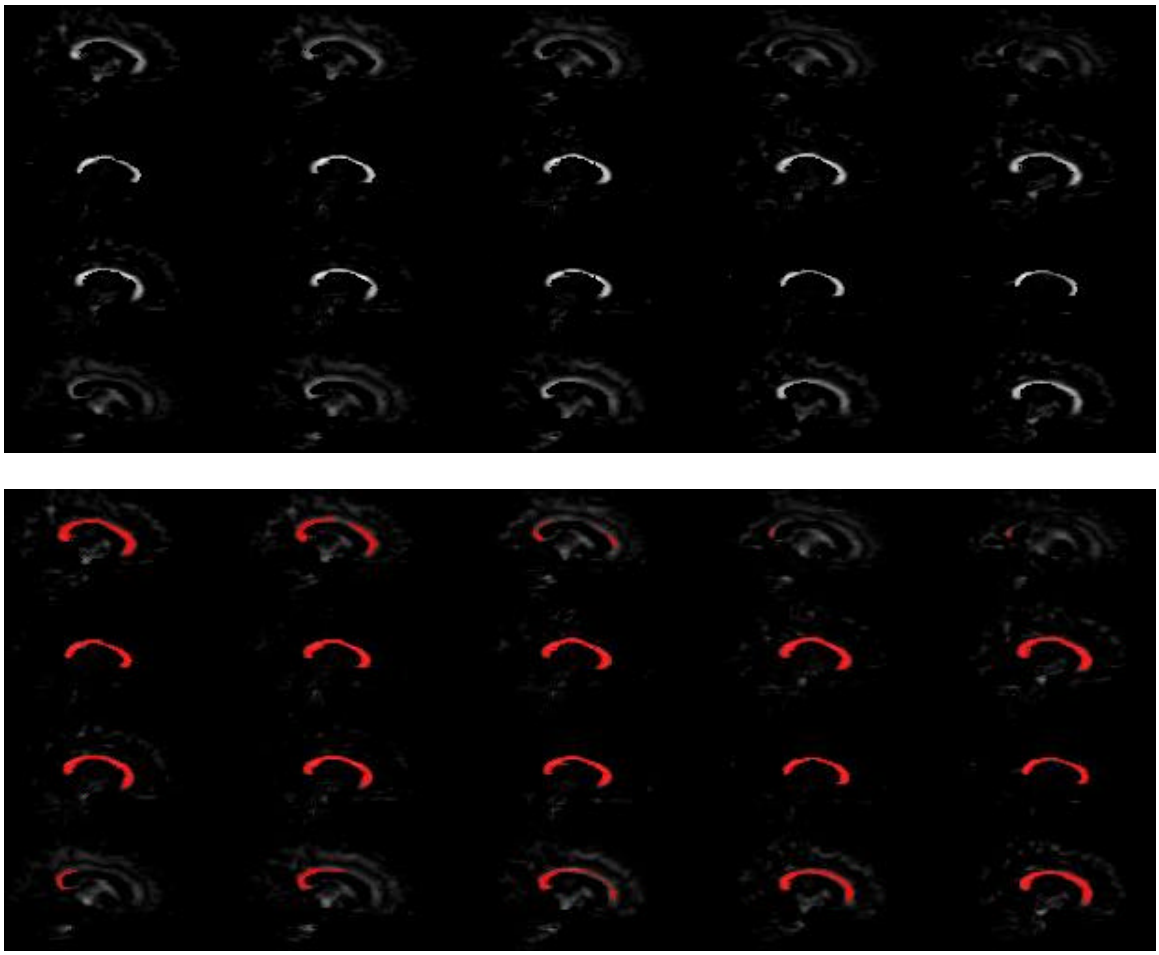

Fig 5-3 The corpus callosum segmentation. The top row is a map of ($\vec{e}_{1,X} * FA$: white matter segmented and thresholded shown as in Fig 5-2). High contrast for the corpus callosum is shown in the top row images. The CC was then manually extracted under a condition of $\vec{e}_{1,X} * FA$ >0.2, and the extracted CC is shown in the bottom row in red shade.

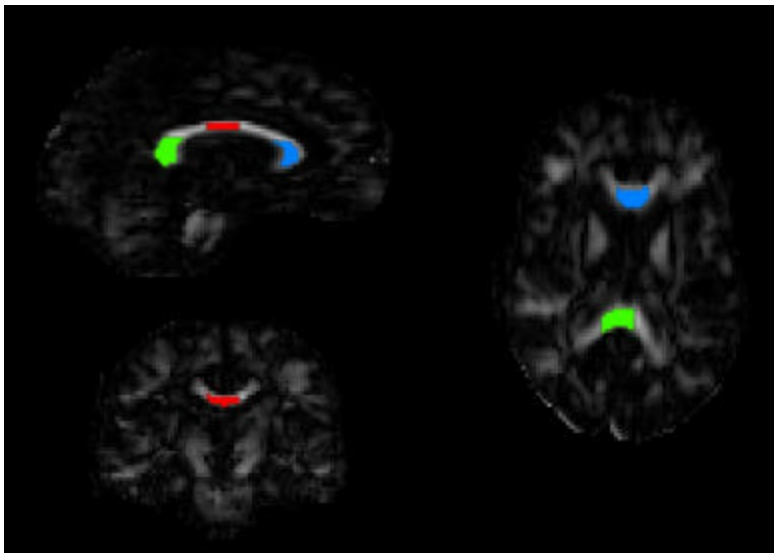

Fig 5-4 The regional corpus callosum segmentation. The underlying image is a map of $\vec{e}_{1,X} * FA$ of one subject. Genu is shown in blue, body in red, and splenium in green.

Voxel-based DT-MRI analysis

Each of the six elements of the diffusion tensor data for subjects were transformed with the same transformation matrix by which FA maps were transformed to be coregistered with the reference data. The reference data was one of seventy seven subjects.

In order to construct the subject-based anisotropic Gaussian kernels, the transformed diffusion tensor was reoriented using the preservation of principal directions that were previously described [Alexander et al, 2001]. The reorientation was conducted for the major eigen vector directions to be reoriented using the affine matrix that was used for the transformation of FA, MD, eigenvalue maps and all tensor elements, then the medium eigenvector directions that were also transformed through the same affine matrix

were projected to the plane that is to be normal to the reoriented major eigenvectors. This projection is necessary because the affine transformed medium eigenvector may not be perpendicular to the transformed major eigenvector. Once the major and medium eigenvector directions were determined, the minor eigenvectors can only exist to be orthogonal to both major and medium eigenvectors. Using the transformed eigenvectors and same eigenvalues, transformed tensor was obtained in a voxel basis.

Smoothing kernels of the size 5 x 5 x 5 voxels were used to create the full width half maximum (FWHM) 12 mm anisotropic Gaussian kernel. Using a t in Eqn. (4-6) a value of 5.0 (s/mm^2) required iterating six times to achieve a smoothing level that corresponded to filter size 12 mm isotropic Gaussian smoothing. Unlike the isotropic Gaussian kernel, anisotropic Gaussian kernel does not have a definitive FWHM since the three principal directions have three different FWHM in the three dimensional space. The total diffusion time t and iteration numbers were obtained as follows:

1. s in $K(\vec{r}) = \frac{\exp(-\vec{r}'\vec{r} / 2s^2)}{(2p)^{3/2} s^3}$ (the isotropic Gaussian in the three dimensional space), is determined with a given FWHM, $s = FWHM / \sqrt{(8\log(2)}$
2. The total diffusion time t is defined in the isotropic system as $t = s^2 / 2$
3. Iteration number $(t / \Delta t)^2$ based on the property of $K_{\sqrt{nt}} = K_t \otimes K_t \otimes K_t ... \otimes K_t$ (n times), where Δt is a dummy variable (local diffusion time per iteration)

   Example: Δt =5.0 iteration number, 6.

In addition, isotropic Gaussian smoothing with a 12 mm FWHM was also performed. Once the individual data were smoothed, a two-tailed contrast t test was

performed on maps of FA, MD, and eigenvalues of the two groups. Significance levels for *t* statistics were set at P<0.005. The resulting *t* statistic images were thresholded using the minimum given by a Bonferroni correction and random field theory [Worsley et al., 1992]. Cluster inference was performed using a software package *FMRISTAT*. (http://www.math.mcgill.ca/keith/fmristat/). The threshold for cluster extent was set at P<0.05.

5.3 Results

ROI analysis

The segmented corpus callosum analysis was summarized in the Table 5-1. The axial and radial diffusitivities correspond to $D_a = l_1$, and $D_r = \frac{l_2 + l_3}{2}$, respectively.

The autism group had higher MD, radial eigenvalues, and lower values in FA in the corpus callosum. Regionally, the body of corpus callosum was not significantly different between the two groups. More detailed results are reported in [Alexander et al., in press]

Global analysis

A. Smoothing: After affine normalization was done for each subject to co-register with the template, anisotropic Gaussian smoothing on the segmented FA, MD, ?$_1$, ?$_2$, and ?$_3$, maps looked less blurred than the isotropic Gaussian smoothing cases. Fig 5-5 shows white matter segmented, normalized (co-registered to the template) FA map (a) of one subject, FWHM 12 mm isotropic Gaussian blurred map (b), and FWHM 12 mm anisotropic Gaussian blurred map (c). As suggested by the images, anisotropic Gaussian

smoothing preserved the more peripheral white matter structures. In addition, the overall intensities were less reduced with anisotropic smoothing.

Fig 5-6 shows the histogram of the data from Fig 5-5. As indicated in the Fig 5-6-c anisotropic Gaussian smoothing better preserved the characteristics of the original distributions of FA maps. Even with a 4 mm FWHM, the isotropic smoothing caused the bump in the FA histogram to be eliminated.

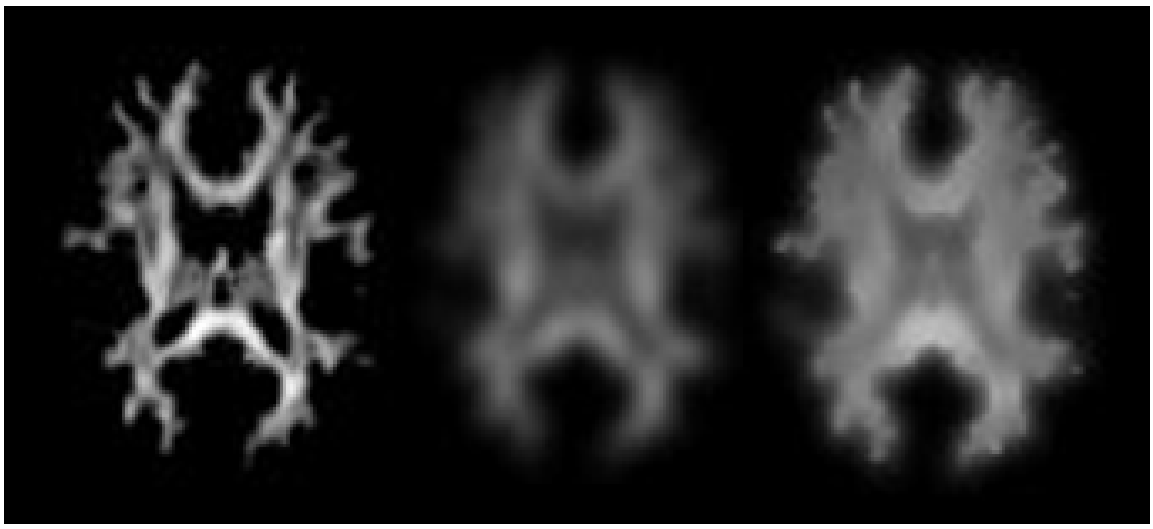

(a) 0.306 (b) 0.124 (c) 0.154

Fig 5-5 Isotropic kernel smoothing with FWHM 12 mm. vs. anisotropic Gaussian kernel smoothing 12 mm. All images displayed in the same scale. (a) is a white matter segmented normalized FA map of one subject. (b) is isotropic smoothing with FWHM 12 mm. (c) is anisotropic smoothing with FWHM 12 mm. The bottom row is the coronal view. Peripheral structures are preserved better with anisotropic Gaussian kernel smoothing. The numbers below each image are the overall averaged intensity values of FA.

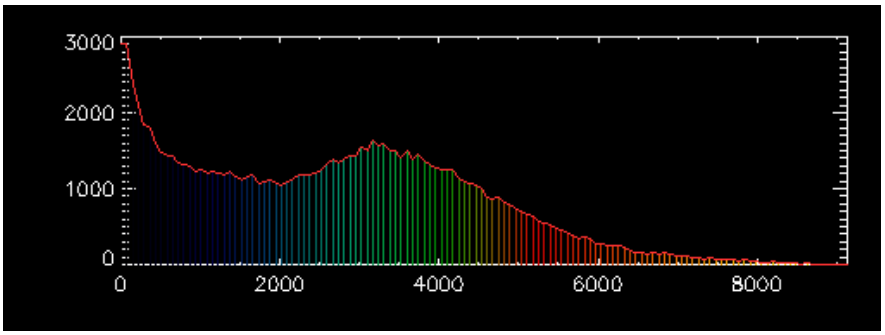

(a) histogram of normalized FA, intensities ($x10^{-3}$)

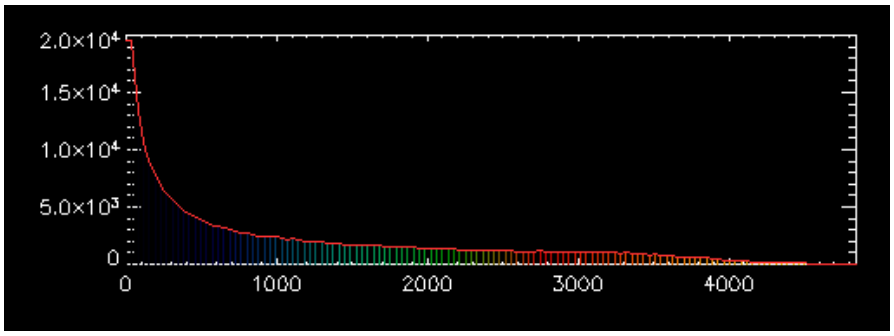

(b) histogram of normalized, isotropically smoothed FA, intensities ($x10^{-3}$)

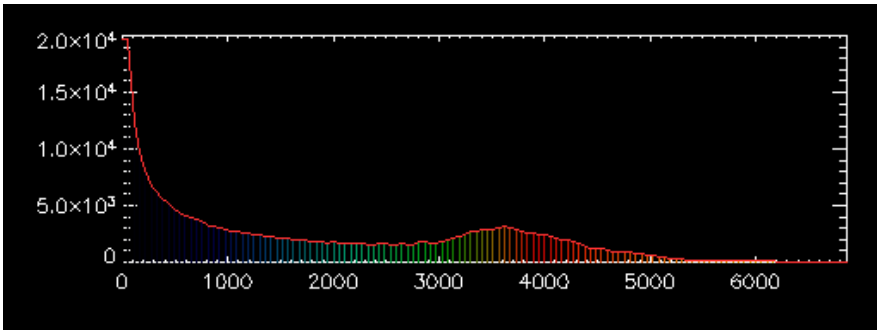

(c) histogram of normalized anisotropically smoothed FA, intensities ($x10^{-3}$)

Fig 5-6 a 12 mm FWHM isotropic kernel smoothing. vs. a 12 mm FWHM anisotropic Gaussian kernel smoothing. Histogram of Fig 5-5 data. Profiles of anisotropic smoothing is more representative for the raw histogram (a).

Table 5-1. Group Comparison of Anisotropy and Diffusivities in the Corpus Callosum Determined by One-way ANOVA

	Autism (n=43)		**Control (n=34)**		**Group Comparison**	
	Mean	SD	Mean	SD	F	Significance
Fractional Anisotropy						
Genu	.663	.042	.692	.037	10.01	.002**
Body	.664	.045	.683	.038	3.71	.058
Splenium	.693	.045	.720	.032	8.22	.005**
Total Corpus Callosum	.552	.037	.579	.024	13.45	<.001***
Mean Diffusivity (10^{-3} mm^2/s)						
Genu	.842	.048	.820	.034	5.13	.026*
Body	.869	.041	.840	.041	13.69	<.001***
Splenium	.832	.050	.818	.026	2.21	.141
Total Corpus Callosum	.833	.037	.807	.023	13.01	.001**
Axial Diffusivity (10^{-3} mm^2/s)						
Genu	1.61	.074	1.62	.067	.33	.569
Body	1.67	.077	1.65	.067	1.74	.191
Splenium	1.64	.091	1.67	.071	1.30	.257
Total Corpus Callosum	1.43	.054	1.43	.043	.11	.747
Radial Diffusivity (10^{-3} mm^2/s)						
Genu	.457	.057	.420	.043	10.51	.002**
Body	.466	.057	.434	.039	8.12	.006**
Splenium	.426	.060	.394	.036	7.57	.007**
Total Corpus Callosum	.533	.045	.495	.027	18.01	<.001***

***significant at the .001 level; **significant at the .01 level; *significant at the .05 level
ANOVA = analysis of variance

Table 5-1 is from Alexander et al., in press.

B. FA Measurements: The most of corpus callosum including the body, splenium and genu were shown as significantly different between two groups with the contrast of FA- reduced in autism using a 12 mm FWHM isotropic smoothing [Fig 5-7 a]. With the anisotropic smoothing, the location of clusters was slightly different. Most noticeably no significant differences were revealed in the body of the corpus callosum (squared in red), which is in agreement with the results obtained using the ROI based analyses.

C. MD Measurements: Unlike the ROI analysis, no significant differences in mean diffusitivity between the control and autism groups were found with a 12 mm isotropic Gaussian kernel smoothing. The high T score (0-3.773) in the color bar (Fig 5-9) did appear on the slices that did not cover the corpus callosum. As opposed to isotropic filter, anisotropic smoothing showed significant clusters in the genu at the midline level, and global corpus callosum on the lateral side.

D. Minor eigenvalue measurements: The voxel-based analysis was done on l_1 and l_2 maps, however, t maps of those two parameters did not show any significant values. On the other hand, significant differences in the minor eigenvalue l_3 between the control and autism groups were observed from both isotropic and anisotropic smoothing. Fig (5-) shows bigger significant clusters and higher T score was achieved by anisotropic smoothing. In the ROI analysis the radial eigenvalues $(l_2 + l_3)/2$ were analyzed and the actual difference assumed to be from mainly minor eigenvalue l_3.

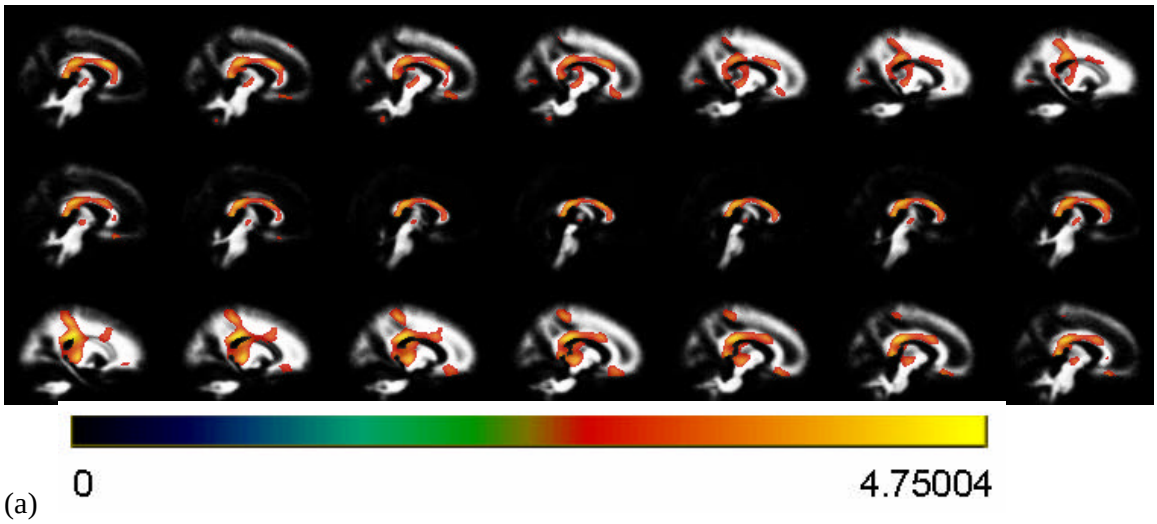

(a)

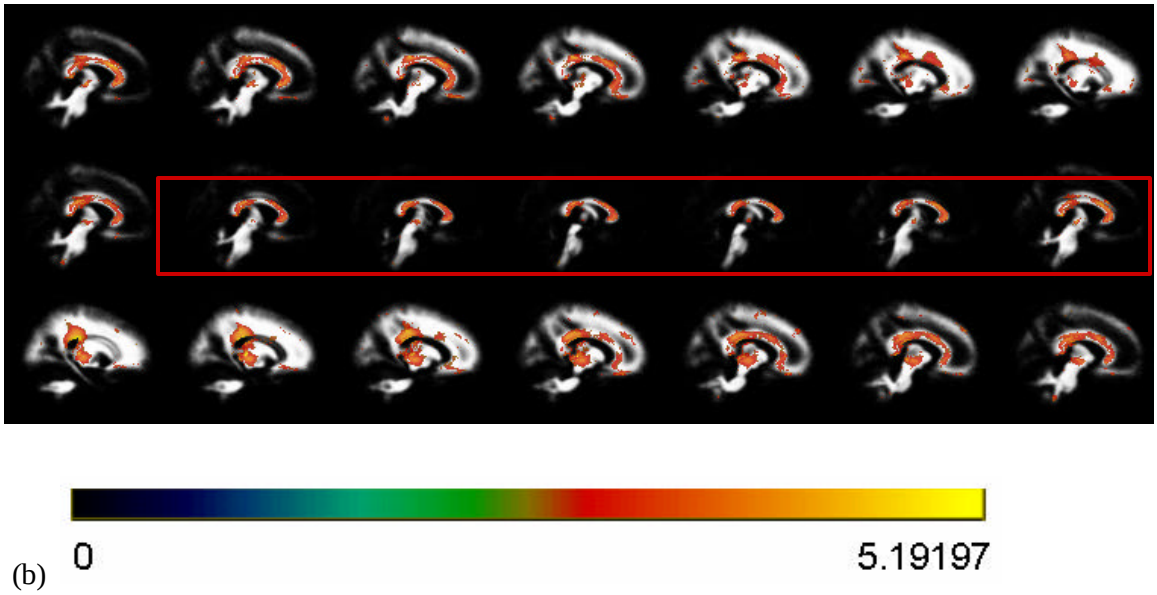

(b)

Fig 5-7 *t*-maps of FA masked from a 12 mm FWHM isotropic Gaussian kernel smoothing (a) and with a 12 mm FWHM anisotropic kernel smoothing (b). The color bar represents the T score. Uncorrected p value was given 0.005. Cluster inference was done for a p value of 0.05

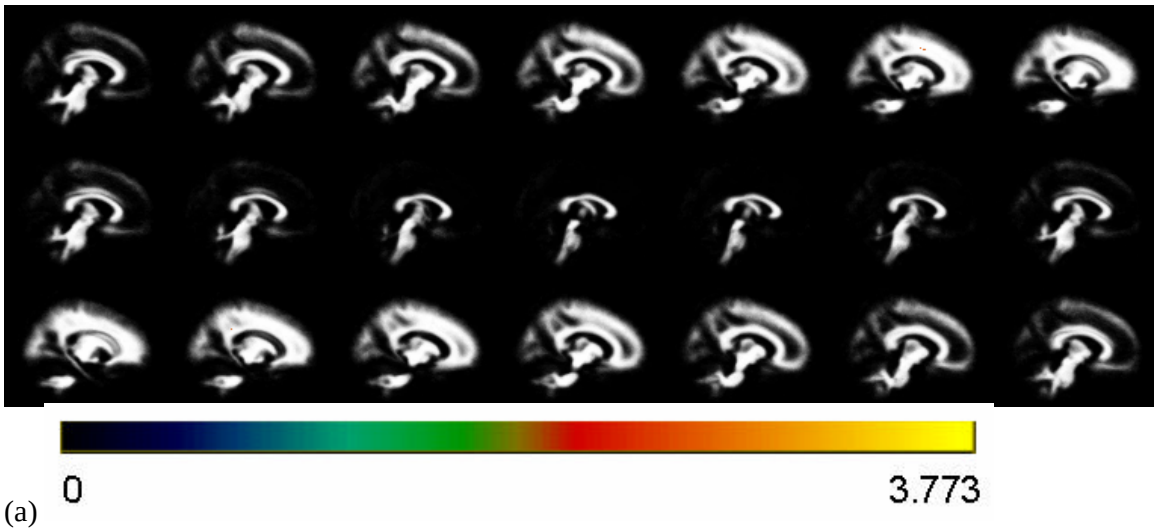

(a)

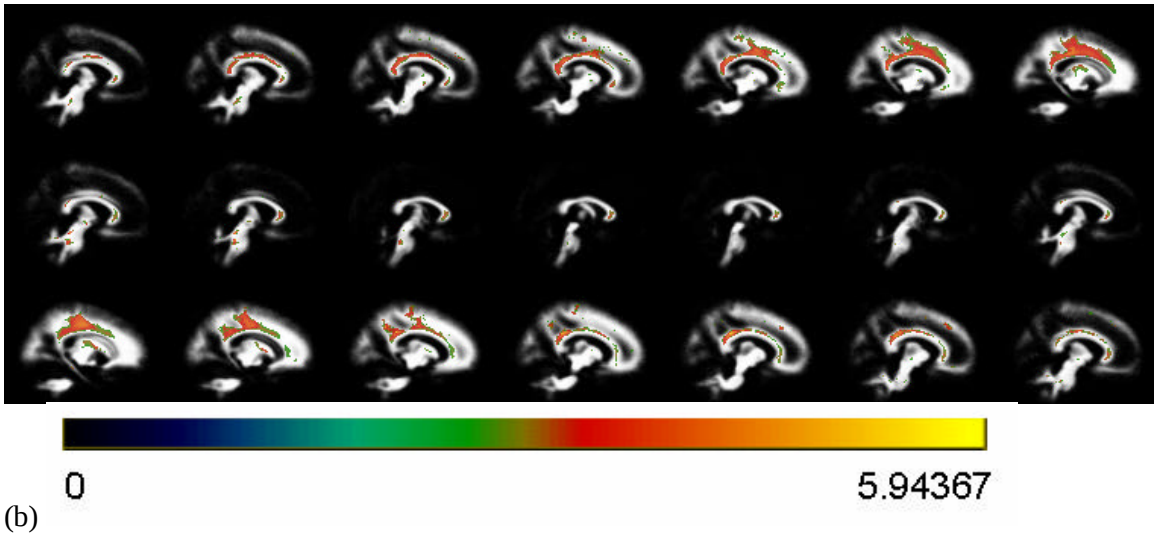

(b)

Fig 5-8 *t*-maps of MD from a 12 mm FWHM isotropic Gaussian kernel smoothing (a) and with a 12 mm FWHM anisotropic kernel smoothing (b). The color bar represents the T score. Uncorrected p value was given 0.005. Cluster inference was done for a p value of 0.05

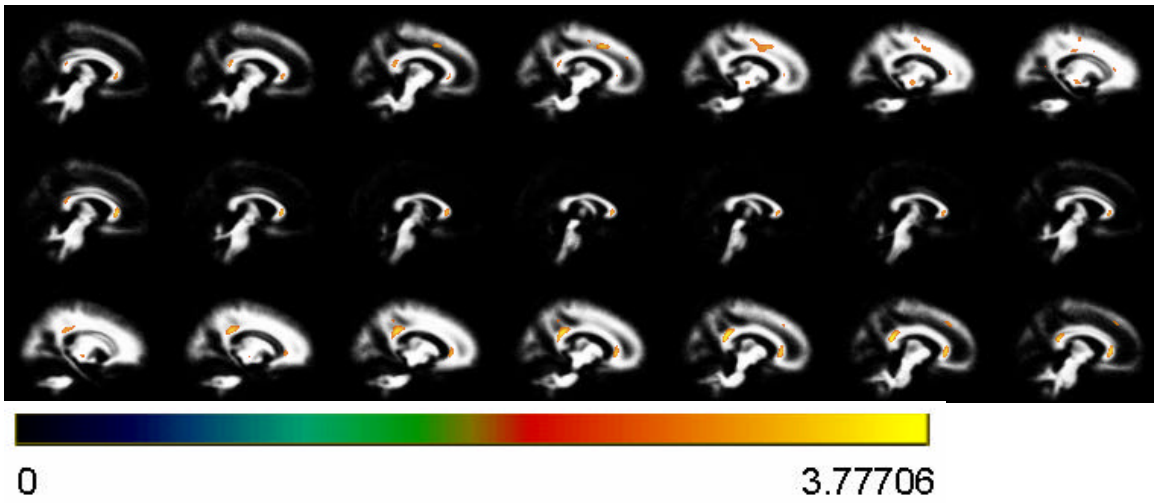

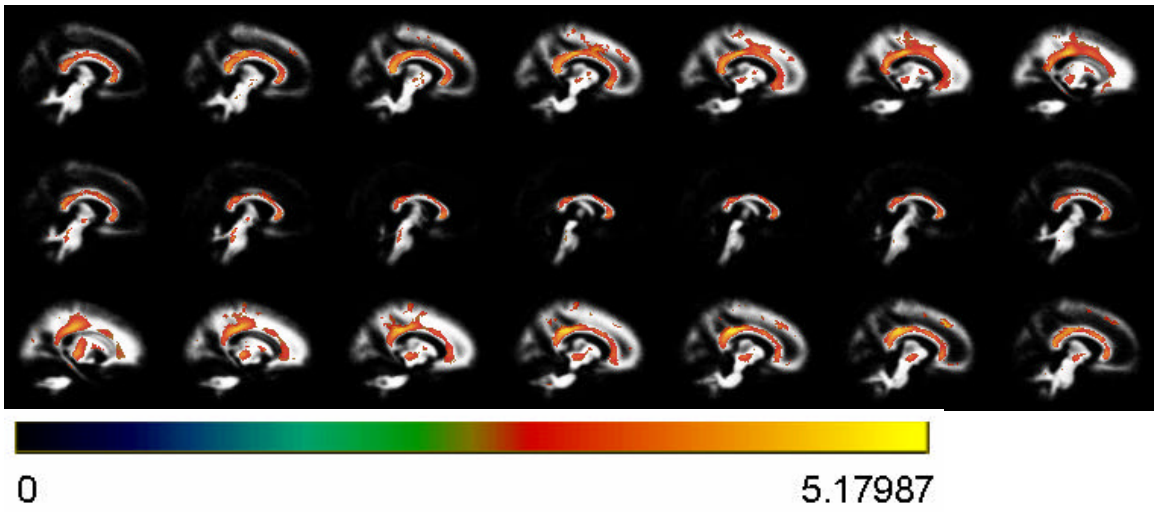

Fig 5-9 *t*-maps of l_3 from a 12 mm FWHM isotropic Gaussian kernel smoothing (a) and with a 12 mm FWHM anisotropic kernel smoothing (b). The color bar represents the T score. Uncorrected p value was given 0.005. Cluster inference was done in p value 0.05

5.4 Discussion

The voxel-based analysis with anisotropic Gaussian smoothing was more consistent with the manual segmentation results in the corpus callosum than conventional isotropic Gaussian smoothing. The difference between isotropic and anisotropic filter lies in the fact that the conventional isotropic Gaussian smoothing increases the partial volume signal averaging, which is reduced with anisotropic kernel smoothing. More thorough ROI analysis or other methods are necessary to verify the improved accuracy of the anisotropic Gaussian filter.

The filter sizes that were used in this study were FWHM 12 mm, 8 mm, and 4 mm. The effects of the filter size on the voxel-based analyses also need to be investigated. According to the matched filter theorem, the filter size should be matched with signal of interest [Rosenfeld and Kak, 1982]. Jones et al [Jones et al., 2005] explored a wide range of filter sizes for the DT-MRI group analysis on schizophrenia, and concluded that each study should seek the optimum filter size for its own. One caveat in choosing the filter size is that if the filter size is too small, the residual might not be normally distributed, and it would not be supported by underlying assumptions of the Gaussian random field theory.

In addition, according to Jones' paper, he found significant differences in FA maps at certain kernel sizes, but did not find any significant difference on MD maps between two groups with any size of isotropic Gaussian kernel. This might suggest that the isotropic Gaussian smoothing could wipe the signal assuming that the difference in fact exists; at least this hypothesis holds for the corpus callosum analysis in this study.

In order to investigate the characteristics between two different smoothing approaches in voxel-based analysis, a segmented binary white matter mask for each subject was transformed using the same affine matrix that was used for normalization of DT-MRI measures. Since the binary mask did not have any diffusion tensor information, the smoothed-normalized binary white matter mask images should not show a statistical significance. On the contrary, Fig 5-13-a shows clusters on the same significance level ($P<0.005$, uncorrected) when being performed with two-tailed contrast *t* test. More interestingly as reducing the size of isotropic Gaussian filter, the number and size of clusters reduced substantially [Fig 5-13 b]. This indicates that blurring with a 12 mm isotropic Gaussian filter might have confounded the DT-MRI group analysis with morphologic differences. The patters were shown in similar regions to the DT-MRI analysis with isotropic Gaussian kernel smoothing, thus there is a confounding effect. Anisotropic Gaussian kernel smoothing showed far fewer morphological differences [Fig 5-14] suggesting that the DT-MRI differences are real in this case.

Subjects' age, and IQ related covariates may influence the voxel based analysis; future studies will examine the influence of these parameters onto the autism-control group differences.

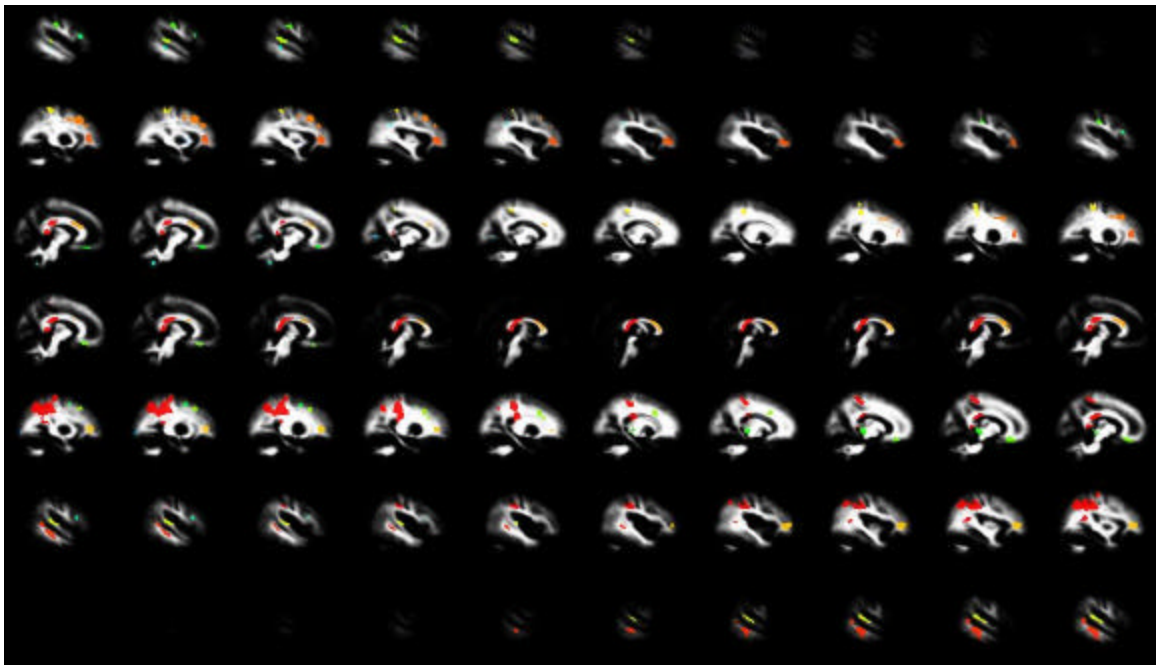

(a)

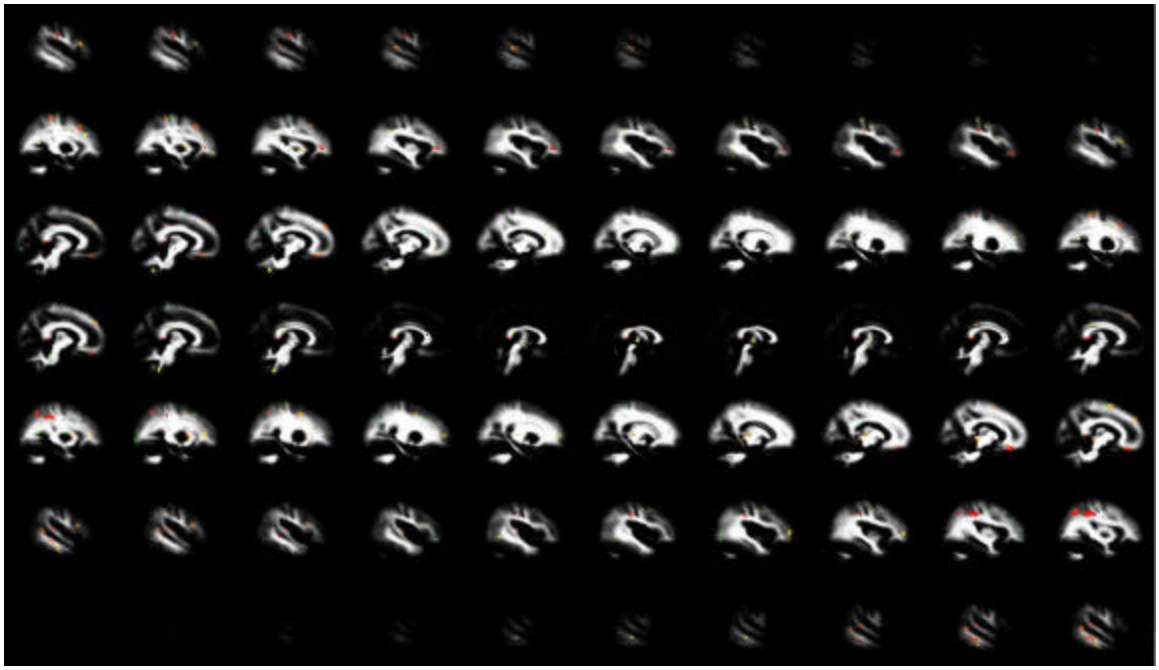

(b)

Fig 5-10 Co registered white matter mask analysis: isotropic kernel smoothing with (a) FWHM 12 mm (b) FWHM 4 mm.

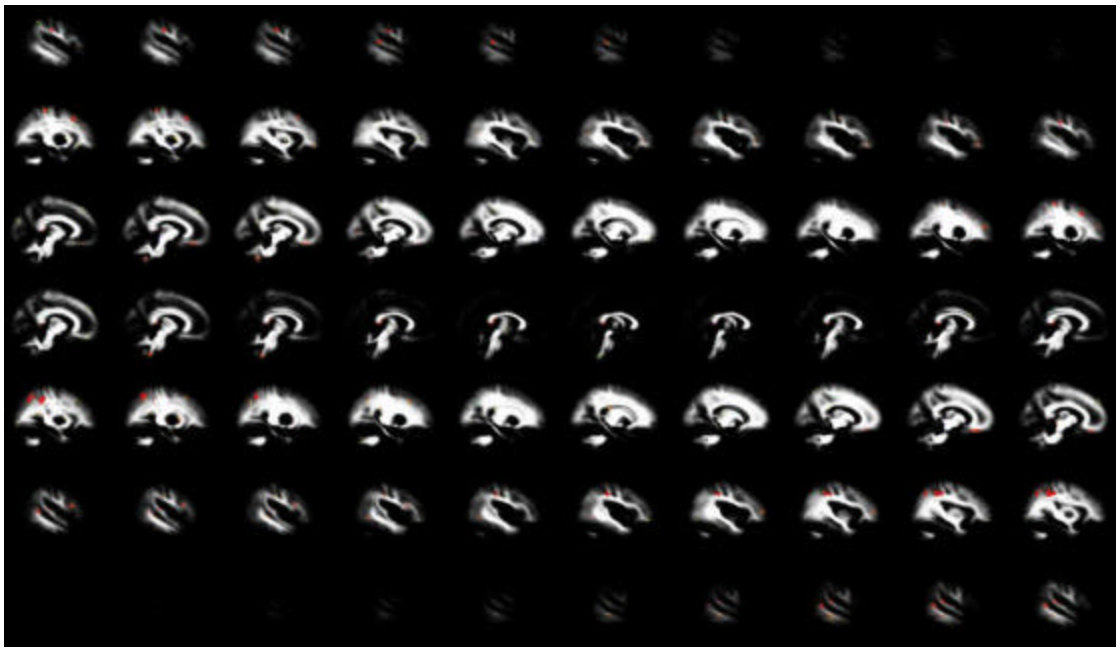

(a)

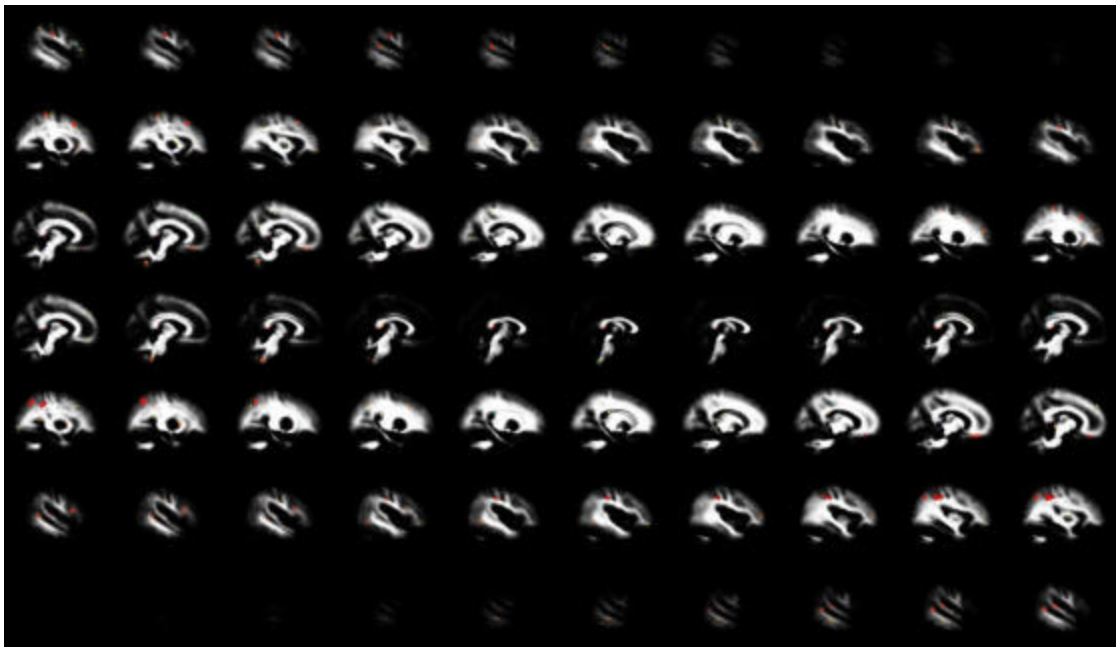

(b)

Fig 5-11 Co registered white matter mask analysis: anisotropic kernel smoothing with (a) FWHM 12 mm (b) 8mm. Clusters shown for an uncorrected p value of 0.005.

5.5 Conclusions

In this chapter, one application of the anisotropic Gaussian kernel smoothing was shown through the DT-MRI group analyses. The anisotropic Gaussian filter was tailored for each individual subject at a voxel level considering spatial transformation that occurred during data normalization. The less sensitivity of anisotropic Gaussian filter from over-filtering that was concluded in the chapter 4 was corroborated by the observation that the anisotropic Gaussian filter preserved the more peripheral white matter structures and the consequent blurring occurred in the direction of white matter directions on the white matter segmented DT measurements (FA, MD and eigenvalues). The ROI analysis of the corpus callosum was more consistent with results from anisotropically smoothed data. In addition, anisotropic smoothing showed fewer morphological differences through the binary mask analysis implying that anisotropic smoothing had less confounding effects onto the group analysis of DT-MRI measures.

CHAPTER 6

PROBABILISTIC CONNECTIVITY OF DT-MRI VIA ANISOTROPIC GAUSSIAN KERNEL SMOOTING

6.1 Introduction

White matter tractography (WMT) is a promising method for estimating the spatial white matter pathways that connect brain regions. [Mori et al., 1999; Conturo et al., 1999; Jones et al., 1999; Bassar et al., 2000]. Most WMT algorithms are based upon the assumption that the major eigenvector of the diffusion tensor, in general is aligned with the directions of white matter bundles. Researchers are continuously developing new techniques for tracing anatomical fibers from DT-MRI and general diffusion imaging [e.g., Pajevic et al., 1999; Poupon et al., 2000; Jones 2003, O'donnell et al., 2002; Brun et al., 2004; Jackowski et al., 2005]

White matter tractography is a noninvasive method for estimating a CNS structural connectivity. Potential applications of WMT include visualization of regional connectivity patterns in both healthy and diseased brains. For example, WMT may be used to map the locations of important white matter pathways (e.g., corticospinal tract) in

patients with brain lesions both prior to and after surgery [Lazar et al., 2006]. WMT may also be used to segment specific entire or parts of WM tracts for subsequent ROI analysis.

Unfortunately, the high sensitivity of DT-MRI to noise and other errors also causes errors in WMT reconstructions. A model of tractography error based on voxel size, distance, SNR and the difference between eigenvalues was developed by Anderson (2000). Lazar and Alexander validated this error model for several WMT algorithms [Lazar and Alexander, 2003]. The potential errors associated with single tractography streamline results have led to the development of probabilistic fiber tractography, which produces a map of connection probabilities from a defined region [Batchelor et al., 2001; Koch et al., 2002; Tournier et al., 2003; Behrens et al, 2003; Parker et al., 2003; Jones et al., 2003,; Lazar et al., 2005]. These methods also compensate somewhat for cases where there is less certainty in the WM fiber orientating, such as the case of non-prolate diffusion tensors.

In this chapter, anisotropic Gaussian kernel smoothing that was detailed in Chapter 4 is applied to generate probabilistic WMT maps of DT-MRI. Generating probabilistic WMT by way of Gaussian kernel smoothing has similarities to formerly proposed probabilistic approaches including Monte Carlo simulations, and solving the heat equation by fast-marching algorithm [Parker et al., 2002; Bachelor et al., 2001; Koch et al. 2001]. In contrast to theses methods, anisotropic Gaussian convolution will produce continuous and consistent connectivity patterns using a simple smoothing approach. The approach works by initializing a concentration at a specific brain region and then using iterative convolution smoothing to estimate a “concentration” of diffusion connectivity.

Gaussian convolution smoothing has been shown to be equivalent to solving the diffusion equation [Koenderink 1984].

6.2 Theory

White matter tractography: Deterministic Approach

Basic white matter fiber tracking methodologies are based on streamlines or line propagation algorithms

$$\frac{d\vec{r}(s)}{ds} = \vec{t}(s) \tag{6-1}$$

where $\vec{t}(s)$ is the unit tangent vector to $\vec{r}(s)$ at s, which is a stepping index (a dummy variable). Assuming that the white matter tracks are represented in the measured major eigenvectors of the diffusion tensor, $\vec{t}(s)$ may be replaced by

$$\vec{t}(s) = \vec{e}_1(\vec{r}(s)) \tag{6-2}$$

where $\vec{e}_1(\vec{r}(s))$ is the major eigenvector of the diffusion tensor that is estimated at position $\vec{r}(s)$. In regions with low diffusion anisotropy, tensor deflection was proposed to estimate the local tract directions [Lazar et al, 2003a]. The tensor deflection algorithm uses the entire diffusion tensor to approximate the unit tangent vector to the trajectory:

$$\vec{t}(s) = \overline{D}\vec{v}_{in} \tag{6-3}$$

A more general tractography algorithm, tensorlines, has been proposed, in which $\vec{v}_{out}$ is extended as

$$\vec{t}(s) = f\vec{e} + (1-f)((1-g)\vec{v}_{in} + gD\vec{v}_{in}) \tag{6-4}$$

where f and g are weighting factors that are in a range of [0, 1] [Weinstein et al., 1999].

For all these approaches, the white matter track realization is ultimately a line integration of (5-1) with an initial condition, $\vec{r}(0) = \vec{r}_0$, (a starting point or a seed point). Several numerical integration methods have been used, including Euler's method [Conturo, 1999] and Runge-Kutta integration [Basser et al., 2000]

White matter tractography: Probabilistic Approaches

Most probabilistic WMT methods use an iterative Monte Carlo tracking algorithm, where the tract orientation is perturbed at each step. The degree of perturbation is typically constrained by the local diffusion tensor. Consequently, highly anisotropic diffusion tensors will produce low dispersion, whereas more oblate or spherical tensors will result in high levels of tract dispersion [Koch et al., 2001, 2002, Parker and Alexander 2003b].

A different approach is proposed here directed to solve the partial differential heat equation using DT-MRI data. The Monte Carlo methods above approximate the effects of a thermal heat equation [Appendix B]. Therefore, the heat equation is ultimately the general solution to the random walk (e.g., Monte Carlo) problem. [Koenderink, 1984] showed that the kernel smoothing in image processing is equivalent to the evolution of the linear heat (or diffusion) equation if the kernels are Gaussian.

6.3 Methods

Simulated phantom

A simple three-dimensional numerical phantom shown in Fig 6-1 was constructed. The phantom consisted of two perpendicular synthetic fiber bundles with high anisotropy (FA> 0.8) crossing each other with surroundings regions filled with very low anisotropy tensors (FA< 0.02). A seed (intensity value 1) was placed in the left horizontal branch (Fig 6-1-c) and Gaussian kernel smoothing was performed to determine the kernel smoothing effects on the diffusion propagation.

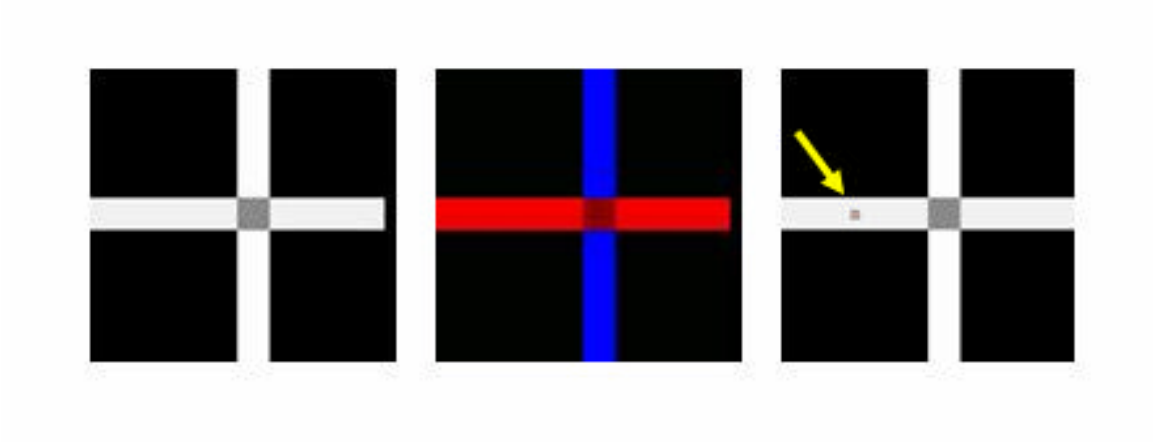

(a) (b) (c)

Fig 6-1 A numerical phantom with matrix size (100,100,100), a FA map of the central coronal view is shown. Two perpendicular cylinders have uniform tensor fields with high anisotropic properties, and the backgrounds (in black) are isotropic. The red bar indicates the numerical fiber in the x directions and the z direction is represented in blur in the color map (b). The position of an initial concentration for the diffusion propagation is shown in (c).

Anisotropic Gaussian kernel

As introduced in the chapter 4, the anisotropic Gaussian kernel is

$$K_t(\vec{r}) = \frac{\exp(-\vec{r}\overline{D}^{-1}\vec{r} / 4t)}{(4pt)^{n/2}(\det \overline{D})^{1/2}} \qquad (6\text{-}5)$$

where t is the parameter that determines the width of the kernel. In this simulation a t value of 0.05 was used and the resultant Gaussian kernel profile in each numerical fiber is shown in Fig 6-2.

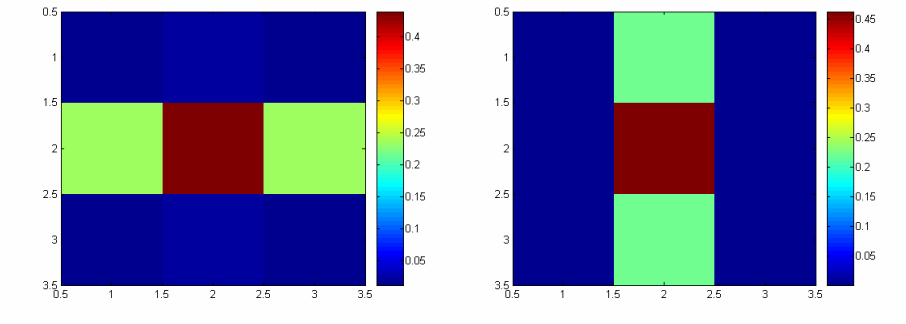

(a) (b)

Fig 6-2 (a) shows the x-y plane view of the kernel in the region of the red bundle in Fig 6-1(b). (b) is a projection view from the x-z plane in blur in color map Fig 6-1(b). Major weights in the kernel correspond to the shape of the fiber directions.

Raising the diffusion tensor to a higher power

The diffusion tensor $\overline{D}$ in (5-1) may be modified to accentuate the anisotropic shape of the tensor. The modified kernel may be formulated as

$$K_t(\vec{r}) = \frac{\exp(-\vec{r}(\overline{D}^P)^{-1}\vec{r}/4t)}{(4pt)^{n/2}(\det \overline{D}^P)^{1/2}} \qquad (6\text{-}6)$$

Powers of $P=1, 3$ were explored in this study.

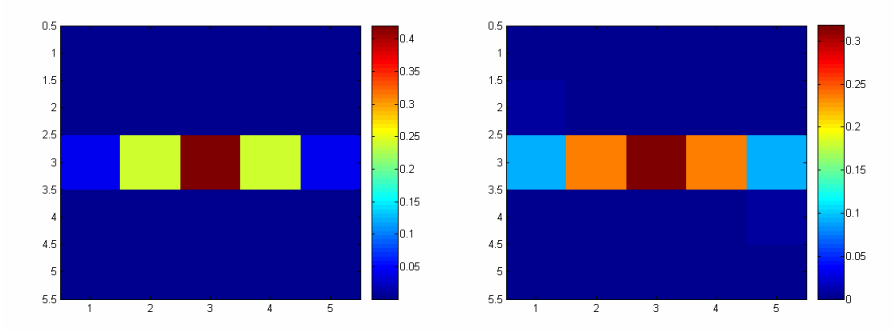

(a) (b)

Fig 6-3 Examples of Gaussian kernels projected on the x-y plane. (a) is the original tensor from the corpus callosum. (b) is the kernel from $\overline{D}^3$ at the same location

Human brain data

The averaged (gold standard) DW data used in chapter 4 was employed in this chapter to generate diffusion tensor and corresponding anisotropic Gaussian kernels. For human brain data, a bigger widow (5 x 5 x 5 voxels) was used to facilitate regions of curvature that are very commonly encountered in the brain data whereas the window that was used for the previous simulation in the simplistic phantom was 3 x 3 x 3 voxels.

6.4 Results

Simulated phantom

Fig 6-4 was generated without using the conventional threshold to mask low anisotropy regions. From the seeding point (in Fig 6-1), the diffusion profiles were spreading out in the fiber directions and toward crossing regions, the diffusion became separated into the three directions shown by the arrows.

The formulation of Fig 6-5-(a) to (c) is the same as for the Fig 6-4 except, in Fig 6-5 all diffusion propagation was restricted in the region of FA>0.1. As shown in Fig 6-5 (d) to (e) compared against Fig 6-5 (a) to (c), raising the power of the tensor improved the degree of anisotropy.

Human brain data

Fig 6-6 was generated using the power of $P=1$ (6-2). Increased power of the tensor propagated faster, however, it did not change the overall propagation maps as noticeably

as in the simulation.

The starting seed point was placed at splenium (shown in Fig 6-6 a), and the diffusion propagation was only allowed in the region of FA > 0.2. As the iteration of convolution increased, the diffusion tended to propagate more in the direction of the streamline tractography (Fig 6-6 f).

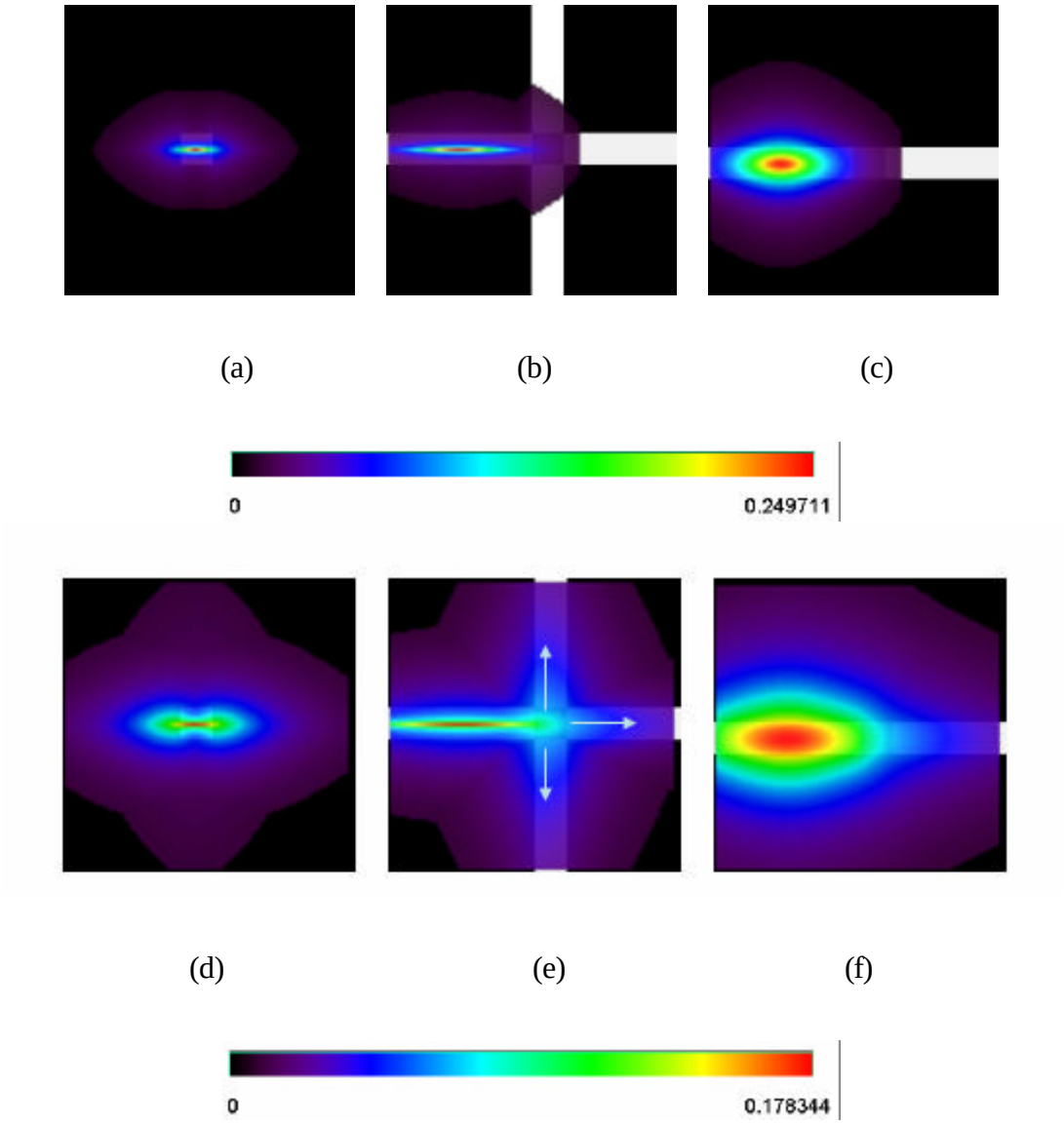

Fig 6-4. An example of the convolution smoothing with a seed point. (a), (b), and (c) are the maps of sagittal, coronal, and axial view of a diffusion map at the level of iteration=40. (d), (e), and (f) are from the iteration=200. Note that the diffusion propagation was not restricted in this simulation, and restriction was allowed in Fig (6-5). The color is displayed in log scale (-log1/p) of the diffusion probability, p

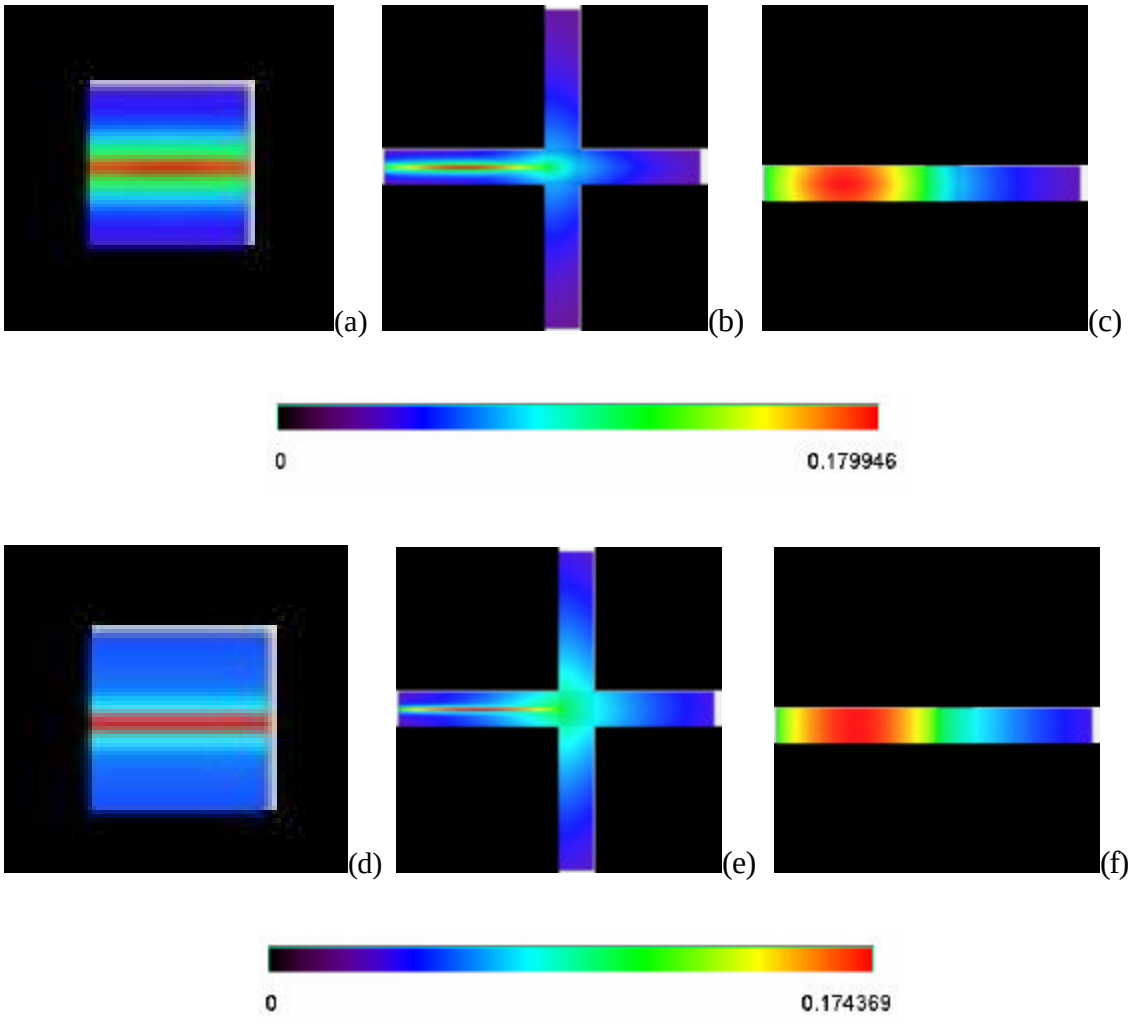

Fig 6-5 an example of effect of powers of the tensor. Increasing the power, p of $\overline{D}^P$ increases the propagation velocity with the same t value for $\overline{D}^1$. Using a 3x3x3 window, with t value 0.05, (a), (b) and (c) show sagittal, coronal, and axial views of using $\overline{D}^1$ and FA threshold mask (FA>0.1). (d), (e), and (f) are sagittal, coronal, and axial view of using $\overline{D}^3$. Gaussian convolution was applied 200 times with a t value of 0.05. Raising the power p, ($\overline{D}^P$), can accentuate the anisotropy shape of the tensor. Note that with the same t value and the same iteration of performance, the $\overline{D}^3$ case diffused faster in the fiber directions (Fig 6-5 b and e) and diffusion perpendicular to the fiber direction was more restricted in the magnified sagittal view (Fig 6-5 a and d). The sagittal views (a, d) are zoomed up for the better visualization. The color is displayed in log scale (-log1/p) of the diffusion probability, p.

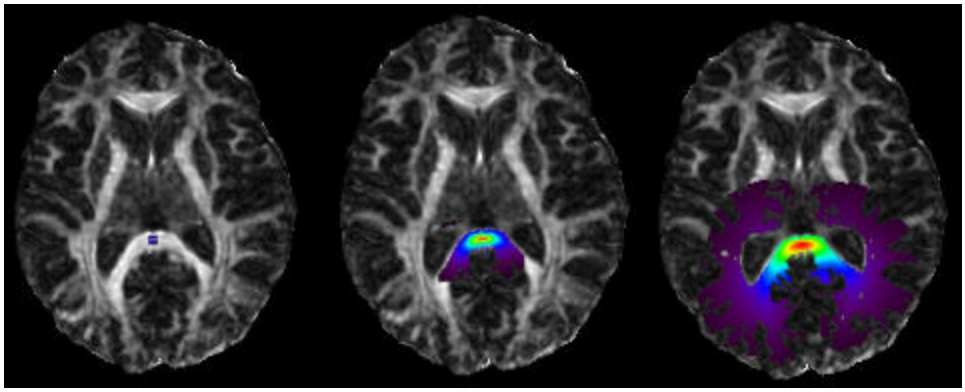

(a) (b) (c)

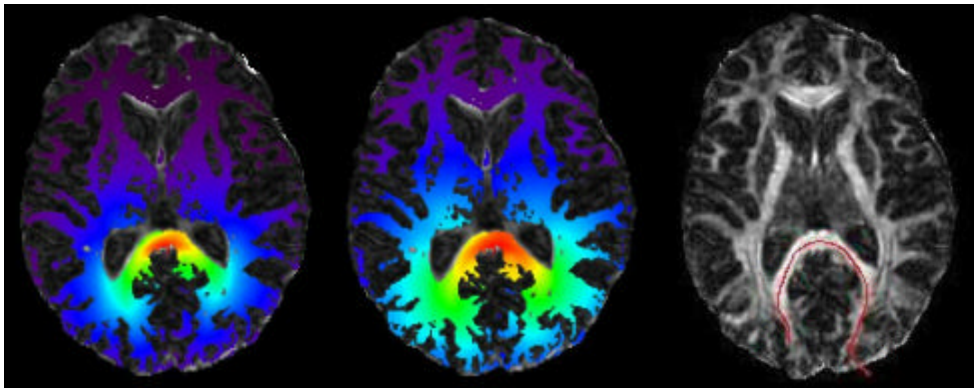

(d) (e) (f)

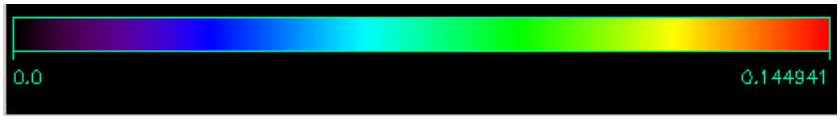

Fig 6-6 iterations at 1 (a), 10 (b), 40 (c), 200 (d), and 400 (e). In (f), a seed was positioned at the same location as for the convolution simulation, and then the Runge-Kutta interpolation method, with a FA threshold of 0.2, and an angle threshold of 45 degree, was used to generate a single track. The color in a-e is displayed in log scale (-log1/p) of the diffusion probability, p

6.5 Discussion

The connectivity probabilistic maps via anisotropic Gaussian kernel smoothing produced a propagation distribution that was based upon the voxel-wise diffusion tensor maps. Since the Gaussian kernel exists in three dimensions, the convolution process leads to the blurring in the non-major eigenvector directions. This ultimately leads to apparent connectivity in all arbitrary directions. To relate this issue, recently Morris et al proposed a method of estimating the statistical significance of connection using random walk simulation and PICo probabilistic tracking method [Morris et al., 2006]. In their method, a null connection frequency was set up with non-restricted random walk probability map and an experimental frequency was based on the connection map by PICo algorithm [Parker et al, 2003a]. A statistical test was conducted on the two distributions to achieve and estimate the significance of the experimental frequency connection map. Although their method was adopted to minimize distance-related artifacts, one of the problems of their method is that it is difficult to regularize the overall distribution concentration by the Monte Carlo algorithm. To compensate for this effect, the distributions from anisotropic and isotropic smoothing were computed in this study. Instead of using z statistics in [Morris et al., 2006] to estimate the significance, a new concept of *tensor distance* by measuring the similarity or dissimilarity between the tensors using Kullback-Leibler (KL) divergence [Wang and Vemuri, 2005] can be utilized for the study of significance of connection.

The KL divergence is defined [Kullback and Leibler, 1951]

$$KL(p \| q) = \int p(\vec{x}) \log \frac{p(\vec{x})}{q(\vec{x})} d\vec{x} \qquad (6\text{-}7)$$

where *p(x)* is the "true" probability distribution, and *q(x)* is the null probability distribution. $KL(p \| q)$ measures a natural distance (difference) between these two distinct probability distributions.

For the probabilistic connectivity by anisotropic smoothing, the KL distance can be a measure of dissimilarity between probabilistic map from isotropic smoothing (*q(x)*) and anisotropic smoothing (*p(x)*). In Fig 6-7, the KL distance was measured between $\overline{D}^1$ and $\bar{I}$ (identity matrix for isotropic smoothing). Fig 6-7 shows a diffusion propagation map obtained using the isotropic Gaussian kernel smoothing (a) and anisotropic Gaussian kernel smoothing (b). Fig 6-7-c is the dissimilarity measure using the Eqn (6-7). Interestingly in Fig 6-7-c the higher dissimilarity was observed in the vertical direction anisotropy bar (shaded in blue) and the KL distance decreased rapidly in the horizontal direction across the crossing region (shaded in violet). The difference between these crossing two directions was more evident in the KL maps. The reason for this dissimilarity originated from the two different FA values; FA of horizontal bar is 0.824494 and the FA of the vertical bar is 0.874281, so that ultimately the relative anisotropy was directed toward the vertical bar leaving smaller values at the horizontal bar.

Fig 6-8-d shows an example of the KL distance obtained in the corpus callosum. The modified KL distance $KL'(p \| q) = \frac{p(\vec{x})}{q(\vec{x})} \int p(\vec{x}) \log \frac{p(\vec{x})}{q(\vec{x})} d\vec{x}$ was attempted to create

more realistic connectivity patterns shown in Fig 6-9. Applications of KL distance need to be developed for determining statistical significance.

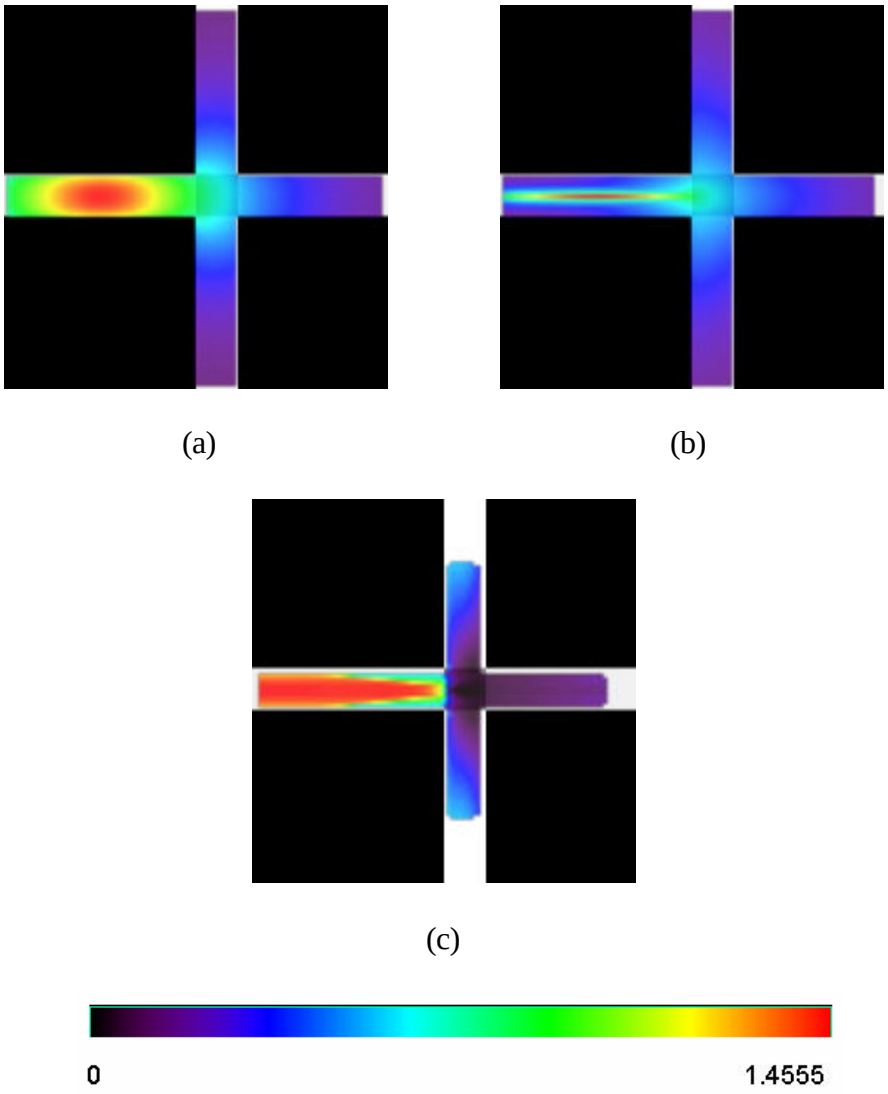

Fig 6-7 numerical simulation. (a) isotropic smoothing (b) anisotropic smoothing (c) KL distance at iteration 200.

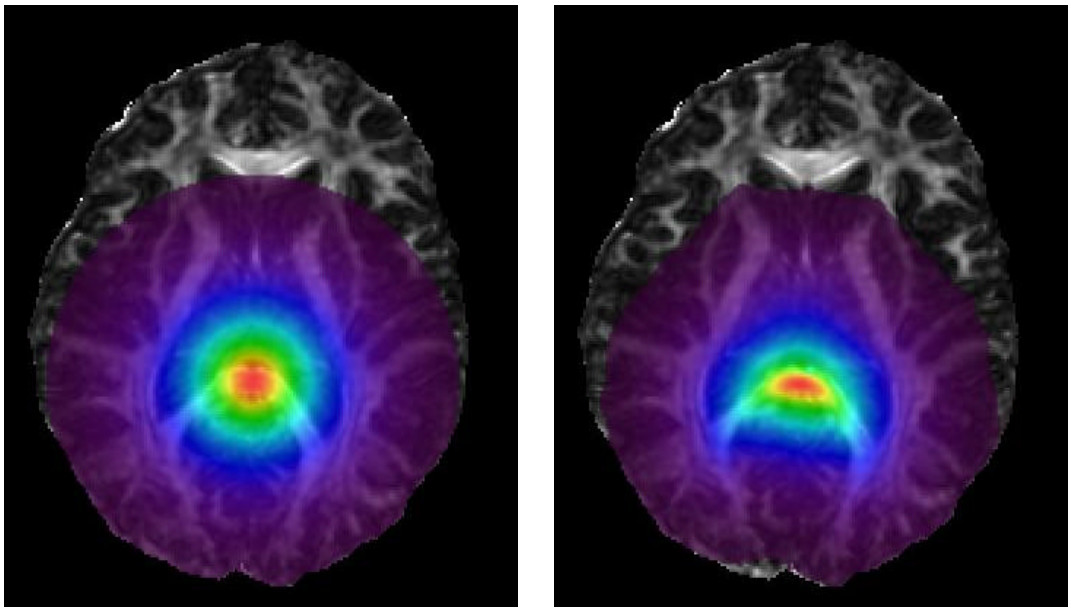

(a) (b)

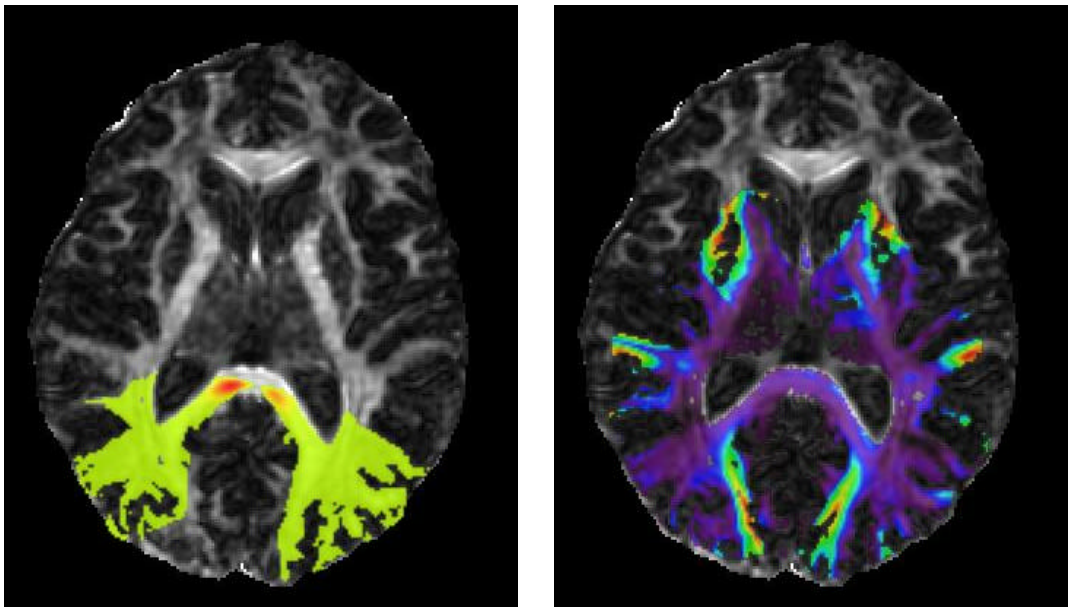

(c) (d)

Fig 6-8 (a) Isotropic smoothing map (b) anisotropic smoothing map. (c) Subtraction map of the isotropic smoothing from the anisotropic smoothing map. (d) KL distance. A seed at the same position in the Fig 6-4 Splenium. The KL distance (dissimilarity between isotropic smoothing and anisotropic smoothing) is shown using the rainbow color scale.

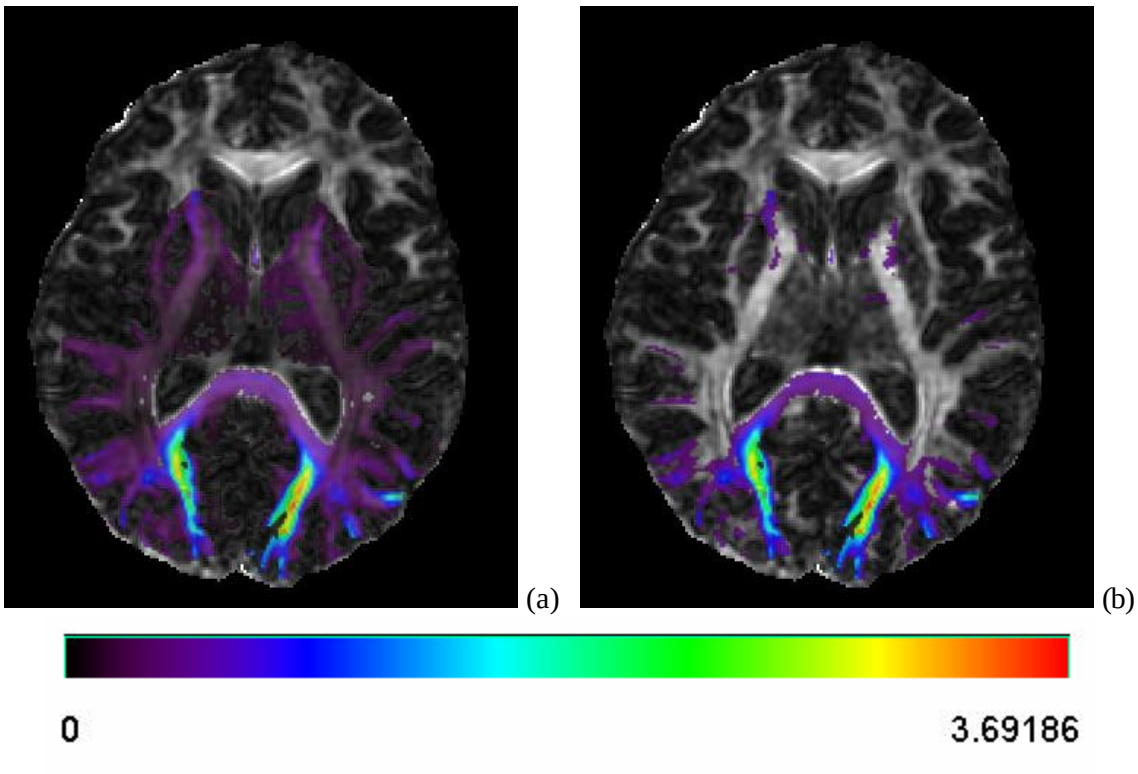

Fig 6-9 Modified KL distance for a seed situated at the same position as in the Fig 6-4 in the Splenium of the corpus callosum. The distance (dissimilarity between isotropic smoothing and anisotropic smoothing) is shown in the rainbow color scale. (b) is thresholded map for KL values longer than 0.3 in (a).

CHAPTER 7

CONLUSIONS AND FUTURE RESEARCH PLANS

This thesis investigates several novel methods based upon anisotropic diffusion-weighting and image filtering. A summary of each chapter is as follows:

Chapter 3: anisotropic optimization of diffusion-weightings reduces the variances of FA and MD measurements in the corpus callosum up to ~56 %. The method presented in this chapter is a desirable approach when a region is homogeneous and the tensor shape and orientations are predictable a priori; however, if the region of interest is mixed with different orientations, it may lead to erroneous results for characterizing each different tissue type.

Chapter 4: anisotropic Gaussian kernel smoothing is compared with isotropic Gaussian smoothing and the Perona Malik algorithm. The evaluation is done with a simulation using both synthetic noisy data and real human brain data. The performance of three spatial filtering methods for reducing errors of FA, MD and major eigenvector orientation demonstrates that an optimum level of filtering reduces the errors for all measures. The optimum performances of both the isotropic and anisotropic Gaussian filters are similar, yet the anisotropic filter is much less prone to over-filtering.

Chapter 5: an application of the anisotropic Gaussian kernel smoothing is shown

through a group analysis of autism data. The anisotropic Gaussian filter is constructed for each individual subject at a voxel level considering spatial transformation that takes place during data normalization. The anisotropic Gaussian kernel smoothing on white matter segmented DT measurements data preserves the more peripheral white matter structures and the consequent blurring occurs in the direction of white matter directions on the white matter segmented DT measurements (FA, MD, and eigenvalues). The ROI analysis in the corpus callosum is more consistent with results from anisotropically smoothed data. In addition, anisotropic smoothing shows fewer morphological differences through the binary mask analysis implying that anisotropic smoothing confounds the group analysis of DT-MRI measures less frequently.

Chapter 6: the connectivity probabilistic maps via anisotropic Gaussian kernel convolution produces a propagation distribution that is based upon the voxel-wise diffusion tensor maps. The evaluation is done with a simple numerical phantom and human brain data. The diffusion propagation in the phantom behaves as the tensor field guides in the phantom. The diffusion propagation in the splenium of the corpus callosum is also consistent with known anatomical connectivity.

As mentioned in Discussions of the last two chapters 5, and 6, more vigorous studies are required and to complete the work in depth. Subjects below are the future works that will be pursued.

The group analysis of DT-MRI data for autism using either anisotropic or isotropic smoothing will be performed in more detail using a range of kernel sizes and examining possible covariates such as age and behavioral measures.

Anisotropic Gaussian kernel smoothing for voxel-based group analysis still requires more thorough validation. Experiments for evaluating the strengths and weakness need to be performed. The validity of anisotropic kernel smoothing for random field theory still needs to be examined more thoroughly.

For the anisotropic kernel smoothing, further algorithmic development is necessary to minimize unlikely pathways to reduce the occurrence of false positive connections.

REFERENCES

[1] A.L. Alexander, K.M. Hasan, M. Lazar, J.S. Tsuruda, and D.L. Parker, "Analysis of partial volume effects in diffusion-tensor MRI," *Magn. Reson. Med*., vol. 45, pp. 770-780, 2001.

[2] A.L. Alexander, J.E. Lee, M. Lazar, R.M. Boudos, M.B. DuBray, T.R. Oakes, J. Lu, E.K. Jeong, E.D. Bigler, and J.E. Lainhart, "Diffusion Tensor Imaging of the Corpus Callosum in Autism," *NeuroImage (in press)*, 2006

[3] D.C. Alexander, C. Pierpaoli, P.J. Basser and J.C Gee, "Spatial Transformations of Diffusion Tensor Magnetic Resonance Images," *IEEE Transactions on Medical Imaging*, vol. 20 pp 1131-1139, 2001.

[4] A.W. Anderson, "Theoretical Analysis of the Effects of Noise on Diffusion Tensor Imaging," *Magn. Reson. Med*., vol.46, pp. 1174-1188, 2001.

[5] P.A. Armitage and M.E. Bastin, "Utilizing the Diffusion-to-Noise Ratio to Optimize Magnetic Resonance Diffusion Tensor Acquisition Strategies for Improving Measurements of Diffusion Anisotropy", *Magn. Reson. Med*., vol.45, pp. 1056-1065, 2001.

[6] R. Bammer, "Basic principles of diffusion-weighted imaging," *European Journal of Radiology*, vol. 45, pp. 169-184, 2003.

[7] N. Barnea-Goraly, S. Eliez, M. Hedeus, V. Menon, C.D. White, M. Moseley, and A.L. Reiss, "White matter tract alterations in fragile X syndrome: preliminary evidence from diffusion tensor imaging," *Am. J. Med. Genet, Part. B* 118B, pp. 81-88, 2003.

[8] P.G. Batchelor, D. L. G. Hill, D. Atkinson, and F. Calamanten, "Study of Connectivity in the Brain Using the Full Diffusion Tensor from MRI," *IPMI Lecture Notes in Computer Science*, vol. 2082, pp. 121-133, 2001.

[9] P. J. Basser, J. Matiello, and D. Le Bihan, "Estimation of the effective self-diffusion tensor from the NMR spin echo," *J. Magn. Reson. B* vol. 103, pp. 247-254, 1994.

[10] P. J. Basser, and C. Pierpaoli, "Microstructural and Physiological Features of Tissues Elucidated by Quantative-Diffusion-Tensor MRI," *J Magn Reson.*, vol. 111, pp 209-219, 1996.

[11] P. J. Basser, S. Pajevic, C. Pierpaoli, J. Duda, A. Aldroubi, "In Vivo Tractography Using DT-MRI Data," *Magn. Reson. Med*., vol. 44, pp.625-632, 2000a.

[12] P.J. Basser and S. Pajevic, "Statistical Artifacts in Diffusion Tensor MRI (DT-MRI) Caused by Background Noise," *Magn. Reson. Med*., vol. 44, pp. 41-50, 2000b.

[13] C. Beaulieu, "The basis of anisotropic water diffusion in the nervous system – a technical review," *NMR Biomed.*, vol. 15, pp. 435 – 455, 2002.

[14] J. Burns, D. Job, M. E. Bastin, H. Whalley, T. MacGillivray, E.C. Johnstone, and S. M. Lawrie, "Structural disconnectivity in schizophrenia: a diffusion tensor magnetic resonance imaging study," *Br. J. Psychiatry*, vol. 182, pp. 439-443, 2003.

[15] A. Brun, H. Knutsson, H-J. Park, M. E. Shenton, and C-F. Westin, "Clustering Fiber Traces Using Normalized Cuts," *LCNS*, vol. 3216, pp. 368-375, 2004.

[16] P.T. Callaghan, "Principles of Nuclear Magnetic Resonance Microscopy," Oxford Science Publications, pp 25-91, 1991.

[17] J. S. W. Campbell, K. Siddiqi, V. V. Rymar, A.F. Sadikot and G. B. Pike, "Flow-based fiber tracking with diffusion tensor and q-ball data: validation and comparison to principal diffusion direction techniques," *NeuroImage*, vol. 27. pp. 725-736, 2005.

[18] F. Catte, P-L. Lions, J-M. Morel, and T. Coll, "Image selective smoothing and edge detection by nonlinear diffusion," *SIAM journal on Numerical Analysis* vol. 29 (1), pp. 182-193, 1992.

[19] M.K. Chung, M. Lazar, A. L. Alexander, Y. Lu, and R. Davidson, "Probabilistic Connectivity Measure in Diffusion Tensor Imaging via Anisotropic Kernel Smoothing," UW Dept of Stats Technical Report NO. 1081, 2003.

[20] T. E. Conturo, N. F. Lori, T.S. Cull, E. Akbudak, A. Z. Snyder, and J.S. Shimony, "Tracking neuronal fiber pathways in the living human brain," *Proceeding of the National Academy of Sciences of the USA*, vol. 96, pp. 10422-10427, 1999.

[21] O. Coulon, D.C. Alexander, and S. Arridge, "Diffusion tensor magnetic resonance image regularization," *Medical image analysis*, vol. 8, pp.47-67, 2004.

[22] Z. Ding, J.C. Gore, and A.W. Anderson, "Reduction of Noise in Diffusion Tensor Images Using Anisotropic Smoothing," *Magn. Reson. Med.*, vol. 53, pp. 485-490, 2005.

[23] S. H., Erikkson, F. J. Rugg-Gunn, M.R. Symms, G. J. Barker, and J.S. Duncan, "Diffusion tensor imaging in patients with epilepsy and malformations of cortical development," *Brain*, vol. 124, pp. 617-626, 2001.

[24] C. M. Filley, "White Matter and Behavioral Neurology." *Ann. N.Y. Acad. Sci.* vol.1064, pp.162-183, 2005.

[25] C. D. Good, I. S. Johnsrude, J. Ashburner, R. N. A. Henson, K. J. Friston, and R. S. J. Frackowiak, "A voxel-Based Morphometric Study of Ageing in 465 Normal Adult Human Brains," *NeuroImage,* vol. 14, pp.21-36, 2001.

[26] K.M. Hasan, D.L. Parker, and A.L. Alexander, "Comparison of Gradient Encoding schemes for Diffusion-Tensor MRI," *JMRI.*, vol. 13, pp. 769-780, 2001a.

[27] K.M. Hasan, D.L. Parker, and A.L. Alexander, "Analytical Computation of the Eigenvalues and Eigenvectors in DT-MRI", *J Magn Reson.*, vol. 152, pp. 41-47, 2001b.

[28] M. Jackowski, C. Y. Kao, M. Qiu, R. T. Constable, and L.H. Staib, " White matter tractography by anisotropic wavefront evolution and diffusion tensor imaging," Medical Image Analysis, vol. 9, pp. 427-440, 2005.

[29] P. Jezzard, and R.S. Balaban, "Correction for geometric distortion in echo planar images from B0 field variations," *Magn. Reson. Med.*, vol. 34, pp. 65-73, 1995.

[30] D.K. Jones, M.A. Horsfield, and A. Simmons, "Optimal Strategies for Measuring Diffusion in Anisotropic Systems by Magnetic Resonance Imaging," *Magn. Reson. Med.*, vol. 42, pp. 515-525, 1999.

[31] D.K. Jones, A. Simmons, S.C.R. Williams, and M.A. Horsfield, "Non-Invasive Assessment of Axonal Fiber Connectivity in the Human Brain Via Diffusion Tensor MRI," *Magn. Reson. Med.*, vol. 42, pp. 37-41, 1999.

[32] D.K. Jones, L.D. Griffin, D.C. Alexander, M. Catani, M. A. Horsfield, R. Howard and S. C. R. Williams, "Spatial Normalization and Averaging of Diffusion Tensor MRI data Sets," *NeuroImage,* vol. 17, pp. 592-617, 2002.

[33] D.K. Jones, "Determination and Visualizing Uncertainty in Estimates of Fiber Orientation From Diffusion Tensor MRI," *Magn. Reson. Med.*, vol. 49, pp. 7-12, 2003.

[34] D.K. Jones, M.R. Symms, M. Cercignani and R. I. Howard, "The effects of filter size on VBM analyses of DT-MRI data," *NeuroImage,* vol. 26, pp. 546-554, 2005.

[35] M. Koch, V. Glauche, J. Finsterbusch, U. Nolte, J. Frahm, and C. Buchel, "Estimation of anatomical connectivity from diffusion tensor data, " NeuroImage, vol. 13, S176, 2001.

[36] M.A. Koch, D.G. Norris, and M. Hund-Georgiadis, "An investigation of functional and anatomical connectivity using magnetic resonance imaging," *NeuroImage*, vol. 16 pp. 241-250, 2002.

[37] J. Koenderink, "The Structure of Images," *Biological Cybernetics* vol. 50, pp. 363-370, 1984.

[38] S. Kullback and R. A. Leible, "On information and sufficiency," *Annals of Mathematical Statistics,* vol. 20, pp. 79-86, 1951.

[39] M. Lazar, D.M. Weinstein J.S. Tsuruda, K.M. Hasan, K. Arfanakis, M.E. Meyerand, B. Badie, H,A,Rowley, V. Haughton, A. Field, and A.L. Alexander, "White Matter Tractography Using Diffusion Tensor Deflection," Human Brain Mapping, vol. 18, pp. 306-321, 2003a.

[40] M. Lazar, and A.L. Alexander, "An error analysis of white matter tractography methods: synthetic diffusion tensor field simulations," *NeuroImage,* vol. 20, pp. 1140-1153, 2003b.

[41] M. Lazar, and A.L. Alexander, "Bootstrap white matter tractography(BOOT-TRAC)," *NeuroImage,* vol. 24, pp. 524-532, 2005.

[42] M. Lazar, A.L. Alexander, P.J. Thottakara, B. Badie, and A.S. Field, "White Matter Reorganization after Surgical Resection of Brain Tumors and Vascular Malformations," *AJNR Am J Neuroradiol,* vol. 27, pp. 1258-71, 2006.

[43] D. Le Bihan, and P.J. Basser, "Diffusion and Perfusion Magnetic Resonance Imaging," Raven press, Chapter 1, 1995.

[44] D. Le Bihan, J.F. Mangin, C. Poupon, C.A. Clark, S. Pappata, N.Molko and H. Chabriat, " Diffusion Tensor Imaging: Concepts and Applications," *Journal of Magnetic Resonance Imaging,* vol. 13, pp. 534-546, 2001.

[45] J.E. Lee, and A.L. Alexander, "Optimized diffusion tensor encoding schemes with anisotropic diffusion weighting," *12th Annual ISMRM meeting, Kyoto, Japan,* 2004.

[46] J.E. Lee, M .K Chung and A.L. Alexander, "Evaluation of Anisotropic Filters for Diffusion Tensor Imaging," *3rd IEEE International Symposium on Biomedical Imaging: Macro to Nano,* pp 77-80, *2006*.

[47] L. H. Leung, G.C. Ooi, D.L. Kwong, G.C. Chan, G. Cao, and P.L. Khong, "White matter diffusion anisotropy after chemo-irradiation: a statistical parametric mapping study and histogram analysis," *NeuroImage,* vol. 21, pp. 261-268, 2004.

[48] Z-P. Liang and P.C. Lauterbur, "Principles of Magnetic Resonance Imaging, A Signal Processing Perspective," IEEE Press Series in Biomedical Engineering, Wiley-IEEE Press; 1st edition , 1999

[49] C.C. Lin, and L.A. Segel, "Mathematics Applied to Deterministic Problems in the Natural Sciences". 1988

[50] P. Mansfield, *J. Physics*, C10, L 55, 1977.

[51] J. Mattiello, P.J. Basser, and D. Le Bihan, "The b matrix in diffusion tensor echo-planar imaging," *Magn. Reson. Med.*, vol. 37, pp. 292-300, 1997.

[52] S. Mori, B.J. Crain, V.P. Chacko, and P.C. Van Zijl, "Three-dimensional tracking of axonal projections in the brain by magnetic resonance imaging," *Ann. Neurol*., vol. 45, pp. 265-269, 1999.

[53] D. M. Morris, K. V. Embleton, and G. J. Parker, "Definition of connection significance using probabilistic tractography," *14th Annual ISMRM meeting, Seattle, WA*, 2006.

[54] M. E. Moseley, "Diffusion tensor imaging and aging-A review," *NMR Biomed.*, vol. 15, pp. 553-560, 2002.

[55] J. Neil, P. Miller, P. S. Mukherjee, and P. S. Huppi, "Diffusion tensor imaging of normal and injured developing human brain-A technical review," *NMR Biomed.*, vol. 15, pp. 543-552, 2002.

[56] D.G. Nishimura, "Principles of Magnetic Resonance Imaging," Stanford University, 1996.

[57] L. O'Donnell, S. Haker, and C-F. Westin, "New Approaches to Estimation of White Matter Connectivity in Diffusion Tensor MRI: Elliptic PDEs and Geodesics in a Tensor-Warped Space," *LCNS*, vol. 2488, pp. 459-466, 2002.

[58] S. Pajevic, A. Aldroubi, and P.J. Basser, "A continuous tensor field approximation of discrete DT-MRI data for extracting Microstructural and architectural features of tissues," *J Magn Reson*., vol. 154, pp. 85-100, 2002.

[59] S. Pajevic, and C. Pierpaoli, "Color schemes to represent the orientation of anisotropic tissues from diffusion tensor data: application to white matter fiber tract mapping in the human brain," *Magn. Reson. Med.*, vol. 42, pp. 526-540, 1999.

[60] N.G. Papadakis, D. Xing, C. L. H. Huang, L. D. Hall, and T.A. Carpenter, "Comparative study of acquisition schemes for diffusion tensor imaging using MRI," *JMR.*, vol. 137, pp. 67-82, 1999.

[61] G.J.M. Parker, J.A. Schnabel, M.R. Symms, D.J. Werring, and G.J. Barker, "Nonlinear Smoothing for Reduction of Systematic and Random Errors in Diffusion Tensor Imaging," *JMRI.*, vol.11, pp. 702-710, 2000.

[62] G.J.M. Parker, C.A.M. Wheeler-Kingshott, and G.J. Barker, "Estimating Distributed Anatomical Connectivity Using Fast Marching Methods and Diffusion Tensor Imaging," *IEEE Trans on Medical Imaging* vol. 21, pp. 505-512, 2002.

[63] G.J.M. Parker, H. A. Haroon, and C. A.M. Wheeler-Kingshott, "A Framework for a Streamline-Based Probabilistic Index of Connectivity (PICo) Using a Structural Interpretation of MRI Diffusion Measurements," *JMRI*, vol. 18, pp. 242-254, 2003a.

[64] G. J. M. Parker and D. C. Alexander, "Probabilistic Monte Carlo based mapping of cerebral connections utilizing whole-brain crossing fiber information," *Lecture Notes in Computer Science*, vol. 2737, pp. 684-695, 2003b.

[65] P. Perona, and J. Malik, "Scale-space and edge detection using anisotropic diffusion," *IEEE Trans. Pattern Anal. Machine Intell*, vol.12, pp. 629–639, 1990.

[66] C. Pierpaoli, and P.J. Basser, "Toward a quantitative assessment of diffusion anisotropy," *Magn. Reson. Med.*, vol. 36, pp. 893-906, 1996.

[67] M.A. Rodriguez-Florido, C-F. Westin, and J. Ruiz-Alzola, "DT-MRI regularization using anisotropic tensor field filtering," *In: 2004 IEEE International Symposium on Biomedical Imaging* - April 15-18 - Arlington, VA (USA). pp. 336–339.

[68] A. Rosenfeld, and A.C. Kak, "Digital Picture Processing 2." Academic Press, Orlando, FL, p.42, 1982.

[69] L. A. Segel, Mathematics Applied To Continuum Mechanics, 1977.

[70] R.I. Shrager, and P.J. Basser, "Anisotropically weighted MRI," *Magn. Reson. Med*., vol. 40, pp. 160-165, 1998.

[71] M. Sommer, M.A. Koch, W. Paulus, C. Weiller, and C. Buchel, "Disconnection of speech-relevant areas in persistent developmental stuttering," *Lancet*, vol. 360, pp.380-383, 2002.

[72] C. H. Sotak, "The role of diffusion tensor imaging in the evaluation of ischemic brain injury-A review," *NMR Biomed.*, vol. 15, pp. 561-569, 2002.

[73] J-D, Tournier, F. Calamante, D.G . Gardian, and A. Connelly, "Diffusion –weighted magnetic resonance imaging fiber tacking using a front evolution algorithm," NeuroImage, vol. 20, pp. 276-288, 2003.

[74] D. Tschumperle, and R. Deriche, "DT-MRI: Estimation, Regularization and Applications," *Eurocast 2003, 9th international conference on computer aided systems theory*.

[75] M.T. Vlaardingerborek and J.A. den Boer, "Magnetic Resonance Imaging" second edition, Springer.

[76] Z. Wang, B.C. Vemuri, Y. Chen, and T.H. Mareci, "A Constrained Variational for Direct Estimation and Smoothing of the Diffusion Tensor Field From complex DWI," *IEEE Transactions on medical imaging,* vol. 23, pp. 930-939, 2004.

[77] Z. Wang, B.C. Vemuri, Y. Chen Y, T. Mareci, "Simultaneous Smoothing and Estimation of the Tensor Field from Diffusion Tensor MRI," CVPR. 2003.

[78] Z. Wang, and B.C. Vemuri, "DTI Segmentation Using an Information Theoretic Tensor Dissimilarity Measure," *IEEE Transactions on medical imaging,* vol. 24, pp. 1267-1277, 2005.

[79] J. Weickert, "Coherence-enhancing diffusion of colour images," *Image and Vision Computing*, vol. 17, pp. 201-212, 1999.

[80] D. Weinstein, G. Kindlmann, and E. Lundberg, "Tensorlines: Advection-Diffusion based Propagation through Diffusion Tensor Fields," *IEEE Visualization Proceedings of the conference on Visualization '99: celebrating ten years,* pp. 249-253, 1999.

[81] William H. Press Numerical recipes in C: The art of scientific computing

[82] K. J. Worsley, A. C. Evans, S. Marrett, and P. Neelin, "A three dimensional statistical analysis for CBF activation studies in human brain," *J. Cereb. Blood Flow Metab.*, vol. 12, pp. 900-918, 1992.

[83] D. Xing, N.G. Papadakis, C. L. -H. Huang, M. L. Vee, T. A. Carpenter and L. D. Hall, "Optimised diffusion-weighting for measurement of apparent diffusion coefficient (ADC) in human brain," *Magnetic Resonance Imaging,* vol. 15, pp. 771-784, 1997.

[84] J. Zhang, N. Kang, and S. E. Rose, "Approximating Anatomical Brain Connectivity with Diffusion Tensor MRI Using Kernel-Based Diffusion Simulations," *LNCS,* vol. 3565, pp. 64-75, 2005.

[85] Y. Zhang, M. Brady, and S. Smith, "Segmentation of Brain MR Images through a Hidden Markov Random Field Model and the Expectation-Maximization Algorithm," *IEEE Transactions on Medical Imaging,* vol. 20, pp. 45-57, 2001.

Appendix A

Diffusion equation from Brownian motion

Consider the one dimensional case, a particle moves between Δ and $\Delta + d\Delta$ in a time interval t with probability $f(D)dD$, the probability distribution must satisfy

$$\int_{-\infty}^{+\infty} d\Delta f(\Delta) = 1, \tag{A-1}$$

$$f(\Delta) = f(-\Delta), \tag{A-2}$$

$$f(\Delta) \to 0 \text{ as } |\Delta| \to \infty, \tag{A-3}$$

If $C(x,t)$ is the density of the particles at time t, the total number of particles

$$N = \int_{-\infty}^{+\infty} C(x,t)\ dx \tag{A-4}$$

At time $t + t$, the density is $C(x,t+t) = \int_{-\infty}^{+\infty} f(D)C(x-D,t)\ dD$ (A-5)

Using the Taylor expansion

$$C(x,t+t) = C(x,t) + t\frac{dC}{dt} + \cdots$$

$$C(x-D,t) = C(x,t) - D\frac{\partial C}{\partial x} + \frac{D^2}{2}\frac{\partial^2 C}{\partial x^2} + \cdots$$

Substituting Taylor terms into (A-5)

$$C + t\,\frac{\partial C}{\partial x} = C\int_{-\infty}^{\infty} f(D)\,dD - \frac{\partial C}{\partial x}\int_{-\infty}^{\infty} f(D)\,D\,dD + \frac{\partial^2 C}{\partial x^2}\int_{-\infty}^{\infty} f(D)\,\frac{D^2}{2}\,dD \qquad \text{(A-6)}$$

Using the property of (A-1) and (A-2), (A-6) leads to $\frac{\partial C}{\partial t} = D\frac{\partial^2 C}{\partial x^2}$

Appendix B

Diffusion equation from Random walk

Let $w(m,N)$ be the probability that a particle will arrive m steps to the right after taking a total of N steps, and then (B-1) should be satisfied. This is called the difference equation.

$$\overline{w}(x,t+\Delta t)=\frac{1}{2}\overline{w}(x-\Delta x,t)+\frac{1}{2}\overline{w}(x+\Delta x,t) \tag{B-1}$$

$$\overline{w}(x,t)\equiv w(\frac{x}{\Delta x},\frac{t}{\Delta t}) \tag{B-2}$$

Thus $\overline{w}(x,t)$ is the probability that the particle which starts at the origin at time t=0 is located at point at time t.

$$x=m(Dx), \qquad t=N(Dt), \tag{B-3}$$

Since we are interested in the solution only after the particle has taken a large number of steps

$$N\to\infty, Dt\to 0 \qquad m\to\infty, Dx\to 0 \tag{B-4}$$

expanding the functions in (B-1) by the Taylor's expansion

$$\overline{w}_t(x,t)\Delta t+O(\Delta t)^2=\frac{1}{2}\overline{w}_{xx}(x,t)(\Delta x)^2+O(\Delta x)^3 \tag{B-5}$$

Dividing each term by $2\Delta t$ and setting (B-6), the diffusion equation (B-7) is derived.

$$\lim_{\Delta t \to 0, \Delta t \to 0} \frac{(\Delta x)^2}{2\Delta t} = D, \qquad D \neq 0, \tag{B-6}$$

$$\overline{w}_t = D\overline{w}_{xx} \tag{B-7}$$

Appendix C

Derivation of the covariance of directional diffusitivities

$$s^{2}_{D_i D_j} = \frac{1}{N}\sum_{k}^{N}({}^{k}dD_i \, {}^{k}dD_j)$$

$$= \frac{1}{N}\sum_{k}^{N}(\frac{{}^{k}\partial D_i}{\partial S_0}{}^{k}dS_0 + \frac{{}^{k}\partial D_i}{\partial S_i}{}^{k}dS_i)\times(\frac{{}^{k}\partial D_j}{\partial S_0}{}^{k}dS_0 + \frac{{}^{k}\partial D_j}{\partial S_j}{}^{k}dS_j)$$

Since S_0, S_i, S_j are all independent of each other their cross multiplication is zero

$$= \frac{1}{N}\sum_{k}^{N}(\frac{{}^{k}\partial D_i}{\partial S_0}\frac{{}^{k}\partial D_j}{\partial S_0}{}^{k}dS_0{}^{2})$$

$$= \frac{1}{b_i S_0}\frac{1}{b_j S_0}s^{2}_{S_0}$$

$$= \frac{1}{b_i b_j S_0{}^{2}}s^{2}_{S_0} \qquad \text{(C-1)}$$

Derivation of FA as an explicit function of directional diffusitivities

Starting with a single diffusion tensor model equation $S_i = S_0 \exp(-b_i D_i)$, where

The diffusion tensor $\overline{D} = \begin{bmatrix} D_{xx} & D_{xy} & D_{xz} \\ D_{yx} & D_{yy} & D_{yz} \\ D_{zx} & D_{zy} & D_{zz} \end{bmatrix}$, $D_i = \vec{g}_i{}^T \overline{D} \vec{g}_i$, $g_i = [g_x, g_y, g_z]_i$

Since $\overline{D}$ is a symmetric matrix, $D_i = \vec{g}_i{}^T \overline{D} \vec{g}_i$ can be simplified as

$$\vec{g}_i{}^T \overline{D} \vec{g}_i = [g_{xi}{}^2, g_{yi}{}^2, g_{zi}{}^2, 2g_{xi}g_{yi}, 2g_{yi}g_{zi}] \cdot \begin{bmatrix} D_{xx} \\ D_{yy} \\ D_{zz} \\ D_{xy} \\ D_{xz} \\ D_{yz} \end{bmatrix} = G\overline{D}$$

$$G^{-1} = (G^T G)^{-1} G^T$$

$$= \begin{bmatrix} \sum_{j=1}^{N} G^{-1}{}_{1,j} D_j & \sum G^{-1}{}_{4,j} D_j & \sum G^{-1}{}_{5,j} D_j \\ \sum G^{-1}{}_{4,j} D_j & \sum G^{-1}{}_{2,j} D_j & \sum G^{-1}{}_{6,j} D_j \\ \sum G^{-1}{}_{5,j} D_j & \sum G^{-1}{}_{6,j} D_j & \sum G^{-1}{}_{3,j} D_j \end{bmatrix}$$

N: number of encoding directions

$\therefore$ The diffusion tensor $\overline{D} = \sum_i G^{-1} D_i$ and the tensor $\overline{D}$ can be diagonalized to generate 3 eigenvalues and 3 eigenvectors Calculating eigenvalues l of the tensor $\overline{D}$

$$\begin{vmatrix} \sum_{j=1}^{N} G^{-1}{}_{1,j} D_j - l & \sum G^{-1}{}_{4,j} D_j & \sum G^{-1}{}_{5,j} D_j \\ \sum G^{-1}{}_{4,j} D_j & \sum G^{-1}{}_{2,j} D_j - l & \sum G^{-1}{}_{6,j} D_j \\ \sum G^{-1}{}_{5,j} D_j & \sum G^{-1}{}_{6,j} D_j & \sum G^{-1}{}_{3,j} D_j - l \end{vmatrix} = 0 \qquad \text{(C-2)}$$

Solving the (C-2), l_i becomes a function of D_i, which makes FA to be an explicit function of D_i using invariants.

$$FA = \sqrt{\frac{3}{2}} \sqrt{\frac{(l_1 - < l_i >)^2 + (l_2 - < l_i >)^2 + (l_3 - < l_i >)}{(l_1{}^2 + l_2{}^2 + l_3{}^2)}} \qquad \text{(C-3)}$$

Another approach to find the FA as an explicit function of D_i would be using the invariants of the tensor and numerical methods. The invariants are as follows:

$$I_1 = D_{xx} + D_{yy} + D_{zz}$$

$$I_2 = D_{xx}D_{yy} + D_{yy}D_{zz} + D_{zz}D_{xx} - (D_{xy}{}^2 + D_{yz}{}^2 + D_{xz}{}^2)$$

$$I_3 = D_{xx}D_{yy}D_{zz} + 2D_{xy}D_{xz}D_{yz} - (D_{zz}D_{xy}{}^2 + D_{xx}D_{yz}{}^2 + D_{yy}D_{xz}{}^2) \qquad \text{(C-4)}$$

The numerical approach of finding eigenvalues is

$$v = (I_1/3)^2 - I_2/3$$
$$s = (I_1/3)^3 - I_1 I_2/6 + I_3/2$$
$$f = a\cos(s/v \times \sqrt{1/v})/3$$

$$l_1 = I_1/3 + 2 \times \sqrt{v} \times \cos(f)$$
$$l_2 = I_1/3 - 2 \times \sqrt{v} \times \cos(f/3 + f)$$
$$l_3 = I_1/3 - 2 \times \sqrt{v} \times \cos(f/3 - f) \qquad \text{(C-5)}$$

By inserting the (C-5) into (C-3) , $FA=\sqrt{1-\frac{I_2}{(I_1^{\,2}-2I_2)}}$, which leads to the FA is an explicit function of diffusitivities D_i

Appendix D

Positive Definite

A positive definite tensor is not altered throughout the kernel convolution as long as all tensor elements within the discrete integral window are positive definite. If the weighting factor is $k_{ij}\ \ i=1,\cdots,n,\ j=1,\cdots,n$ window size= nxn

$$\sum\ k_{ij}=1$$

Assuming the tensor

$T=\begin{bmatrix} D_{xx} & D_{xy} & D_{xz} \\ D_{yx} & D_{yy} & D_{yz} \\ D_{zx} & D_{zy} & D_{zz} \end{bmatrix}$ is positive definite then, for any vector, $\vec{r}=(x,y,z)$,

$$\vec{r}\ T\ \vec{r}'\ >\ 0$$

$$x^2D_{xx}+y^2D_{yy}+z^2D_{zz}+2xyD_{xy}+2yzD_{yz}+2xzD_{xz}>0$$

the new tensor after kernel convolution, T' may expressed as following

$D_{xx}{}^{ij}$ means that D_{xx} values in the i,j position.

$$T'=\begin{bmatrix} \sum k_{ij}D_{xx}{}^{ij} & \sum k_{ij}D_{xy}{}^{ij} & \sum k_{ij}D_{xz}{}^{ij} \\ \sum k_{ij}D_{yx}{}^{ij} & \sum k_{ij}D_{yy}{}^{ij} & \sum k_{ij}D_{yz}{}^{ij} \\ \sum k_{ij}D_{zx}{}^{ij} & \sum k_{ij}D_{zy}{}^{ij} & \sum k_{ij}D_{zz}{}^{ij} \end{bmatrix}$$

calculating $\vec{r}\ T'\ \vec{r}'$

$$x^2\sum k_{ij}D_{xx}{}^{ij}+y^2\sum k_{ij}D_{yy}{}^{ij}+z^2\sum k_{ij}D_{zz}{}^{ij}+2xy\sum k_{ij}D_{xy}{}^{ij}+2yz\sum k_{ij}D_{yz}{}^{ij}+2xz\sum k_{ij}D_{xz}{}^{ij}$$

$$= \sum k_{ij}(x^2 D_{xx}{}^{ij} + y^2 D_{yy}{}^{ij} + z^2 D_{zz}{}^{ij} + 2xyD_{xy}{}^{ij} + 2yzD_{yz}{}^{ij} + 2xzD_{xz}{}^{ij})$$

let $A_{ij} = x^2 D_{xx}{}^{ij} + y^2 D_{yy}{}^{ij} + z^2 D_{zz}{}^{ij} + 2xyD_{xy}{}^{ij} + 2yzD_{yz}{}^{ij} + 2xzD_{xz}{}^{ij}$

if all tensors in i, j position are positive definite, then $A_{ij} > 0$

$$= \sum k_{ij} A_{ij} > 0$$

Applying the kernel to the directional diffusitivity is the same as the applying the kernel to the tensor due to the linearity

$D_i = g_{,}' T g_i$

$D = GT$

$T = (G'G)^{-1} G' D$

$(G'G)^{-1} G'$ is a constant matrix.

$\therefore T$ is proportional to D